A PARAMETRIC STUDY OF POLARITY, CONTACT AND CURRENT RISETIME EFFECTS ON WIRE ARRAY Z-PINCHES

A Dissertation

Presented to the Faculty of the Graduate School

of Cornell University

in Partial Fulfillment of the Requirements for the Degree of

Doctor of Philosophy

by

David Arthur Chalenski

February 2010

A PARAMETRIC STUDY OF POLARITY, CONTACT AND CURRENT RISETIME EFFECTS ON WIRE ARRAY Z-PINCHES

David Arthur Chalenski, Ph.D.

Cornell University 2010

Data presented are the culmination of experiments studying the combined effects of polarity, contact and current risetime on wire array z-pinches operated on the 1 MA, 100-200 ns Cornell University COBRA pulsed power generator. Data were collected on 16-wire, 12.5 μm φ aluminum z-pinch arrays in both negative and positive polarity, with soldered and non-soldered contacts, and with slow and fast risetimes (100ns and 200ns). A minimum of five shots were collected for each of the eight cases to obtain statistical significance. The initiation, ablation, implosion and stagnation phases were compared for the various cases.

Polarity was modified via a 12 nH bolt-on convolute, rotatable to provide positive or negative polarity with similar inductance in each case, allowing side-by-side comparisons. Contact was modified by applying Pb60Sn40 solder to the cathode wire-electrode contact point or leaving the array unsoldered. The current risetime was varied between a 100 ns "short" pulse and 200 ns "long" pulse by utilizing current-pulse shaping capabilities of the COBRA pulsed power generator.

These experiments aimed to build upon previous research by Duselis et al. (2004), which showed that polarity, contact and current risetime have significant impact on energy deposited and uniformity of expansion of single wires under low-current (<10 kA) conditions. These low current experiments were designed

to mimic the conditions on a single wire of a wire-array z-pinch during initiation, also known as the resistive voltage phase. Experiments presented here aim to build upon this research by establishing a better understanding of the effects of polarity, contact and current risetime on the initiation, ablation, implosion and stagnation phases of wire array z-pinches, and also to understand the utility of low current, single wire results as they pertain to higher current, wire array z-pinches.

The data were collected in two separate experimental runs: a preliminary dataset with only contact and current risetime as the variables (four distinct cases), and a second, full dataset examining polarity, contact and current risetime (eight distinct cases).

The first dataset showed a significant improvement to long pulse shots when the wires were soldered to the cathode, but no improvements to short pulse shots. Long pulse, soldered shots from this dataset were also observed to exhibit the "Christmas tree" effect, or time-accelerated pinch dynamics at the cathode and axial flow towards the anode. The second dataset showed that, with short pulses only, operating arrays in positive polarity resulted in a 25% improvement in deposited energy, 30% smaller achieved current radius, 20% improvement in peak x-ray power and a 50% improvement in x-ray yield when compared to negative polarity arrays. Soldering contacts showed a 10% improvement in initiation energy deposited in positive polarity only, but no subsequent correlated improvement in x-ray yield. Short pulse shots showed a ten-fold increase in peak x-ray powers and yield over long pulse shots. The two datasets were compared, and recommendations for future work were developed.

BIOGRAPHICAL SKETCH

David Arthur Chalenski was born to Arthur Abdon and Claire Marie Chalenski on June 11th, 1982 in Syracuse, NY. He spent formative stage #1 in and around Syracuse, while attending the Fayetteville-Manlius school system. He decided that moving greater than 60 miles from home would be silly, and consequently applied to the Cornell University School of Engineering. Formative stage #2 began the day he got his acceptance letter, and included his undergraduate and graduate careers at Cornell.

The decade plan at Cornell University does not appeal to everybody, but Dave "The Rabbi" Chalenski has managed to love nearly every minute of it. Dave graduated with his B.S. in electrical and computer engineering in 2004, and initially pursued his M.Eng. before transferring into the Ph.D. program.

Formative stage #3, or life after Cornell, will be a radical shift, but Dave is looking forward to enjoying as vibrant a life as he did all of his previous years.

To the memory of Paladin Chalenski (January 21, 1995 - February 4, 2009)

This man's best friend

ACKNOWLEDGEMENTS

To all my friends: each and every one of you has had a remarkable impact on my life. I cannot thank you enough.

To Harry, Todd and Joyce: thank you for the countless good times/discussions, and being the people behind the curtain at LPS. Your attentions to details and attitudes ensured that we collectively made any progress whatsoever.

To my colleagues at LPS: Thank you for all your help and camaraderie in the lab and at conferences. When I actually managed to relax in lab, I had some of the more enjoyable conversations of my life with all of you.

I would like to thank my committee members, Professors Paul Kintner and Richard Lovelace. They have always been supportive of my accomplishments and tolerant of my shortcomings.

To the Cornell Buds: take Natties 2010, and continue being carried by the D-line -The Rabbi

To the residents of 218B: nine years and we finally got the correct formula! Here's a Venn Diagram!

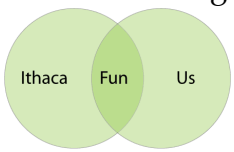

To Rick James Brown: Ever a trustworthy accomplice. Done in Cornell's keeping?

To Michelle: I thank you for your love and companionship. Let us hope that the sporadic weekend visits are soon a thing of the past!

To my sisters Sue and Cat: you tried to ruin me during childhood by pushing me through that wall and repeatedly taping my face into mangled contortions, but somehow I persevered! I hope that many years down the road we will

continue to have as much fun together as we do today.

I have done it all here at Cornell: short and long hair, bike mechanic and plasma physicist, struggling musician and damaged athlete, beacon of hope and all-consuming emotional gravity well. One person has stuck with me through it all (my parents briefly abandoned me for my Tuvan Throat Singing phase): Bruce Kusse. I walked into this lab to meet Bruce as a junior, a lime-shade of green (but at least I could turn a ratchet). I'm a deeper forest green now, but ready to take on the world. Bruce has been with me through all my phases of productivity, as well as complete lack there-of. His companionship, focus on his students and rigorous methodologies combined melodiously to develop the new lens through which I view the world. I owe a substantial portion of whatever success I may achieve to Bruce.

Finally, to my parents: you have given me everything I have in this world. I cannot thank you enough.

TABLE OF CONTENTS

LIST OF TABLES

LIST OF FIGURES

CHAPTER 1

INTRODUCTION

1.1 Background

The z-pinch, in its most fundamental form, is a conducting column through which current is driven in the axial direction. This current produces an azimuthal magnetic field, which, through the Lorentz **J**x**B** force, creates a radially-directed force inwards at all points on the cylinder. If the cylinder is a plasma (as it usually is when dealing with relevant experiments), and the **J**x**B** force is greater than any resisting or outwards-pointing force, the plasma is drawn in towards the z-axis. Upon reaching the axis, the cylindrically imploding plasma compresses, stagnates (or "pinches"), and energy from the implosion is converted into x-rays. The **JxB** force can also be applied to two wires carrying current in the same direction, as shown in Figure 1.1.

In the laboratory, modern day z-pinches operate at enormous extremes of the physical and temporal ranges: Sandia National Laboratory's Z Machine (Z, recently upgraded to the refurbished-Z Machine, ZR), the largest z-pinch generator in operation today, has a peak current of 26 MA, and delivers this current to a load in under 100 ns. The resultant x-ray output is expected to be 350 TW, with a total x-ray energy of 2.7 MJ [1]. This represents the most powerful laboratory source of x-rays available today, and as such is useful for a wide variety of scientific purposes, including research into inertial confinement fusion (ICF), x-ray lithography, spectroscopy and microscopy, neutron sourcing, astrophysical and equation-of-state research, and a whole host of other high-energy scientific ventures.

The path which z-pinches have taken started in the early days of research in

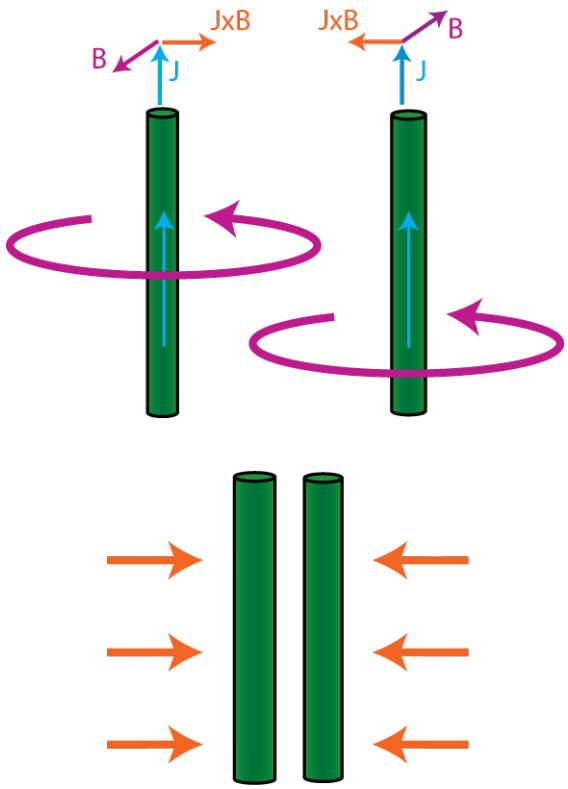

Figure 1.1: **JxB** force on two current-carrying wires

electricity and magnetism. By definition, any current path is a z-pinch, so electrostatic generators that could create arcs in air are, in effect, z-pinch generators. However, z-pinches truly gained traction with the development of the Bennett relation in 1934, which gave the current required to contain a uniform plasma column:

$$I_C = 1.4 * 10^{-9} r_p \sqrt{n_e T}$$

Where I_C is the current through the column in MA, r_p is the radius in cm, n_e is the electron density per cm^3, and T is the electron and ion temperature in keV. This formula allowed plasma and density temperatures to be related to the current required to contain the column, which, as the formula predicts, can be remarkably low.

In the 1950s, the development of the z-pinch as a pathway to ICF began [2]. Interest was generated because z-pinching was seen as a way to confine and heat a plasma, ultimately reaching nuclear fusion conditions. However, the initial momentum in z-pinches at Los Alamos and the Kurchatov Institute in Russia was temporarily halted by limitations in the current sources. Pulsed power generators at the time were limited to μs scale current risetimes, and the timescales at which the implosions occurred were too slow compared to magneto-hydrodynamic (MHD) instabilities that occurred on much faster timescales, ruining the symmetry of the implosion.

As dependent as they are upon pulsed power, z-pinches tend to track well with advances in pulsed power drivers. Therefore, z-pinch research stagnated somewhat through the 1960s until the 1970s, when J.C. (Charlie) Martin and colleagues revolutionized the pulsed-power field with their development of nanosecond pulsed power techniques [3, 4, 5]. These pulsed power generators rapidly reached MA-, MV- and TW-levels. Research started first with single wires, but these were limited in x-ray output due to the high initial impedance of a single wire. The next step was to consider loads that could be of a larger initial diameter, and therefore lower initial inductance. These loads would also benefit from the higher implosion velocities due to acceleration from a larger diameter. The first loads attempted were annular liners, followed by wire arrays and gas puff loads. This development continued through the 1980s and into the 1990s. The work on initial 5 MA- 50 ns-scale devices (such as Proto-II) in the late 1970s led ultimately to the to the construction and subsequent upgrading of PBFA-II into the 20 MA, 100 ns Z-Machine (Z) at Sandia National Laboratories [6, 7]. Continuous advances in pulsed power techniques, especially magnetically insulated transmission lines (MITLs) and high-voltage, low jitter switches,

allowed these advances to unfold.

Another substantial advancement in wire array z-pinches occurred when Sanford et al. [8] and Deeney et al. [9] showed that increasing the number of wires from 6-10, the standard at the time, to ~90 dramatically improved x-ray power. The intuitive reason for this improvement is that the azimuthal inhomogeneity of an array with smaller number of wires is improved by approaching a more symmetrical, shell-like implosion with more wires. Limits to this increase of wire numbers have been determined, but these papers generated an explosion in wire array load configurations and experiments. Wire array experiments today are aimed at improving symmetry of implosion and reducing symmetry-destroying MHD instabilities.

The past couple years have seen another exciting advancement at Sandia: the 20 MA Z machine has been gutted and refurbished, yielding the 26 MA ZR [1, 10, 11]. Scientists at Sandia have spent the past year bringing ZR online and performing proof-of-principle tests, but are just now starting to break new ground on physics research. ZR will be another step towards ICF using z-pinches as a driver, and to explore new regimes of physics previously impossible.

1.2 Plasma physics research at the Cornell University Laboratory of Plasma Studies

Research on z-pinches over the past several decades has rapidly accelerated [12]. The large scale facilities uncover new physics and ideas, yet have such a low shot-rate that they often cannot keep up with the ideas that they generate. Universities fill a valuable role by facilitating the understanding of z-pinches

and high energy density physics on much smaller scale machines (1-5 MA). The smaller scales allow higher shot rates and the lower cost per shot facilitates more experimental research. To this end, the Center for the Study of Pulsed-Power-Driven High-Energy-Density Plasmas was established here at Cornell University. In addition to the Cornell University Laboratory of Plasma Studies (LPS), other members of the center include the Lebedev Institute in Russia, Imperial College in London, the Weizmann Institute in Israel, the University of Rochester in New York and the University of Nevada, Reno. Participants collaborate by pooling knowledge, findings, and offering the use of facilities to each other.

LPS currently employs 4 professors, 1 research scientist, 2 visiting scientists from Russia, 2 technicians, 1 account representative, 5-10 graduate students, and an ever-shifting gaggle of undergraduates. The recent addition to LPS is the COrnell Beam Research Accelerator (COBRA), a 1 MA, 100-200 ns pulsed power driver [13, 14, 15, 16]. COBRA is predominantly used with single wire array z-pinches as the load, but other past and future experiments include, but are not limited to, radial/cylindrical foils, nested arrays, gas puffs z-pinches, x-pinches, conical arrays for astrophysical work, linear arrays, and more exotic loads. The first 2-3 years of experiments on COBRA were primarily focused on diagnostic development and proof-of-principle tests, but the future for COBRA holds many new and exciting possibilities as new experiments are rapidly brought on-line.

1.3 The present state of z-pinch research

The modern best-in-class z-pinch, driven by ZR with 26 MA in 100 ns, has shown a 15% efficient conversion of electricity "from the wall" to x-ray power [17, 18, 19]. This remarkable efficiency is highly desirable for ICF because every

last bit of energy must be squeezed out to improve gain in a practical power plant. Using the highly efficient wire array z-pinch, Sandia scientists have outlined a ~50-year road map to creating a full-scale test power plant [20].

Despite the positive outlook, there is a lot of work to be done. A main focus of present research is power scaling laws [21, 22]: determining how radiated x-ray power scales with current input. Accurate power scaling laws will allow predictions on specifications of a theoretical generator capable of ICF. Present thought is that a generator capable of delivering 60 MA with a risetime of 100 ns may be necessary [23].

In parallel with power scaling laws, the four defined stages of the z-pinch, initiation, ablation, implosion and stagnation, must constantly be studied and optimized to improve the x-ray output. The experiments in this dissertation were focused on this aspect of z-pinch improvements: examining the impacts of changes in early stage z-pinch dynamics on later stages, namely x-ray production.

1.3.1 Four phases of the wire array z-pinch

Following is a description of the present understanding of the four phases of a typical wire array fast z-pinch implosion. A good review of this material can be found in reference [24]. The phases considered will be for a typical single imploding wire-array. There are many exotic array and experimental configurations which do not follow this format, and therefore will not be considered here.

1.3.1.1 Phase I (Initiation)

The initiation phase, also called the resistive heating or resistive voltage phase, is characterized by the conversion of the initial, cold wires to hot cores surrounded by a low-density ($<10^{17\text{-}18}$) conducting plasma. The phase begins with each wire acting as a single entity (not substantially magnetically-connected) when current starts to rise. Current resistively heats each wire, increasing the voltage across them and depositing energy by Joule heating. The current per wire, < 10 kA, is not high enough to have a substantial impact on surrounding wires which are on the order of 1 mm away. Beginning at an undetermined time in this phase, adsorbed gases are expelled from the wire surface. These gases are initially of a higher resistance than the wire core and therefore do not conduct substantially more current than the wire cores, but, at a certain time, the gases are rapidly ionized through thermal transfer from the wires and Joule heating of the gases themselves. This forms a low-resistance coronal plasma shunt around the wire cores and the current preferentially switches to this plasma. The current will continue to rise, but the low resistance of the plasma (several orders of magnitude lower than the remaining wire cores) has eliminated any resistive voltage drop across the array. The current-switching occurs very rapidly, typically in less than 2 ns, and can be seen as a sharp drop to zero on any voltage monitor capable of explicitly showing resistive voltage. This so-called "voltage breakdown" defines the end of the initiation phase. The switching of current to the coronal plasma also halts substantial Joule heating to the wire cores themselves, so a figure of merit for comparing initiation phases is the deposited energy, or the multiplied voltage and current integrated from t=0 to voltage collapse.

The length of the initiation phase is typically determined by the current and current risetime [25, 26, 27], thickness and number of wires and the ability of

other experimental parameters to keep the coronal plasma from forming [28]. The duration of initiation also has an impact on deposited energy, as holding off voltage breakdown typically increases deposited energy in the wires. It has been theorized that the amount of deposited energy is critical to later stages due to initiation's impact on ablation and the plasma shell symmetry, so controlling the the initiation phase has been deemed critical to the z-pinch development effort [29, 30, 22].

At the end of the initiation phase, the remaining wire cores are left in either a solid, liquid or vapor state, dependent upon the amount of energy deposited. It has been theorized that it is most desirable for the wires to be in a homogeneous liquid state [31, 29]. Homogeneous liquid cores will produce the optimum ablation rate, as described in the next section. Whatever their state, the wire cores are surrounded by coronal plasma expanding with a velocity experimentally determined to be ~1.5x10^4 ms^{-1} [32].

1.3.1.2 Phase II (Ablation)

The ablation phase is characterized by the transition from independent, individual wire cores with a surrounding coronal plasma, to a shell-like plasma at the array radius continuously injecting material onto the axis of the array, forming a "precursor" plasma. The specific dynamics of ablation are heavily dependent upon experimental parameters, and are still the focus of much study [14, 33, 34, 35, 22].

The plasma projected from each individual wire in the initiation phase eventually reaches neighboring wires (it grows with a relatively constant velocity, as described above), and the continuous rise of currents heats the coronal plasma and wire cores (albeit mainly through thermal transfer from the coronal

plasma), which remain in their original positions and continue to project (ablate) more material into the surrounding plasmas. Throughout this phase, the current is high enough for the **JxB** force to draw material from the plasma inward towards the axis. This is the process typically referred to as ablation, the specifics of which are still hotly discussed. Recent results show that the x-ray power is heavily dependent upon ablation rate [22], which is dependent upon the state of the wire cores after initiation [30, 29].

At the end of the ablation phase, which is typically not clearly well-defined, a quasi-shell of conducting plasma remains at the original diameter of the wires, material is still streaming from this shell, the ablating wire cores still exist in some fashion at their original positions, and a low-density, weakly emitting precursor plasma rests on axis [36, 14].

1.3.1.3 Phase III (Implosion)

The implosion phase is characterized by the driving implosion of mass from the original wire positions to the central axis of the array. Recent results show that the implosion begins when gaps form in the ablating structure of the wires and coronal plasmas [37]. This forces an imploding sheath of material inward towards the array axis, the homogeneity of which is determined by the uniformity of the previously ablated material. As this sheath of material moves in, it collects previously ablated material, called the "snowplow."

The quality of implosion is balanced upon two key effects of the previous ablation rate: Rayleigh-Taylor (RT) mitigation and amount of precursor on-axis [22]. A large precursor on axis is not desirable as it hinders final compression and therefore x-ray production. However, the snowplow process helps to mitigate RT effects and improve symmetry, and more material on which the implo-

sion can occur, the better the instability control. Therefore, a balance for ablation rate must be found for these two effects in order for implosion to commence optimally, which, again, is theorized to be controlled during the initiation phase.

An important aspect of the implosion is that it can be observed on voltage signals as a time-dependent inductance that increases throughout the implosion. The material streaming in carries current with it, thereby decreasing the overall current radius. This current radius can be unfolded from voltage measurements, as described in section 3.2.2.

1.3.1.4 Phase IV (Stagnation)

The stagnation phase is when the main x-ray pulse occurs. The kinetic energy from the imploding material is converted to x-rays, and in some cases the x-ray output has been shown to be greater than the estimated kinetic energy of the imploding mass [38, 39]. Upon reaching the axis, the x-rays are generated from rapid thermalization of the material [40]. The sources of this thermalization are under study, but it is theorized that the energy comes from shock heating, PdV work and Joule heating [22]. The dynamics of the stagnation and x-ray production are one of the hottest areas of z-pinch study today, with significant experimental and computational efforts being invested.

Significant x-ray energy can be seen after the main pinch, and is typically ignored on larger machines (ZR) because it will not be useful for ICF work. However, on smaller machines such as COBRA, azimuthal asymmetries due to lower wire numbers typically have a deleterious effect on the FWHM of the radiation pulse, and it is expected that some of the late-time radiation seen on COBRA can be extracted on bigger machines. Therefore, descriptions of maximum energy from x-ray pulses will involve different definitions of the length

of the x-ray pulses when comparing typical Z and ZR results to those in this dissertation.

1.4 Motivation

The experiments in this dissertation were designed to study the impact of several parameters on the initiation and later stages of wire array z-pinches, and were motivated both by external experiments published in literature, and previous experiments conducted at LPS.

1.4.1 The importance of polarity, contact and current risetime

As described in section 1.3.1.1, previous research has shown that initiation is important to later stages of z-pinches. A proper understanding of initiation and its effects on ablation, implosion and stagnation is critical to moving forward with experiments on z-pinches.

This dissertation examines three main avenues to modify the initiation: polarity of the array with respect to ground, wire-electrode contact, and current risetime. While many papers can be found discussing the impacts of these factors on initiation and ablation [26, 30, 31, 27, 41, 42, 43], and other papers can be found discussing the importance of various aspects of ablation on implosion and stagnation [36, 37, 44, 45, 28], little has been done to carry experiments modifying initiation all the way through to the impacts on x-ray production. The experiments conducted for this dissertation aim to do just that: develop the understanding of the effects of polarity, wire-electrode contact and current risetime on initiation, and the impacts of these and initiation as a whole on the x-ray production. The hope is that, using these techniques on conventional pulsed

power generators, we can show an improvement in x-ray yield using modifications to polarity, contact and/or risetime. Therefore, design limitations on future z-pinch fusion reactors can be relaxed and costs can be reduced, making the dream of ICF closer to reality.

1.4.1.1 The effects of polarity

Present day pulsed power machines are operated in negative polarity due to the effects described in section 2.5.2. Therefore, the electric field at the load points from the return current posts to the load, enhancing electron emission and causing electrons that are emitted from the wires to be pulled away from the array [25, 28, 46, 41]. Current theories state, and experiments have verified, that this will have a deleterious effect on initiation, because the emitted electrons can interact with the gases desorbed from the wire cores, causing the ionization of the coronal plasma to occur earlier than if it were induced only by Joule heating. Therefore, voltage breakdown will occur sooner and less energy will be deposited in the wire cores.

However, if the polarity at the wires is reversed then electron emission will be substantially reduced, and the coronal plasma formation that leads to voltage breakdown will be slowed, increasing energy deposited. Experiments on single wires in the low current regime have shown a beneficial impact to energy deposition by operating in positive polarity [25, 42, 46].

1.4.1.2 The effects of contact

ress" contacts, whereby the wire is weighted and pulled against the solid electrodes to establish contact [25, 43]. This form of contact has been shown to have a higher contact resistance between the wire and electrode [47]. With such poor

resistive and inductive quality to the contacts, present theories state that the sudden increase in voltage between the wires and electrodes from the onset of the current pulse will generate arcs. These arcs can, in turn, initiate ionization in the region surrounding the wires near the electrodes. This plasma can shunt current around the wire cores, thereby decreasing the energy deposited in the wires around the region of the electrodes. This effect has been shown in low current, single wire shadowgraphic data as a tapered structure to the expanding wire cores [25].

If contact is improved at the wire-electrode interface, these arcs will be mitigated or eliminated altogether. Improving the contact at the electrodes by soldering has been shown to reduce this effect and make the expansion of the wire cores more uniform. The effect also moves with the electrode soldered (soldering the anode improves expansion at the anode, soldering at the cathode improves expansion at the cathode), and the greatest improvement to expansion uniformity was shown by soldering both electrodes. An improvement in energy deposited was also seen when the cathode was soldered, and when both electrodes were soldered (soldering the anode had little effect on energy deposited).

1.4.1.3 The effects of current risetime

Modern day pulsed power generators are very expensive. The 26 MA, 100 ns ZR driver was initially projected to cost $60 million, but costs were raised to ~$90 million [1]. Much of this cost goes into design and construction elements related to making the driver faster. Minimizing inductance requires very tight tolerances and computer designed parts, which carry a large price tag. Present theories state that radiation requirements for an ICF driver will require not only the high maximum amperage (60 MA), but also a very fast risetime (< 100 ns)

[22]. Therefore, efforts have been aimed at determining optimum current risetimes for a potential z-pinch ICF driver. If slower risetime machines can show similar x-ray powers and yields to fast risetime machines, design limitations on risetime can be relaxed, drastically reducing costs. We are examining whether operating an array in positive polarity and improving wire-electrode contacts via soldering can improve the x-ray output of a slower risetime machine such that it can compete with an array operated on a faster risetime machine.

1.4.2 Low-current, single wire experiments at Cornell University

The initial experiments at Cornell University to study polarity, contact and risetime effects to exploding wire experiments were in the low current, single wire regime [25]. These experiments were conducted on the pulsed power generator Low Current Pulser 3 (LCP3). LCP3 was the third and final machine in the Low-Current Pulser family of generators, which were designed to simulate the prepulse conditions of a single wire on Z (-200-0 ns using Z timing conventions). The prepulse on Z was mainly capacitively-driven displacement current from the final output switches. This prepulse phase ended when the output switches closed and the main load current started to conduct, but by this time the initiation phase had completed. Additionally, some ablation occurred near the end of the prepulse. LCP3 was designed to investigate the nature of the changes to one single wire of the entire array during this low-current (1-8 kA/wire) phase (Figure 1.2).

LCP3 was driven by a single 220 nF capacitor charged to 20 kV [25]. The risetime was varied by means of external inductors ranging from 0.2 to 2 μH, yield-

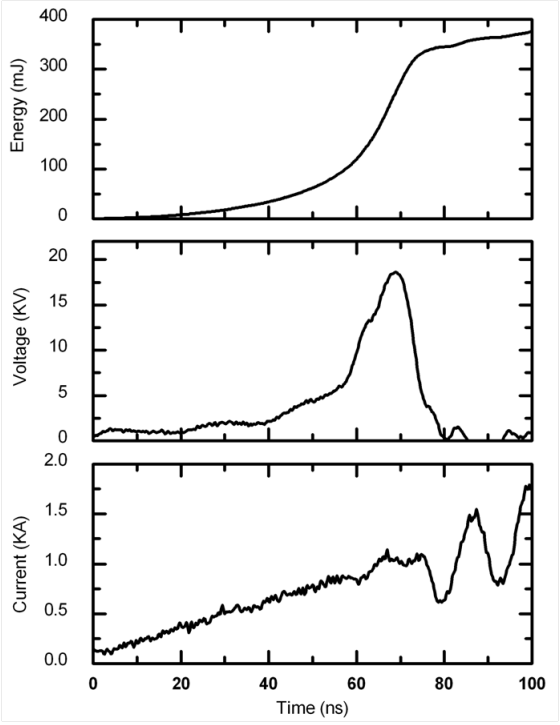

Figure 1.2: Typical LCP3 current, voltage and deposited energy traces. Reprinted from Duselis, et al.

ing current rise rates from 5 to 60 A/ns. The wire was mounted between two copper electrodes, which were capable of adjustment from wire lengths of 1-3 cm, but were typically set at 2 cm (the present standard for wire array height). The low current and voltage on LCP3 allowed the use of a resistive voltage divider and Pearson Rogoswki monitor, which gave highly accurate current and voltage measurements compared to larger pulsers. A Nd:YAG Q-switched laser and imaging system were employed to give shadowgraphy data. The small size and simplicity of LCP3 allowed for a high rep-rate of 5-10 shots/day.

LCP3 has been used to examine a variety of interesting initiation effects, including the effects of wire material, the existence and nature of the coronal plasma generated during initiation, and energy deposition [25]. More recently, experiments were conducted to determine the effects of polarity (positive vs.

negative with respect to machine ground), wire-electrode contact (non-soldered, or "press," vs. soldered) and current rise rate (5-60 A/ns) on the dynamics of initiation.

These effects were diagnosed by determining the electrical energy deposited in the wires up until the point of breakdown; current and voltage were multiplied to give instantaneous power, which was integrated in time from the beginning of current rise to voltage breakdown. These values for deposited energy were then compared across the parameter-space.

The laser shadowgraphy system gave two images per shot, allowing quantitative measurements of velocity and qualitative observations of structure to be made.

The following is a summary of the results obtained from these measurements, an in-depth analysis of which is available in Reference [25], which were the motivation for the experiments presented in this dissertation:

1. Wires operated in positive polarity had 40%-100% more deposited energy than wires operated in negative polarity.
2. Soldering the wire to the electrode improved energy deposited and uniformity of expansion, but only in positive polarity.
3. Soldering an electrode improved uniformity of expansion of a portion of the wire near that electrode.
4. The cathode was more important than the anode when maximizing energy deposited, but soldering both electrodes produced the most energy deposited.
5. Deposited energy increased as di/dt increased, from 5 A/ns to the LCP3 maximum of 60 A/ns.

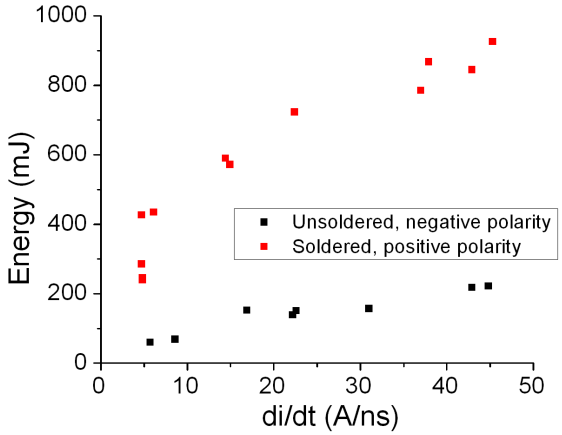

Figure 1.3: Best vs. worst case scenarios for low-current, single wire experiments conducted on LCP3

6. These effects were evident in aluminum, copper and tungsten wires, but the relative amount of improvement observed was different for the different wire materials, with aluminum showing the greatest improvement.

7. The highest relative improvement in energy deposited was observed with a positive, soldered, high di/dt aluminum wire.

Figure 1.3 exemplifies the final item in this list: positive, soldered, high di/dt experiments represent the best possible case, and show a substantial improvement in deposited energy over negative, non-soldered, lower di/dt cases.

1.4.2.1 Scaling single wire experiments to z-pinches

As an isolated experiment, LCP3 results are interesting, but they carry even greater weight if the results from low-current, single wire work scale to larger experiments. Therefore, along with investigating the direct effects of polarity, contact and current risetime on wire array z-pinches, we were implicitly investigating whether low current, single wire results are relevant to higher current, wire array z-pinch experiments.

1.4.3 Questions explored for dissertation

Given the above, the following list summarizes the questions we asked while conducting our experiments:

1. How does the bolt-on convolute perform on COBRA during z-pinch experiments?
2. What are the effects of polarity, wire-electrode contact and current risetime on the initiation stage of wire array z-pinches?
3. What are the effects of polarity, wire-electrode contact and current risetime on the later stages of wire array z-pinches?
4. What are the impacts of initiation on later stages of wire array z-pinches?
5. Of what importance to wire array z-pinches are low current, single wire experiments?

Before delving into the research aimed at answering these questions, an introduction to COBRA, the pulsed power generator on which these experiments were conducted, is prudent; chapters 2-5 will accomplish this. The experiments and results developed for this dissertation will be presented in chapters 6 and 7. We will present our conclusions and recommendations for future work in chapter 8.

CHAPTER 2

DESCRIPTION OF COBRA

After conducting initial, single-wire experiments on LCP3, we moved up 2 orders of magnitude in current (from 10's of kA to 1 MA), and conducted experiments on COBRA with 16 wire cylindrical z-pinch arrays. LCP3 is an effective machine at examining the dynamics of single wires in the low-current regime, but 8 kA is not enough current to drive wire-array z-pinch experiments. COBRA, on the other hand, is a nominal 1 MA, 100-200 ns variable risetime pulsed power generator capable of driving up to 16-32 wire z-pinches, and generating 300-500 GW of total x-ray power [15]. The variable nature of the current risetime of COBRA comes from the four independent output switches, described in more detail in section 2.2. There are three typical current pulses seen on COBRA: the 100 ns "short pulse," the 200 ns "double-humped" pulse (herein referred to as the "long pulse") and the 200 ns monotonically rising pulse obtained only through laser triggering. These three current pulses are shown in Figure 2.1

2.1 Layout of machine

The delivery of a 1 MA, 100 ns current pulse to the load requires substantial device integration and time-precision [13]. In order to facilitate the immediate need for an understanding of the COBRA layout (Figure 2.2), we will follow the generation of the current pulse from the capacitor banks to the load (Figure 2.3), ignoring any previous components, saving their description for section 4.1 (e.g. machine trigger events, diagnostic synchronization, etc.). For reference, a simplified lump circuit element diagram of COBRA is shown in Figure 2.4.

COBRA was designed using the popular Marx bank as the main current-generating mechanism (Figure 2.5). A Marx bank is a specific assembly of ca-

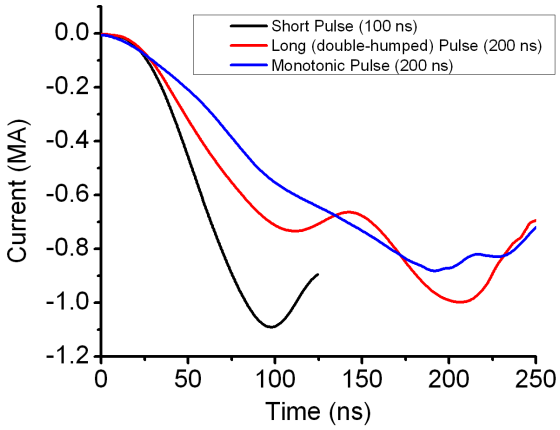

Figure 2.1: COBRA current pulses

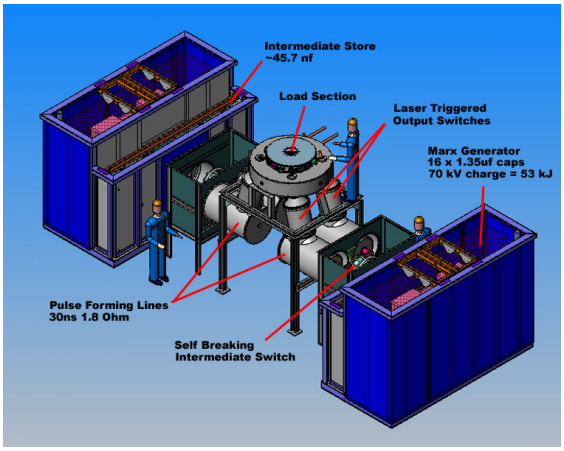

Figure 2.2: CAD rendering of the COBRA pulsed power generator.

pacitors (in our case, 16 capacitors per bank, each 1.35 μF, for a total stored energy of 53 kJ) resting in transformer oil. The capacitor, spark-gap switch, and resistor layout allow the capacitors to be charged in parallel by the two positive and negative 70 kV DC power supplies (Figure 2.5, top). The Marx erection is controlled by a series of cascading breakdowns through triggered Sulfur Hexafluoride (SF_6) insulated spark-gap switches. Upon closing the switches, the discharge times are short enough and the resistors are of a high enough resistance (1-10 kΩ, giving RC-times in the millisecond range) that the capacitors

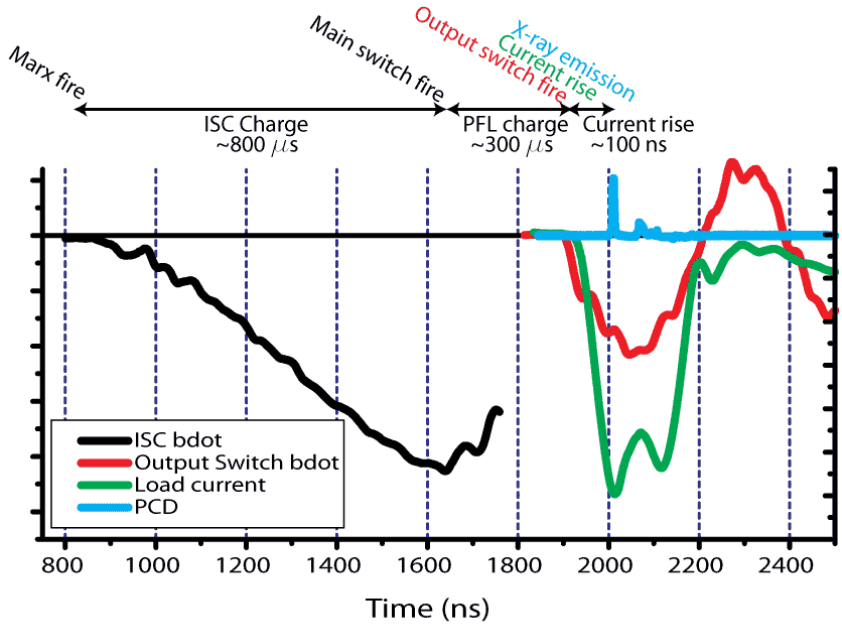

Figure 2.3: Current waveforms of the various stages in COBRA.

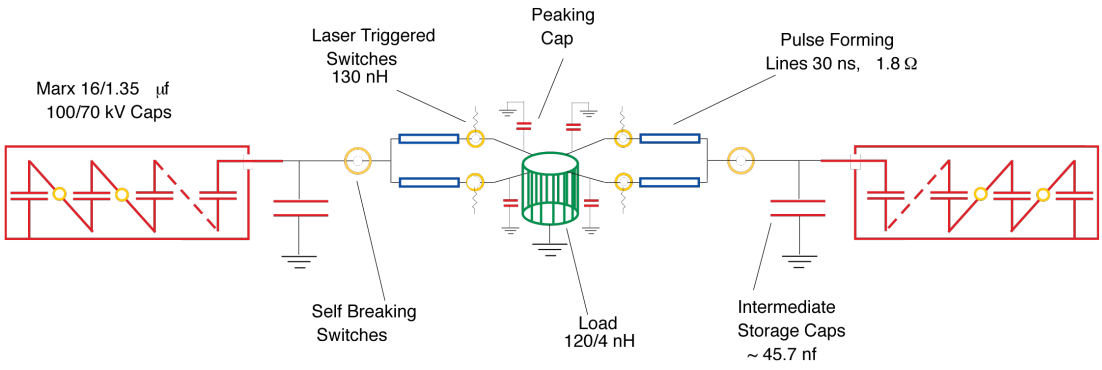

Figure 2.4: Electrical schematic of COBRA

are effectively discharged in series (Figure 2.5, bottom). This produces approximately 1.1 MV at the Marx output. For more information on pulsed power and switching, refer to section 2.4.

The energy in COBRA is stored in two diametrically opposed Marx banks, which are timed to fire simultaneously (jitter: ~60 ns). This means that, while describing any components before the current-adder stack, where the current

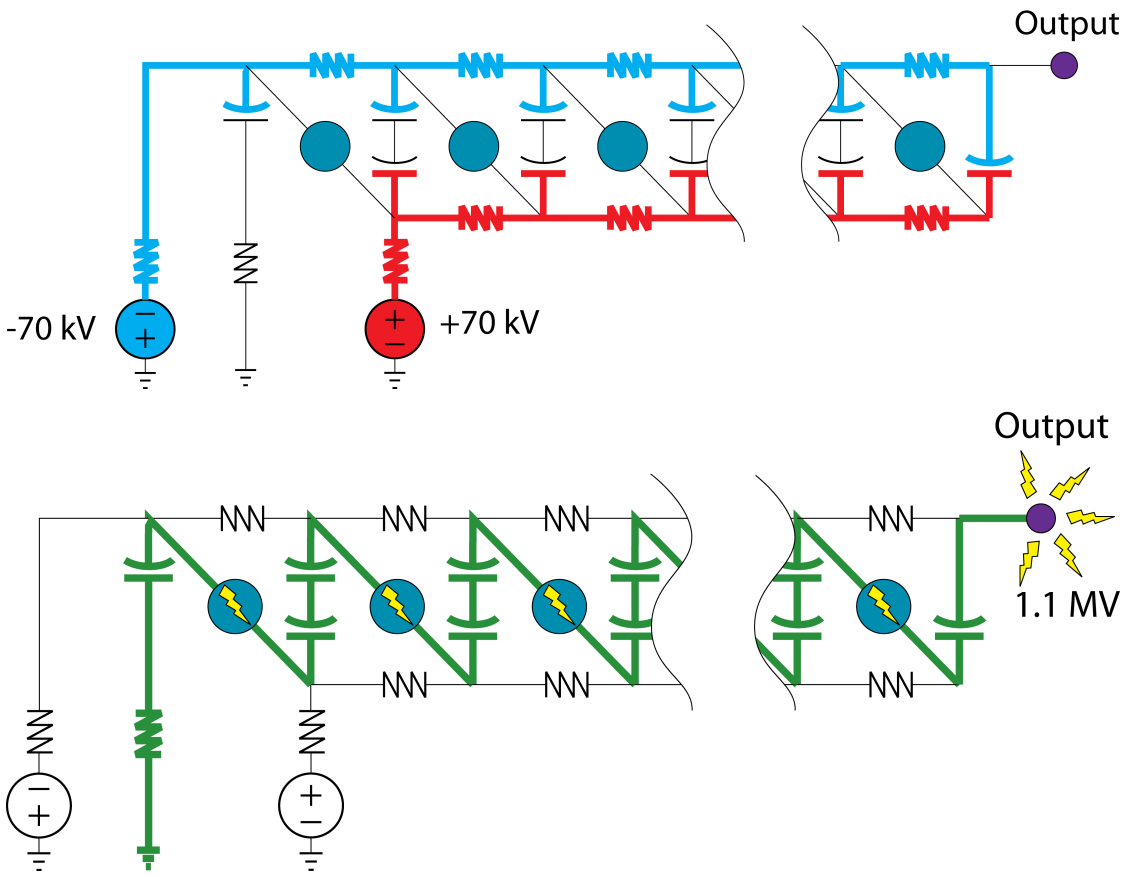

Figure 2.5: Simplified schematic of a section of the COBRA Marx bank: (top) charging and (bottom) firing. Note that there are some components missing from this diagram, excluded because they are not required for a simple understanding.

from both of these banks was combined, there are two such components in COBRA that are mirror images of each other (two Marx banks, two intermediate storage capacitors, two main switches and two sets of pulse forming lines).

Each capacitor in the Marx bank is charged to 70 kV, so the resulting voltage upon erection at the output end of the Marx bank is approximately 1.1 MV (16*70 kV). The Marx banks are discharged such that the output voltage of the Marx is negative with respect to ground. This voltage initially charges a water-dielectric, low inductance 46 nF Intermediate Storage Capacitor (ISC). The low inductance of the ISC shortens the risetime of the pulse to subsequent stages,

relaxing design limitations on the Marx banks.

The ISC is switched-out after ~800 ns of charging, at near peak voltage, by the self-breaking SF_6 filled spark-gap main switch (jitter: ~40 ns), and feeds into two parallel, water-dielectric, coaxial Pulse-Forming Lines (PFLs). These PFLs each have an impedance of 1.8 Ω and a transit-time of 30 ns. These lines charge for ~300 ns, at which point the SF_6 insulated output switches fire either by voltage-induced self-breakdown (jitter: ~20 ns) or laser-triggering (selected by the operator, jitter theoretically <10 ns). The combined impedance of the four 1.8 Ω PFLs, if fired simultaneously, is approximately 1/2 Ω.

The output switches, which are housed in transformer oil, feed the current from the PFLs into the water-insulated current-adder stack ("adder"), where the current from each of the four PFLs is combined (Figure 2.6). The adder was designed for a constant impedance per unit radial length of 20 Ω. The current then feeds through a vacuum interface to a center cathode plate sandwiched between two anode plates (at ground), all in vacuum, configured in a biconic triaxial (three-plate) geometry. The final stage before the load is the post-hole convolute (there are six posts that electrically connect the two anode plates to minimize inductance), where the final load-current and -voltage measurements are obtained, and the final conversion to coaxial geometry is made.

2.2 Variable risetime feature

The timing of the four COBRA output switches determined the nature of the final current pulse. For the short pulse mode, all four switches must fire simultaneously. This can be achieved most reliably with laser triggering, but COBRA has functioned in this short pulse mode for several years without laser triggering but with reduced repeatability. Laser triggering involves triggering each

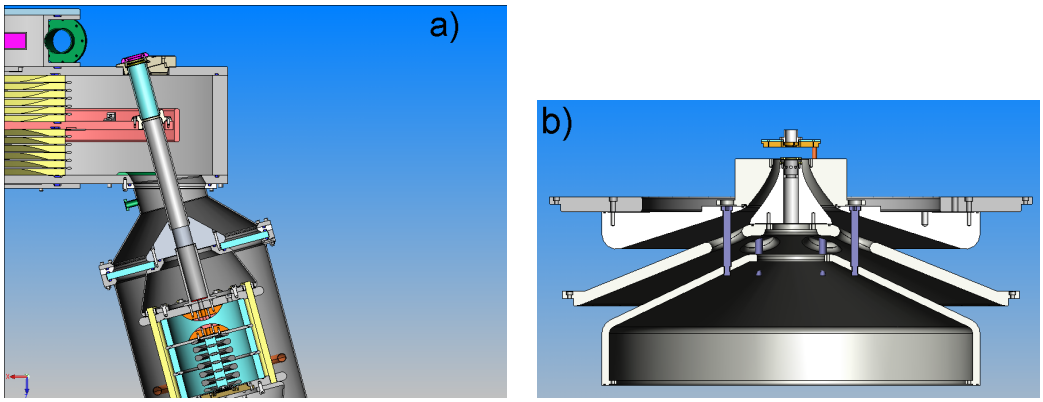

Figure 2.6: COBRA (a) output switch assembly and (b) vacuum adder stack

switch independently with its own 266 nm laser beam [48, 49, 50]. Alternatively, the switches can be set to different SF_6 pressures for self-break, which provides less control of the relative timing (for traces of these current pulses and a description of how they were used in the present experiments, refer to section 5.1). COBRA can produce fairly reliable 100 ns and 200 ns "double-humped" pulses in self-break mode, but laser triggering is necessary to produce the 200 ns monotonically rising current pulse.

The double-humped 200 ns pulse is achieved by lowering the SF_6 pressure in one of the main switches by ~3 lbs/in^2 (approximately 10%), and leaving the pressures in the output switches the same. This causes the second pair of output switches to fire ~100 ns later than the first pair. The timing of this results in two pulses of negative di/dt (remember that the machine is charged negatively) each about 100 ns long, separated by ~10 ns of positive di/dt. This results in a current profile with two distinct humps (one local peak at ~100 ns, the other at the peak total current time of 200 ns), with a small dip in the current at ~100 ns due to the brief positive di/dt. The ring-back voltage from the first set of PFLs to close acts to increase the voltage across the remaining switches, enhancing

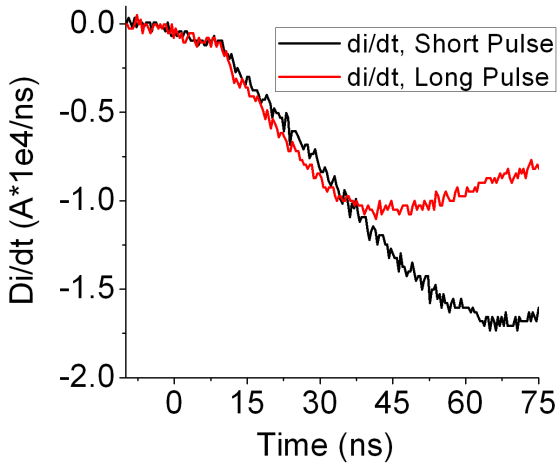

Figure 2.7: COBRA early time di/dt and current are similar for long and short pulses due to voltage source effects

the self-break condition. This makes the profile of the double-humped pulse very repeatable.

The monotonic pulse eliminates the possibility of quirky physics due to the variable di/dt throughout the current pulse or the period of positive di/dt in the double-humped pulse. The monotonically rising pulse is only possible with laser triggering of the output switches, as the back-voltage generated on a non-fired PFL works to reduce the total voltage across that line's output switch, thereby constraining the timing of its self-breakdown with gas. The monotonic pulse will be a valuable asset of COBRA in the future, but was not operational during the experiments presented in this paper, so it will not be discussed in detail.

2.3 Early time current

Figure 2.7 shows an important similarity of the early-time currents, as measured at the load, of the short and long pulse. Before voltage-induced breakdown, a

typical wire array has an extremely high impedance due to the small diameter of the wires. Until plasma forms around the wires, this inductance dominates the series combination of the array and machine-feed inductance (which is approximately 10 nH). Once plasma forms around the wires, the array inductance drops into the 10 nH range as well. As the current from COBRA starts to rise, it reaches a point when the decreased load impedance causes the generator to stop behaving like an ideal voltage source (approximately 35 ns into the pulse), and the currents from the short and long pulses diverge.

This effect is important because, on COBRA, there is no difference between the short and long current pulses during the initiation phase. Therefore, while we considered risetime to be a variable in experiments described in later chapters, it was actually not a variable specifically in the initiation phase. This helped to determine when during the current pulse effects manifested themselves (initiation vs. ablation, etc.).

2.4 Switches in pulsed power machines

The current and voltage between stages in COBRA is held-off by SF_6 insulated spark-gap switches [51]. These switches contain two electrodes of various materials, with SF_6 gas insulating the ~1-2 cm gap between them that holds off the ~100 kV per gap voltages. The voltage-holdoff capabilities of SF_6 can be determined for various pressures from empirical data [52]. SF_6 is a desirable switch gas due to its high electronegativity and high voltage hold-off characteristics [53].

The two types of spark-gap switches employed on COBRA are triggered and self-break switches. Triggered switches are designed with a separately applied electrical overvoltage or laser-induced breakdown that initiates an arc be-

tween the two electrodes. The voltage across the gap then begins to conduct current through this arc, rapidly decreasing the impedance and closing the switch. Therefore, the timing of a triggered switch is controlled by the firing of the trigger mechanism. A self-break switch, on the other hand, is closed when the voltage across the electrodes reaches the electric field breakdown strength of the insulator gas, and an arc channel spontaneously forms. The timing is controlled by the pressure of the SF_6 insulation gas. Self-break switches typically have more jitter, and take longer to close, than their triggered counterparts. However, triggering schemes, especially laser triggering, can be very expensive, and self-break switches are inherently simple and robust.

For self-break switches and in the regimes used on COBRA, a fairly linear relationship exists between pressure and voltage hold-off (e.g. a 10% increase in total pressure corresponds to a 10% increase in the voltage that can be held off). If the voltage is rising quasi-linearly, then this linear relationship of voltage and pressure extends to the time of switch-out (e.g. a 10% increase in total pressure corresponds to a 10% increase in the charging time).

2.5 Notes on the use of pulsed power insulating materials (dielectrics)

The choice of insulating material used between a high-voltage conductor and ground on pulsed power machines is critical to proper performance. The two important things to consider are the relative dielectric constant and breakdown strength. However, it must be noted that the choice of insulating material, as with every design choice in pulsed power, cannot be made by only considering these aspects independently. All potential impacts must be taken in concert with

Table 2.1: Relative dielectric constants of various insulators used in COBRA. Data obtained from Martin et al. (1996), and Peek et al. (1920).

Insulator	$\epsilon_{relative}$
De-ionized Water	80
Transformer Oil	2.4
High vacuum (<5e-5 Torr)	1

the overall objectives for the machine design, and typically require extensive computer simulation. Therefore, the descriptions below are drastically simplified and one-dimensional, but may help the reader to better understand some of the reasons for the complicated transitions between insulating materials.

2.5.1 Dielectric constant

The dielectric constant (see table 2.1) affects two aspects of the typical geometries used: transit time and capacitance. These data were obtained from References [5, 54].

The insulating material plays an important part in controlling the capacitance. For example, parasitic shunt-capacitance in the final vacuum feed is undesirable as it limits current delivered to the load, so the low ε of vacuum is desirable. However, energy storage in the ISC and PFLs is the main design requirement, so a high-ε material, such as water with $\varepsilon_{\text{relative}} \approx 80$ is used. The high dielectric constant of water is also useful in the adder, creating a "peaking capacitor" between the outer annulus of the center plate and the outer cylinder of the adder. The peaking capacitor has a capacitance of 14 nH, and allows the high-

inductance output switches to conduct some current before and during closure, decreasing the time it takes them to close and improving current delivery to the load. Control of capacitance through dielectric selection can also be used to mitigate current prepulse on the load, which is often a problem due to capacitive coupling between the PFL and output stages before the output switch has closed. On COBRA, this isolation is accomplished by placing the output switch in an intermediate oil-filled stage between the water-filled PFLs and adder. This escalates cost and design requirements, but is very beneficial to the final output current shape.

Higher dielectric constant materials also increase transit time of electromagnetic wave propagation. This can be useful when space constraints exist and sections must be made shorter. For example, the PFLs on COBRA are ~6 ft long, but the water insulation means that their effective length is closer to 50-60 feet when compared to the same geometry but with vacuum as a dielectric. This increased transit-time effect also allows the water in the adder to provide temporal isolation for the four output switch connections. Therefore, each switch has more time to fire independently without back-voltage from previously fired switches, a benefit to its switch-out characteristics.

A summary of the insulating materials used in the COBRA stages and their primary function is given in Table 2.2.

2.5.2 Electric field breakdown strength

The electric field breakdown strength is another important characteristic of insulating materials when calculating geometries and tolerances. Insulating material breakdown strengths are highly dependent upon both the time-evolution of the electric field across the material (or lack thereof with vacuum), as well

Table 2.2: COBRA stages and insulating material

Stage	Insulator	Dominant insulator design requirement
Marx bank	Oil	High voltage hold off
		Low ε reduces shunt capacitance
ISC	Water	High ε increases capacitance
PFL	Water	High ε increases capacitance
Output switch	Oil	Low ε reduces shunt capacitance, prepulse
Adder	Water	High ε increases peaking capacitance
		High ε decreases cross-talk
Vacuum feed	Vacuum/	High electric field hold-off
	MITL effects	Low ε decreases shunt capacitance

as electrode shape and its impact on field enhancement. In addition to its importance, high-voltage breakdown in liquids is not completely understood, and often empirically-derived formulas are the only available sources for design. Entire books have been written on the subject (see references [55, 5]), and two very useful papers on this subject can be found in References [3] and [56]. Information on vacuum breakdown, which is beyond the scope of this document, can be found in Reference [57].

For the insulating liquids used on COBRA, the breakdown field of a short time-scale (μs) pulse can be estimated using the following formula (this formula has been revised several times since the first publication - this is its most current form) [53, 3, 56]:

$$E_{BD} = \alpha * K * A^{-n} * \tau^{-1/3}$$

Where E_{BD} is the breakdown field strength in MV/cm, τ is the time in μs for

Table 2.3: Values of empirically determined constants K and n for oil and water, used for calculating breakdown strength, Adler (1989).

Material (electrode polarity)	K	n
Water (positive)	0.23	0.058
Water (negative)	0.56	0.070
Oil (positive)	0.48	0.075
Oil (negative)	1.41	0

which the electrode is above 63% of the breakdown field, K and n are empirical parameters given in Table 2.3, A is the electrode area in cm^2, and α is a measure of field enhancement, given by:

$$\alpha = 1 + 0.12\left(\frac{E_{max}}{E_{mean}} - 1\right)^{1/2}$$

which we will we assume is ≈ 1 for our cylindrical geometries.

Readily apparent from these formulas is that oil has a higher dielectric strength than water for a given polarity. It has been suggested that the lower dielectric strength of water is a product of its dipole-nature and smaller molecule size, although this is not well understood.

The formulas also give a higher dielectric strength of oil and water on negative polarity electrodes. This result is empirical, and a debate continues as to the reason. Regardless of its physical source, this polarity effect is the reason that modern pulsed power generators have been constructed in negative polarity. For a positive polarity electrode to have an equivalent voltage hold-off to its negative polarity counterpart, all other parameters being equal, the spacing would have to be approximately three times larger, having a cascading impact on capacitance and inductance design parameters. This would drastically in-

crease size and therefore cost.

These formulas were derived for μs scale voltages. However, the Marx bank is operated in DC, and therefore one must use the typical guideline of 40 kV/cm for the breakdown electric field of transformer oil [53].

It should also be noted that breakdown strength is not highly dependent upon purity of the insulating material. Therefore, oil filtration or dehydration is rarely necessary to maintain electrical properties. However, water must constantly be filtered and de-ionized to reduce Ohmic loads on the machine, not to improve its voltage hold-off [3]. For the reason, COBRA must be fired with the DI water filtered to a resistivity above 1.0 MΩ-cm.

Vacuum electric field hold-off is also very complicated, and is beyond the scope of this document. However, Reference [53] states that, for perfectly clean aluminum and stainless steel electrodes (not typical of the electrodes in use on COBRA), the electric field hold-off is approximately 300 kV/cm. However, in order to keep inductance acceptably low, it is also necessary to stress the vacuum feed beyond the cathode emission threshold (~100 kV/cm). Thus, self-magnetic insulation is essential to couple the generator to the load. Magnetically insulated transmission lines as used on COBRA are discussed in more detail in section 5.3.

CHAPTER 3

COBRA DIAGNOSTICS

COBRA was fielded with a variety of diagnostics to study all phases of wire array z-pinch dynamics [16]. The functions of the diagnostics used in the experiments presented here are described below.

3.1 Current monitor

The current monitor was a homemade Rogowski coil mounted ~8 cm below the COBRA output. A Rogowski coil is essentially a helically wound wire, which is then wrapped around the source of current to be measured. The ends of the wound wire are the final terminals across which the voltage measurement is obtained. If the lines of magnetic-flux are perpendicular to the circular surfaces of the turns, a di/dt in the source induces a voltage in each turn, and the total voltage induced across all the turns is proportional to the total number of turns. Since the measured value is proportional to di/dt, the signal must be mechanically self-integrated on the diagnostic or numerically integrated during later analysis. There are several variations on the design of the Rogowski coil, including one where the wire is wrapped back around itself, eliminating any contribution from magnetic fields with field lines normal to the large, outer diameter of the coil. Different cores through the windings can also be used to give the same effects as the various cores used in transformers. One of the greatest advantages of the Rogowski coil is its insensitivity to positioning around the source to be measured.

3.2 Voltage monitor

The inductive voltage monitor employed was a high-inductance wire connected from the current feed ~11 cm below the load to ground [13]. This monitor sapped a small portion of the load current, and this current was measured by an adjacent $\dot{B}$ probe near the end of the feed. The raw output gave:

$$V_{raw} = IR + \frac{d}{dt}(LI)$$

The inductance (L) includes both the (non-varying) machine inductance ($L_{machine}$) downstream of the voltage monitor and the (varying) array inductance ($L_{array}(t)$) [15]. R represents the ohmic resistance of the array, and I is the total current through the load. This voltage signal, $V_{raw}(t)$, was used to obtain several very important pieces of information: the ohmic power and energy input, the time of voltage collapse, and an effective current radius of the array [58, 19].

The chain rule allows us to break V_{raw} into the following components:

$$V_{raw} = IR + L(t)\frac{dI(t)}{dt} + I(t)\frac{dL(t)}{dt}$$

3.2.1 Voltage monitor during initiation - calculation of energy deposited

During initiation the array inductance is essentially constant, and this inductance, along with the machine inductance, can be estimated from the geometry, yielding L_0. Since we have experimentally determined dI/dt, and assuming that $L=L_0$ is constant (only during initiation), we can subtract the L_0*dI/dt term. During initiation, we can also assume that dL/dt is negligible because there is no movement of the wires, so any remaining voltage we see is resistive:

$$V_{raw} - L_0 \frac{dI(t)}{dt} = IR$$

This formula is only valid during the initiation phase before the array inductance has changed at all, and can be used to determine the time of, and voltage achieved at, voltage collapse. The results of this analysis are used to compare initiation phases between arrays, as differences in the resistive voltages are compared from shot to shot. The energy deposited can be calculated from this resistive voltage and measured current, and compared to the energies required to melt, vaporize and partially ionize the wires.

Energy deposited can be compared to the amount of energy required to convert the wires from a solid to liquid or vaporized state. The energy required to melt the wires is composed of the energy required to raise the temperature of the wires from room temperature to the melting point, and then the latent heat of fusion of the amount of mass in the array.

$$E_{melt}\,[eV] = (C_s * \Delta T_{start-melt} * N_{moles}) + \left(L_m * N_{array}\right)$$

The energy required to vaporize the wires is composed of the melting energy, the energy required to raise the temperature of the wires to the boiling point, and the energy required to vaporize the material.

$$E_{vaporize}\,[eV] = \left(C_l * \Delta T_{melt-vaporize} * N_{moles}\right) + \left(L_v * N_{array}\right)$$

These two energies, T_{melt} and $T_{vaporize}$ can be added to give the total amount of energy to vaporize the wires. The values required for these calculations are shown in Table 3.1, and were obtained from Reference [59].

We have also calculated a factor to convert from energy in Joules per shot to Energy in eV/atom for the particular array used in these experiments. This conversion factor was calculated as follows, and also used values in table 3.1.

$$E\left[\frac{J}{array}\right] = \frac{C_{eV}}{N_{array}}$$

The result, for a given number of Joules deposited in our specific, 16x12.5 μm diameter aluminum wire array, is 1 J/array = 2.6376 eV/atom. Using this conversion factor, the Joule-energy deposited in an array (the direct output of the current and voltage measurements) can be compared to the values listed in Table 3.1 for energies to transition from room temperature to melted and vaporized.

After vaporization, the energy required to ionize the first electron from an aluminum gas is an additional 5.986 eV [59]. The energy required to fully ionize aluminum is on the order of 12 keV/ion [40], or many orders of magnitude above the energies with which we are dealing in the initiation phase.

3.2.2 Current radius unfold

After voltage collapse, plasma has formed around the wires, and some current begins to move in towards the array axis (assumed to be at an unspecified time). Therefore, the assumption that the inductance has not changed is no longer valid. However, we used another analysis technique to obtain the effective array radius from the $V_{raw}(t)$ signal. This technique involves integration of $V_{raw}(t)$ and some simple algebraic manipulation. The result is a formula for $L_{array}(t)$, which is unfolded to obtain $R_{current}(t)$.

As above, the raw voltage signal is assumed to be a serial combination of an initial, unchanging machine inductance, and a variable load inductance.

$$L(t) = [L_{machine} + L_{array}(t)]$$

Table 3.1: Thermodynamical and other properties of aluminum used to calculate energy required to melt and vaporize array from room temperature. These values were obtained from Weast et al. (1988).

Thermodynamical properties of aluminum/array	Symbol	Value	Unit
Density	ρ	2.7	g/cm^3
Mass of array	m_{array}	6.62	μg
Molar mass of aluminum	m_{mole}	26.9	amu
Number of atoms per array	N_{array}	$2.3658e^{18}$	atoms
Number of moles per array	N_{moles}	$3.9299e^{-6}$	# Moles/array
Starting temperature	T_{start}	295	K
Melting point	T_{melt}	933	K
Boiling point	T_{boil}	1333	K (at 10^{-3} atm)
Latent heat of fusion, Al	L_m	0.1106	eV/mole
Latent heat of vaporization, Al	L_v	3.0474	eV/mole
Specific heat, solid aluminum	C_s	$1.5145e^{20}$	eV/(atom*K)
Specific heat, liquid aluminum	C_L	$1.8314e^{20}$	eV/(atom*K)
Conversion factor Joules to eV	C_{eV}	$6.24e^{18}$	N/A
Conversion factor Joules/array to eV/atom		2.6	N/A
Energy to transition from room temp to melted		0.27	eV/atom
Energy to transition from room temp to vaporized		3.4	eV/atom

The calculations and integrations of this technique are chosen to start immediately after resistive voltage collapse, so it is assumed that there is no contribution from resistive voltage (set IR=0) due to low plasma resistance (Spitzer resistivity estimates I*R on the order of 1 and L*di/dt on the order of 10^5).

The assumption must also be made that there has been no inward movement of current up until the time of voltage collapse, which allows us to use the array's initial, calculated inductance, L_0, at the time of voltage collapse. This is a reasonable assumption, as the current is still confined to the original wire locations, and the calculation of inductance is based upon geometry.

This technique is written in equation form below:

$$V_{raw}(t) = \frac{d}{dt}\Big[\Big(L_{machine} + L_{array}(t)\Big)I(t)\Big]$$

$$\int_{t_0}^{t_1} V_{raw}(t)dt = \Big[L_{machine} + L_{array}(t_1)\Big]I(t_1) - \Big[L_{machine} + L_{array}(t_0)\Big]I(t_0)$$

$$L_{array}(t_1) = \frac{\Big[\int_{t_0}^{t_1} V_{raw}(t)dt\Big] + L_{machine}\Big[I(t_0) - I(t_1)\Big] + \Big[L_{array}(t_0) * I(t_0)\Big]}{I(t_1)}$$

t1 = final time to which we integrated (typically the time of implosion, but is valid as long as the current and voltage monitor signals are reliable).

t0 = time of voltage collapse.

If we assume a uniform, cylindrical sheath of current, $L_{array}(t)$ can then be unfolded to give the time-dependent array radius. The array radius was found from the following formula for inductance of a coaxial transmission line (a factor of 50 was included to account for a cylinder 2 cm high) [MKS]:

$$R_{current} = R_{return} * e^{-\left(\frac{100\pi L}{\mu_0}\right)}$$

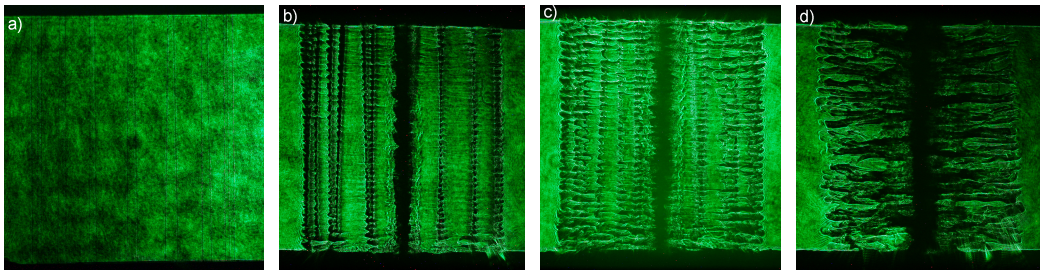

Figure 3.1: Typical COBRA backlighter images of a 16 mm , 16 x 12.5 μm φ aluminum array showing (a) pre-shot, (b) 112 ns, (c) 132 ns and (d) 157 ns.

The assumption that the current exists in a uniform cylindrical shell is clearly not correct when image data are taken into consideration, but provides a useful metric to compare the quality of various implosions.

3.3 Laser backlighter

Laser shadowgraphic images were taken using an EKSPLA SL312 Nd:YAG laser. This was a q-switched laser with a 250 mJ fundamental at 1,064 μm. The fundamental was internally frequency doubled to give a 120 mJ, 150 ps, 532 nm (green) second-harmonic pulse, which was split into three channels and delayed to give three beams each separated in time by ~10 ns. The beams were nearly colinear when aimed at the pinch to give nearly identical viewing angles. The shadowgraphic images were then attenuated and focused onto the image sensor of Canon EOS Digital Rebel XT cameras, where they were recorded for later analysis. Sample shadowgraphic images are shown in Figure 3.1.

The shadowgraphic images were obtained with a method similar to Schlieren imaging where the knife-edge or focal point block has been removed [60]. A collimated beam of light was passed through the plasma to be imaged. The plasma deviated different parts of the beam off normal by an amount that

was related to density-based refraction. Regions with greater density gradients refracted the beam further from normal that those with smaller density gradients. When collected by the lens, the regions that deflected the beam more appeared darker on the imaging plane. It must also be mentioned that this diagnostic was limited to observing plasma densities below the plasma cutoff frequency of the imaging light, which is given by the following formula:

$$\omega_p = \left(\frac{ne^2}{\epsilon_0 m}\right)^{1/2}$$

Where ω_p is the plasma frequency, n is the density, e is the electron charge, ε_0 is the permittivity of free space, and m is the mass of an electron. Using the wavelength of the imaging beam, 532 nm, in the calculation above gives a cutoff density of n=4x10^{21}/cm^3.

Laser backlighter images were compared based upon general shapes and sizes of various structures (precursor column, fundamental wavelength of streamers, etc.) and timing of pinch developments.

For timing purposes, the output of the laser is measured (near the laser head) with a pin-diode. There is a propagation delay between when this signal is observed and when the first laser beam is incident upon the array. This delay has been measured as 22.4 ns. Therefore, 22.4 ns must be added onto the pin-diode signal when read directly to obtain the time of the first image. The subsequent images were measured at +9 ns and +21 ns, which were determined by the path length between mirrors.

3.4 4-frame time-gated self-emission XUV camera

A 4-frame Multi-Channel Plate (MCP) camera observed the pinch with 4 ns exposures through 50 μm pinholes. This technique was similar to that used in

Reference [61]. This gave 4 ns time-resolved, self-emission, extreme ultraviolet (XUV) images separated in time by 10 ns. XUV refers to photons with energies in the 10-100 eV range.

The 4-frame camera was essentially a time-gated light amplifier. Incident photons from the plasma passed through the pinhole and were converted to electrons at the photo-cathode. These electrons were then accelerated and photomultiplied by a pulsed, high-voltage (1-10 kV) bias down an array of 12 μm channels, collectively called the micro-channel plate. These channels were 15 μm apart, which gave an effective resolution of 27 μm. The pulsing of this bias voltage was what accomplished the time-gating of the diagnostic, because the electrons were not accelerated down the MCP when no bias voltage was present. Therefore, the time-resolution was limited by the ability of the power supply to create a short, high-voltage pulse. The MCP output directly to a phosphor plate where the electrons were converted to light in the visible range via phosphorescence, and Kodak T400 film was placed against this phosphor plate to record the results. This film was developed in Kodak Microphen developer according to standard development procedures at LPS. A sample film from COBRA is shown in Figure 3.2.

4-frame images were compared based upon general shapes and sizes of various structures (precursor column, fundamental wavelength of streamers, etc.) and timing of pinch developments. The 4-frame camera also gave indications in some shots of an axial inhomogeneity called the "Christmas tree" effect [62]. This effect is characterized by accelerated dynamics of the wires near the cathode, an early pinch at the cathode, and the appearance of axial flow towards the anode. The Christmas tree effect is shown in Figure 3.2.

The lowest energy observed by the MCP is limited by the pinhole size ac-

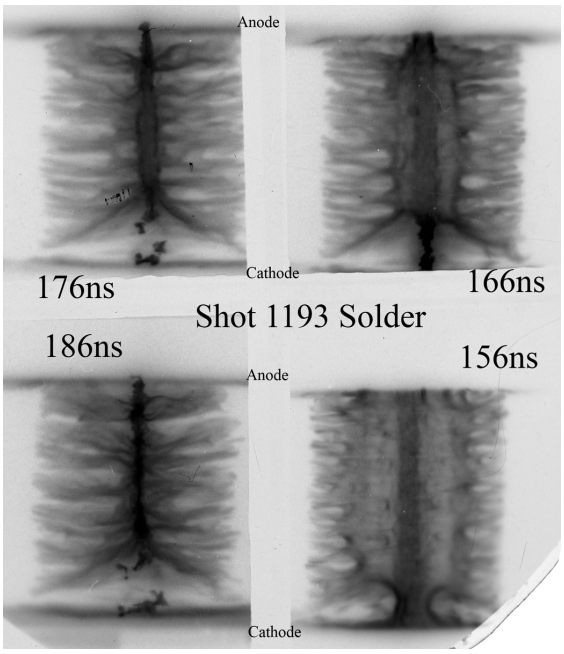

Figure 3.2: Typical COBRA 4-frame XUV self-emission camera film showing all four images from one 16 mm φ, 16 x 12.5 μm aluminum array. Note the Christmas tree effect, or early pinching, at the cathode. Also note that the images were digitally flipped horizontally and vertically to get the proper orientation.

cording to the following formulas [61]:

$$L_{diff} = 1.22\frac{\lambda p}{d}$$

$$L_{geometry} = d\left(1 + \frac{p}{q}\right)$$

Where L_{diff} is the smallest resolvable size due to diffraction effects, L_{geometry} is the smallest resolvable size due to geometry effects, λ is the wavelength of incident photons (related to energy), p is the object-pinhole distance, q is the pinhole-image distance, and d is the pinhole diameter. Light with any wavelengths (energies) below this value are cutoff by diffraction through the pinhole. The above formula predicts that the 50 μm pinholes with the geometries used on our experiments will cut off energies < ~20 eV.

3.5 Diamond photoconducting detectors

Photoconducting Detectors (PCDs) were used to obtain time-dependent x-ray powers from the pinch. A PCD is constructed by mounting a small piece of diamond between two electrodes and applying a large (typically 300V) DC bias across the diamond. The conductance of the diamond is dependent upon the incident x-ray power, has a nearly flat response from 10 eV up to 6 keV, and is theorized to have sub-200 ps time resolution [63]. This response is remarkably wide and flat when compared to x-ray detectors made of silicon p-n junctions, but the drawback is the high cost of the installed diamond. PCDs are also very robust and can have direct line of sight exposure to the pinch without being damaged by debris or x-ray flux. Filters can be placed in front of the PCD to give the desired low-frequency cutoff. The experiments described herein used the COBRA standard x-ray filter set: 2 μm and 6 μm of Mylar, and 12 or 25 μm of Beryllium, all in place on 3 different PCDs on every shot. The transmission data for these filters are shown in Figure 3.3.

A sample trace from a PCD during one of the shots presented here is shown in Figure 3.4. This trace can be directly converted to x-ray power, and can be integrated to give energy. If the PCD is properly calibrated these are absolute values, otherwise they can be compared only within the dataset or to other shots with that specific PCD. In this paper, x-ray output is used as a general term for power and energy, so a shot with improved x-ray output had both higher peak powers and more total energy in its x-rays.

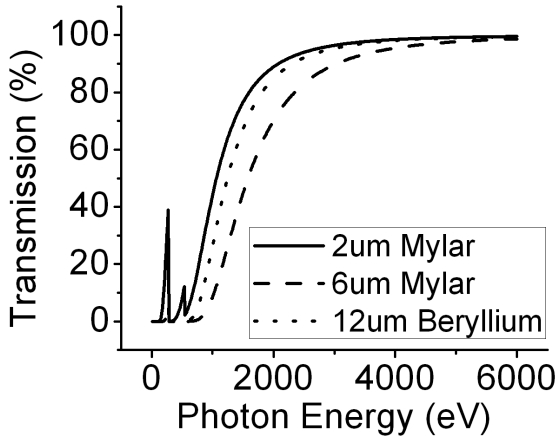

Figure 3.3: Transmission data for filters used on PCDs. Data obtained from Henke et al. (1993).

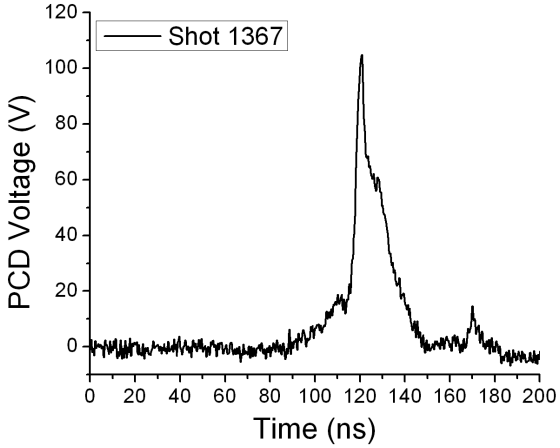

Figure 3.4: Sample collimated, 6 μm Mylar filtered PCD output from a typical COBRA short pulse shot

3.6 Bolometer

A fast nickel bolometer was used to give total energy emitted throughout the lifetime of the pinch [64]. The bolometer is a ~1 μm thick, 1-2 mm wide, 2 mm long strip of nickel deposited on a non-conductive (typically fused silica) substrate. The ends of the strip are then soldered to electrodes, and a 6 μs current pulse is applied through the strip from a well-regulated, constant current supply, while the voltage drop across the strip is simultaneously measured. The

current heats the strip, increasing its resistance and therefore the voltage across it, until it reaches an equilibrium between heat radiated and heat deposited by the current. If there is no incident x-ray flux, the current through the bolometer does not change and the voltage across the strip is constant. However, the strip will absorb incident x-rays, thereby heating it up, increasing its resistance, and showing a change in voltage.

The bolometer was unfiltered except for a permanent magnet to deflect charged particles, and therefore had a nearly flat response for radiation from 10 eV to 2 keV, above which the response began to decrease. The bolometer voltage change, which happens on approximately the 10 ns scale, can be unfolded to give the total x-ray flux, and is a good measure of the total energy emitted by a pinch.

When discussing total energy output from the pinch, only the energy change during the main x-ray pulse was used, and all data before and after this time period were ignored, as it was energy not emitted during the pinch. A calibration factor of 0.55 kJ/V was used to convert to total radiated energy, as discussed in Reference [15].

3.7 Visible streak camera

The operation and calibration of the visible streak camera is described in detail in Reference [65]. The camera was setup to give two streaks per shot: radial and axial. The streak camera was synchronized by a fiducial from the diagnostic laser. An optical fiber captured a reflection of the beam and, after some propagation delay through the fiber, output this pulse on the input of the streak camera streak. As a result, there was a bright, horizontal fiducial on each streak. The time of this fiducial was determined by considering the propagation delay

from the array to the streak camera input, which was 55.2 ns, and this optical fiber delay. The result is that the fiducial on the streak camera appeared 49.8 ns after the start of rise of the pin-diode signal measuring the laser output. This time can be used to synchronize the streak image with the load current.

CHAPTER 4

TIMING OF DIAGNOSTICS ON COBRA

Experiments on COBRA require a multitude of diagnostics to determine what was occurring during the pinch. In order to catch the proper events, these diagnostics require nanosecond timing accuracy with respect to the start of the current pulse. To accomplish this synchronization, a system was designed to control the timing and triggering of all aspects of the machine, including the actual trigger to the machine current itself.

Before describing the triggering system, a list of the timing and triggering requirements of each diagnostic is given below.

For in-depth explanations of the operation of the diagnostics, please refer to chapter 3.

4.1 Overview of timing needs of diagnostics on COBRA

The following section outlines the timing requirements of the various diagnostics on COBRA. These are summarize in Table 4.1.

4.1.1 COBRA

COBRA is triggered by the following sequence: 22V pulse to PT-55 (50 kV) pulse to TG-70 (70kV, higher current than PT-55) to Trigger Marx to Main Marx. The 22V pulse is an operator depressed button at the main control panel, and determined when the machine fired. There are several signal delays before the PT-55, but once the PT-55 is triggered, the self-break switching occurs independently of outside control, and current reaches the load ~1.8 μs later. Output timing signals are also retrieved from COBRA in the form of $\dot{B}$ signals from the PFLs, which start approximately 300 ns before current reaches the load. These $\dot{B}$ signals are

Table 4.1: Timing requirements of COBRA functional units.

Unit	Trigger	Time before load current
COBRA	PT-55	1.8 μs
Oscilloscopes	5 V	1.8 μs
Diagnostic laser "START"	5 V	1.5 ms
Diagnostic laser Q-switch	5 V	(-)100-(+)100 ns
Trigger laser flashlamp	0-5 V rising	128 μs
Trigger laser Q-switch	5-0 V falling	~400 ns
Visible streak	5 V	365 ns
PCDs	N/A	N/A
4-frame camera	40 V	50-150 ns
Rebel XT cameras	Cryo close	1-2 sec.
Bolometer	40 V	~2 μs

used by the Glory Box (explained in section 4.2) and diagnostics as low-jitter trigger signals, as described in section 4.2.

4.1.2 Oscilloscopes

The digital oscilloscopes, which record the data from each shot, require a rising-edge TTL signal for a trigger. They are set to record a window a significant amount of time before and after this trigger event, and therefore the exact trigger time is not critical, but have to be repeatable from shot to shot so that the same record window is acquired every shot. The trigger event selected for this event is the synchronization output from the PT-55 power supply, which sends a ~10V

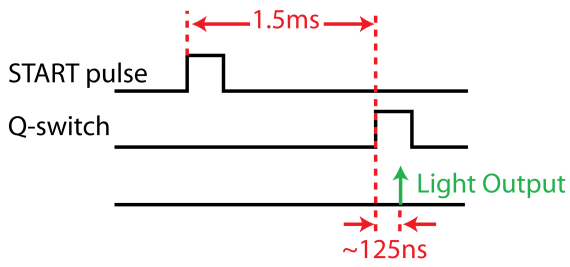

Figure 4.1: Diagnostic laser trigger pulses and laser output timing using EX1.

pulse simultaneously with the trigger for the PT-55. Therefore, the scopes are triggered approximately 1.8 μs before current reaches the load, and the record window and horizontal (time) scale are set accordingly.

4.1.3 Diagnostic laser

The trigger input needs of the diagnostic laser, an EKSPLA SL312, are all at TTL levels (5V). The diagnostic laser can be run in three different triggering modes, all described in its manual. The mode in which we operate the laser is called "External 1," and is designated on the control pad by "EX1." It requires two different input signals. A rising-edge TTL input pulse ("START") is required ~1.5 ms (±3 μs) before desired laser output, and must be a 10 Hz clock signal. The laser internally adjusts the flashlamp timing so that the desired amplification level is obtained if the Q-switch pulse comes 1.5 ms (±3 μs) after the START pulse (see Figure. 4.2). A second rising-edge TTL input pulse is required to trigger the Q-switching, and laser output occurs ~120 ns after this final trigger pulse.

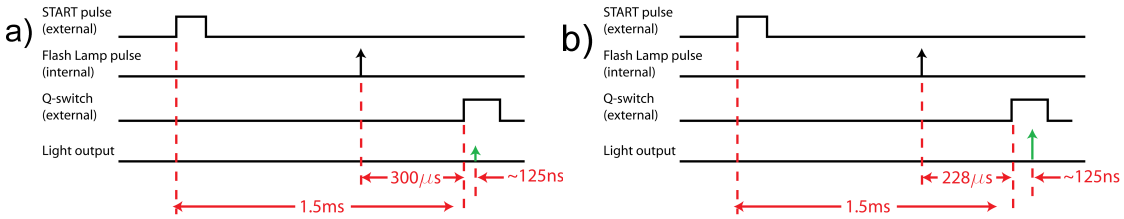

Figure 4.2: Diagnostic laser input and internal trigger pulses for (a) low and (b) maximum amplification using EX1.

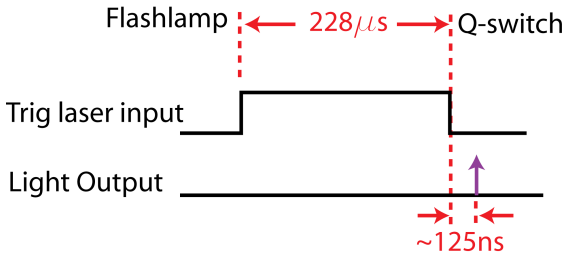

Figure 4.3: Trigger laser triggering pulse. The rising edge triggers the flashlamps, the falling edge triggers the Q-switch.

4.1.4 Trigger laser

The trigger laser, an EKSPLA NL303, also needs two TTL input trigger events, but they must both be on the same cable. The laser can operate from an internally or externally generated 1 Hz clock pulse, or in single-shot mode, but is not designed to run at 10 Hz like the NL303. The laser uses the rising and falling edges of a single TTL pulse, which must have a specific width. The rising edge of this pulse determines when the flashlamps should fire, approximately 228 ± 3 μs before desired laser output. The falling edge of this same pulse determines when the laser Q-switches, and laser output occurs ~120 ns later.

The energy in the output pulse is determined by the timing of the Q-switch relative to the flashlamps. The NL303 laser used on COBRA outputs maximum energy in the pulse if it is Q-switched ~228 μs after the flashlamps are triggered. Q-switching the laser later than 228 μs results in a lower energy pulse (the laser

should not be Q-switched before 228 μs or damage may occur). Therefore, the length of the input pulse to the trigger laser determines the energy in the laser pulse, but use on COBRA typically requires it to be switched for maximum output energy.

4.1.5 Visible streak

While not used extensively in the experiments presented here, the visible streak camera is an integral diagnostic in the suite used on COBRA for other experiments. The streak camera requires a single trigger pulse, listed as the rising edge of a 5V pulse in the manual. The amount of time between the trigger and the start of the streak is dependent upon the sweep time. On COBRA, the sweep duration is typically set to 200 ns, for which the manual states the middle of the streak occurs 465 ns after trigger event. Therefore, the streak begins 365 ns after trigger event. Since the PFLs start charging ~300 ns before current reaches the load, these low-jitter monitor signals can not be used to trigger the streak camera. We instead use an earlier signal to initiate the streak, with the unfortunate consequence of introducing more jitter.

4.1.6 PCDs

The Photoconducting Detectors (PCDs) and Silicon Diodes (SiDis or XRDs) do not require a trigger. They have a DC bias across them, and their signal is continuously recorded by the oscilloscopes. Therefore, the only thing required for acquisition of the PCD and SiDi signals is proper synchronization of the oscilloscopes.

4.1.7 4-frame XUV self-emission camera

The 4-frame XUV self-emission camera requires a high-voltage (~40 V in this context), rising edge pulse approximately 50-150 ns before the first frame is acquired, the timing of which is dependent upon the voltage to which the power supply is set. The timing between the individual frames is determined by the physical cable length inside the power supply box, and can not be controlled externally.

4.1.8 Canon Digital Rebel XT cameras

The cameras used for the laser backlighting system are Canon EOS Digital Rebel XTs. These cameras are not designed for scientific work and therefore do not have a short or well documented throughput time from trigger input event to start of image recording. Therefore, we operate them with a 3 second exposure time, trigger them externally to the COBRA trigger-system, and coordinated the firing sequence such that the firing of the machine occurs during this window. The cameras are triggered off of the switch closing the cryo-pump gate-valves, which occurs during each shot. This switch is flipped 1-2 seconds before the machine is fired, within the 3 second camera shutter. Since these cameras have little to do with the rest of the trigger system, they will not be included in any further triggering discussions.

4.1.9 Bolometer

The bolometer requires a high-volt (~40 V) trigger pulse at least 1 μs before the time of desired measurement. The bolometer has a 6 μs wide pulse, and can take data anywhere within this range. However, since our experiments last only 100-

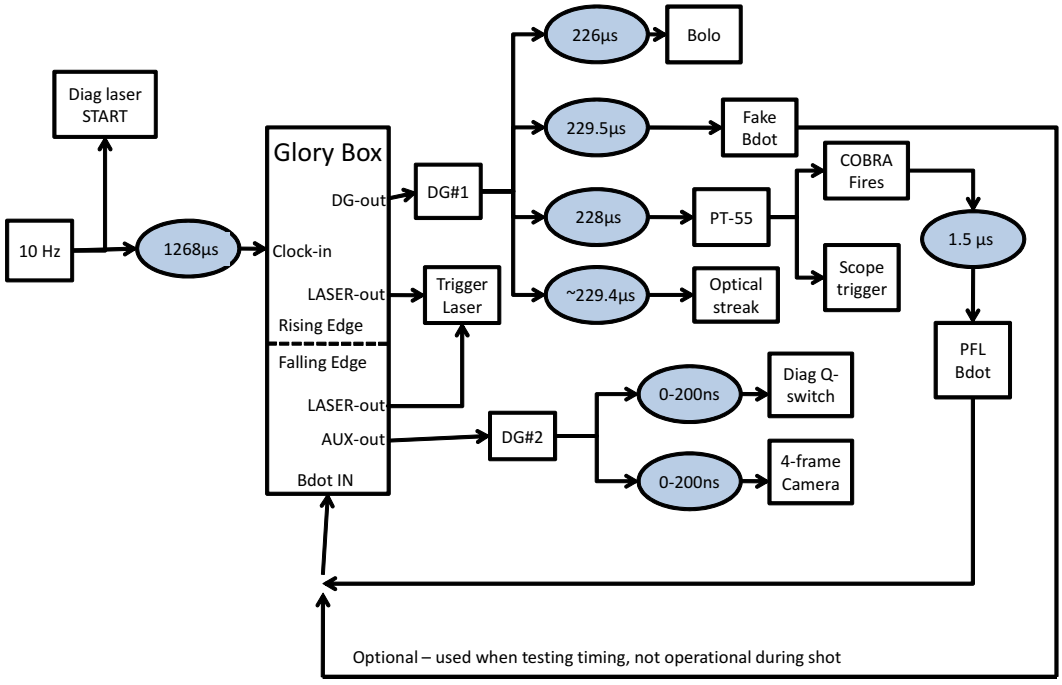

Figure 4.4: Block diagram of COBRA shot timing, including Glory Box and diagnostics.

300 ns, we aim to have the pinch occur somewhere in the middle of this range, so we trigger it ~2 μs before current reaches the load.

4.2 Sequential description of COBRA timing

Please refer to Figures 4.4 and 4.5 for the following description.

A COBRA shot starts with a clock pulse generated from a 10 Hz square pulse generator, which runs continuously. If the diagnostic laser is running on "External 1" mode, it will use this signal with no delay as the "START" pulse. Therefore, the experiment must be conducted such that current reaches the load ~1.5 ms after this pulse to get proper lasing, as described above. This clock signal is

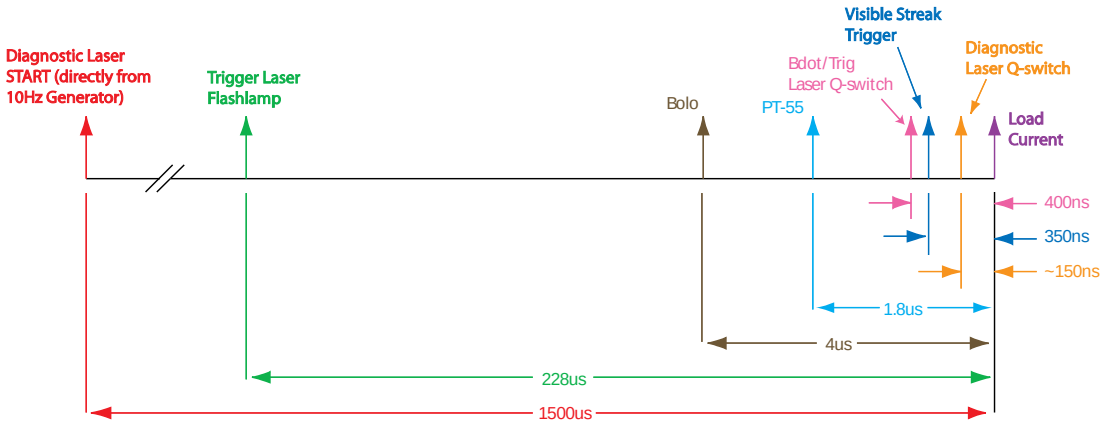

Figure 4.5: Trigger events for required for diagnostic synchronization during a COBRA shot

then delayed 1,268 μs by the analog delay generator located in the screen box currently located on top of the diagnostic laser. This signal is fed directly into the Glory Box, the internal operation of which is described in section 4.3. This preceding sequence of events is happening continuously, but without external user input, the sequence stops here: at the input of the Glory Box. When the main machine trigger button is pressed, the next two clock signals to enter the Glory Box are read, and the Glory Box sounds out the required signals used by COBRA and the diagnostics.

The Glory Box has three outputs, which all have identical pulse shape outputs (despite their different names, which generally refer to the pulse destination). The Glory Box outputs and what they control are as follows:

1. LASER-out: Trigger laser - The trigger laser starts its flashlamps with the rising edge this output, and the falling edge triggers the Q-switch. The falling edge of this pulse will be described in the following sections.

2. DG-out: Delay Generator 1 input (DG1, located in the screen room) - DG1 is triggered off the rising edge of this pulse.

Table 4.2: Delay Generator 1 output channels

Channel	Function	Present delay settings
A	PT-55 trigger	228.000 μs
B	Bolometer trigger	226.600 μs
C	Optical streak trigger	~229.400 μs
D	Fake $\dot{B}$	229.500 μs

3. AUX-out: Delay Generator 2 (DG2, located in the screen box containing the Glory Box) - DG2 is triggered off the falling edge of this pulse.

DG1 and DG2 are Highland Technology P400 digital delay generators, which each have four outputs that are split into separate high voltage (~40 V) and low-voltage (0-10 V) channels.

DG1 is triggered early in the firing sequence (before the PT-55 even), so it is not used for the higher-precision diagnostics due to accumulated jitter. The present delays and functions of the four outputs of DG1 (see Table 4.2) are described below:

1. Channel A (PT-55 trigger): This signal goes to the PT-55 power supply, which initiates the machine firing sequence. The high-volt (40 V) output is used. The scopes are triggered from the PT-55 monitor, so this channel ultimately controls the scopes as well.
2. Channel B (Bolometer trigger): This signal triggers the bolometer well before the machine or any other diagnostics fire. The high-volt (40 V) output is used.
3. Channel C (Visible streak trigger): This signal triggers the visible streak

camera, and is timed such that the streak will begin capturing at the desired time. The value listed above, 229.400 μs, is a good value with which to start for a properly timed short current pulse. Please see section 4.1.5 for a description of the visible streak internal timing.

4. Channel D (Fake $\dot{B}$): This channel simulates a $\dot{B}$ by producing a short, fast pulse similar to the ones from the PFL current monitors. If routed into one of the $\dot{B}$ inputs on the glory box, it will cause the Glory Box to behave as if a shot were being conducted (i.e. dropping the output signals at ~228 μs). This can be used to diagnose the various lasers or 4-frame camera timing issues. For example, when the diagnostic laser does not fire, it can be tested by setting it up for a shot, and hooking up the fake $\dot{B}$. One can then press the main machine trigger button, and a spotter can check to see if the laser fires.

We now follow the trigger pulse sent to the PT-55 to understand the rest of the timing. The triggering of the PT-55 initiates the main COBRA firing sequence. If we exclude laser triggering, current will reach the load based on the predetermined self-break voltages of the various switches. However, there is an inherent total jitter of about 100 ns in this process. Therefore, the diagnostics must be triggered as late in the COBRA firing sequence as possible to maximize their chances of being timed properly. The diagnostics with a short enough throughput delay (e.g. the diagnostic laser, 4-frame camera, etc.) are triggered off the $\dot{B}$s, which indicate the beginning of the charging waveform of the PFLs. This occurs approximately 300 before current reaches the load, and typically results in ~20 ns jitter. The Glory Box accomplishes this precise timing by reading one of these charging waveforms, and, through internal circuitry and with some throughput delay, dropping its output voltage from 5 V to 0 V. DG2 is triggered

off this falling pulse.

The use of the four outputs of DG2 typically depend upon which set of experiments are being conducted on COBRA, but channel A is usually used for the 4-frame camera and channel B is usually used to trigger the diagnostic laser.

4.3 Glory box overview

To accomplish the complicated task of triggering all the diagnostics in conjunction with the machine, we designed and built a custom circuit. This circuit rests in what is called the "Glory Box," and will be referred to as the "Glory Circuit." This circuit works in conjunction with the COBRA, diagnostics and PFLs to coordinate 5 V logic signals that can be used for precise triggering.

The Glory Circuit is a high-speed, single-shot, variable length pulse generator. It has five inputs and 3 outputs

The inputs are:

1. 5V in: 5 V DC power supply.
2. CLOCK-in: Clock pulse, positive, 10 Hz. Any duty-cycle clock pulse can be used.
3. TRIG-in: Input for single-event trigger from control panel. This selects when the Glory Circuit will output.
4. BDOT1: Reads in a signal from a PFL $\dot{B}$ monitor. This input is configured to work off a signal that goes NEGATIVE first.
5. BDOT2: Reads in a signal from a PFL $\dot{B}$ monitor. This input is configured to work off a signal that goes POSITIVE first. This input must also be shorted if not in use.

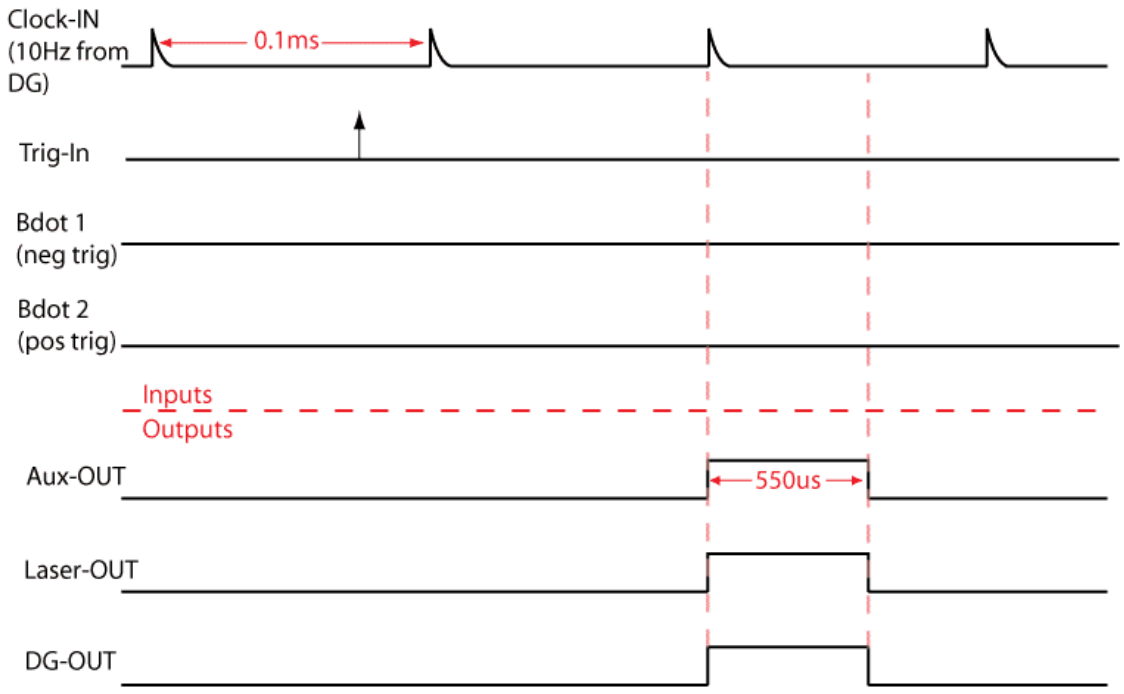

Figure 4.6: Glory Box inputs and outputs without $\dot{B}$ input (no shot).

The outputs are all identical, and their use is described in detail in section 4.2. The output stages are all fairly high-current integrated circuit devices by design, but have been found to have trouble driving long, low-impedance (50 Ω) cables and circuits.

The Glory Circuit reads the rising edge of a clock pulse. If there is no external trigger event (input to TRIG-in), this clock input is essentially ignored, and no output occurs. However, if a trigger on TRIG-in is given by the machine operator, the next clock pulse will also be ignored, but the second clock pulse rising edge will be converted, after a short (~20 ns) throughput delay, to the rising edge of a pulse at the output stages. The width of these output pulses is variable, and depends upon whether or not there is a $\dot{B}$ event (see Figures 4.6 and 4.7). If a $\dot{B}$ is read on either of the inputs (they are logically OR'd inside the circuit), the Glory Circuit will subsequently drop the output voltage from 5 V

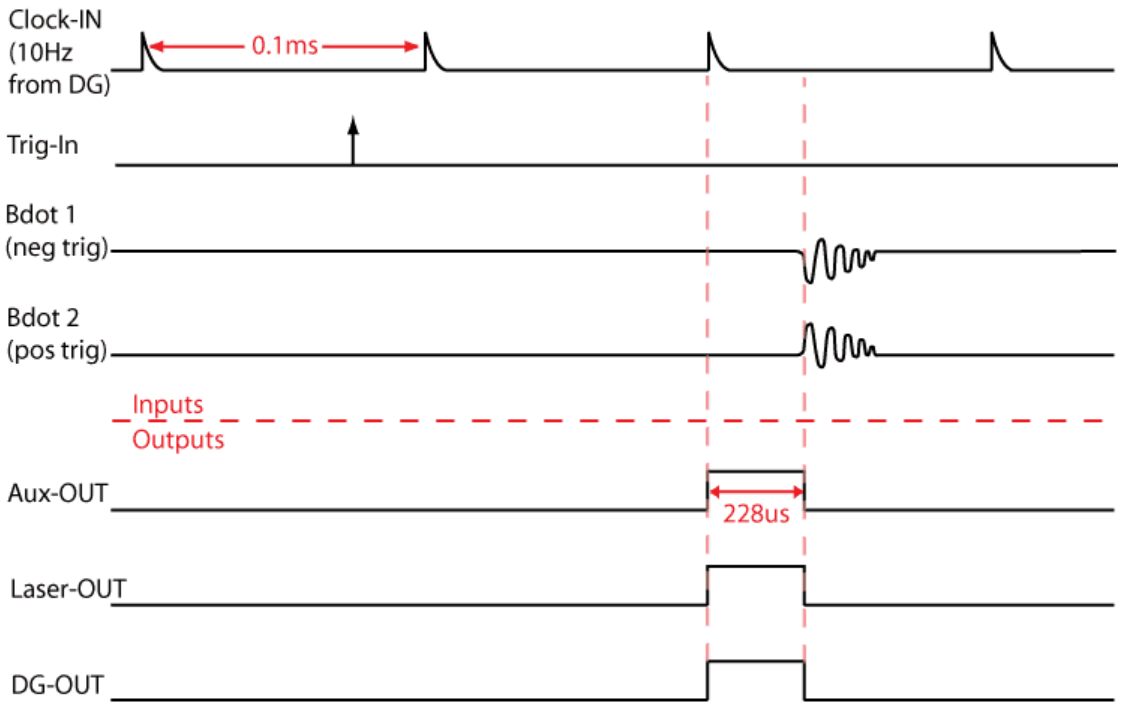

Figure 4.7: Glory Box inputs and outputs with $\dot{B}$ input (during a shot).

to 0 V after a ~20 ns throughput delay. This event typically occurs ~228 μs after the rising edge when COBRA fires. However, if no $\dot{B}$ event occurs, the outputs will automatically fall at an internally set ~550 μs to reset the circuit.

A walkthrough of the Glory Box operation at the circuit level is given in Appendix B.

CHAPTER 5

COBRA EXPERIMENTAL SETUP

Experiments conducted recently on the COBRA pulsed power generator built upon the LCP3 results by modifying the current risetime, contact and polarity of wire array z-pinches. The data were collected in two main experimental runs, the first of which included modifying only contact and risetime to complete the dataset. After we completed this dataset and published the results [66], we conducted the final combined polarity, contact, and risetime experiments. This incremental approach was done to provide a proof of principle test on contact and risetime without the complication of the polarity-reversing convolute. Use of the convolute introduced a lot of questions about current losses and increasing of inductance, so tests on it were conducted simultaneously with the initial contact/risetime dataset to ensure its reliability and compatibility with COBRA.

As described in more detail below, risetime was varied on these experiments by controlling the COBRA current pulse through independent spark-gap output switches. Contact was modified by soldering the wires to the electrodes before loading them into the machine, or leaving them unsoldered. The polarity was modified via a bolt-on convolute, which was rotated to switch the electric field at the wires by re-routing the current through the load without any change in inductance.

5.1 Modifying risetime of a wire array z-pinch: COBRA variable current pulses

COBRA was designed as a 1 MA, 100-250 ns variable risetime machine (Figure 5.1). Four, parallel, 1.8Ω pulse forming lines (PFLs) and output switches

allowed independent switching of power to the load [13]. The 100 ns pulse, referred to as the short pulse in these experiments, was produced by simultaneously firing the four output switches. A 20 ns, monotonically rising pulse can be produced by proper independent firing of the output switches, but has not been reliably implemented on COBRA yet. Therefore, the long pulse used in these experiments was produced by firing the main switches (and consequently the corresponding set of north or south, downstream, output switches) with a separation of ~100 ns relative to one another. This resulted in a 200 ns, "double-humped" current pulse. Note the period of brief positive di/dt ~100 ns into the pulse (Figure 5.1). This was a result of the ~100 ns delay imposed between the two main switches and subsequent two sets of output switches: the first pair of output switches delivered current to the load for ~100 ns, after which the current started to ring back and the center-plane of the adder saw a brief period of positive di/dt. At this point, the positive di/dt acted to increase the voltage across the two remaining (delayed) output switches. This increase in voltage enhanced the self-break condition, and the spark-gaps broke down and closed soon afterward. This sequence of events created very repeatable, albeit double-humped, long pulses, and was found to be (refreshingly) insensitive to jitter at the main switches.

For early times, during the initiation phase of wire arrays and before the load impedance drops, COBRA is essentially a voltage source (see section 2.3). Therefore, the early-time di/dt was nearly the same for the 100 ns and the 200 ns current pulses. The currents of the short and long pulses began to diverge around 35 ns after current onset (Figure 5.2). A consequence of this early-time similarity is that, despite di/dt being a variable of these experiments as a whole, it was not actually a variable during initiation. Therefore, the current-rate effect,

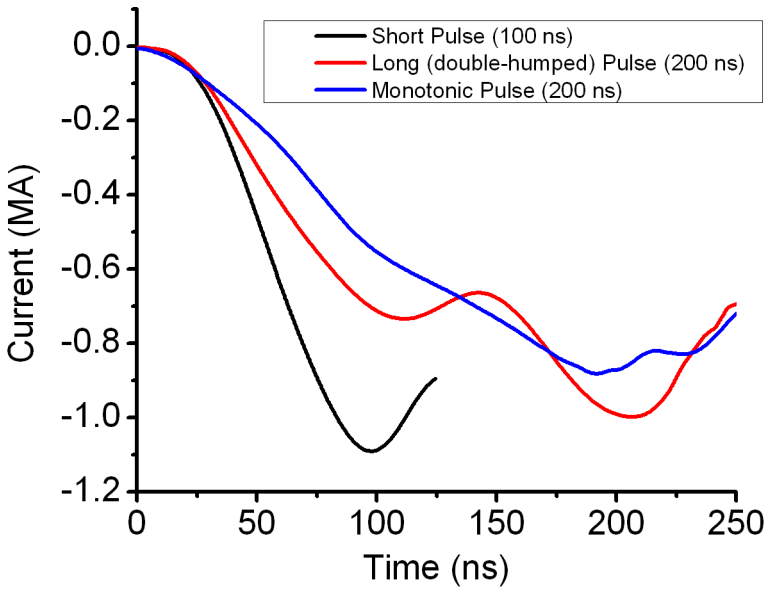

Figure 5.1: COBRA current pulses. The short and long (double-humped) pulses were used for the experiments presented herein. The monotonic pulse can only be achieved with proper laser triggering of the output switches.

which is a commonly studied initiation feature [31, 26, 25],was not studied during these experiments.

Voltage collapse for the arrays studied occurred at approximately 13 ns, at which time the di/dt per wire in both short and long current pulses was approximately 175 A/ns/wire. This can be compared to the single wire results from LCP3 where the largest di/dt was 60 A/ns and resulted in the shortest time to voltage collapse of approximately 20 ns.

5.2 Modifying wire-electrode contact of a wire array z-pinch: soldering the wires to the electrodes

Previous data have shown that the cathode is the most important electrode to solder [25, 43]. Additionally, the geometry of COBRA, specifically the vacuum-

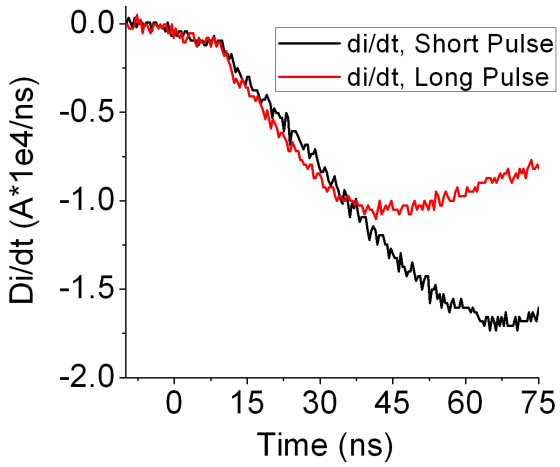

Figure 5.2: Early time di/dt on COBRA. Note that the di/dt for both short and long pulses is nearly identical up to 35 ns.

induced motion in the current-adder stack, made it difficult to solder both ends of the wires in an array. Therefore, all experiments presented here had only the cathode soldered. Note: the cathode in our negative polarity arrays was on the bottom of the array, whereas the cathode for the positive polarity arrays was on the top.

Identical hardware was used for soldered and non-soldered arrays of a specific current risetime. Two different diameter arrays were used in these experiments, as described in section 5.4. The large diameter arrays used in the long pulse shots had wire locating holes drilled in the electrode inserts at a diameter which placed the wires on a 16 mm diameter, and a 12.7 mm hole was drilled in the center (Figure 5.3c). The smaller diameter arrays used in the short pulse shots had radial slots that were machined inward from these holes, placing the wires on an 8 mm diameter, and a 6.4 mm hole was drilled in the center. This short pulse insert is shown in Figure 5.3, and is referred to as the "lollipop" hardware. For the soldered arrays the same hardware was used with the holes, or holes and slots, filled with solder (Figure 5.3b).

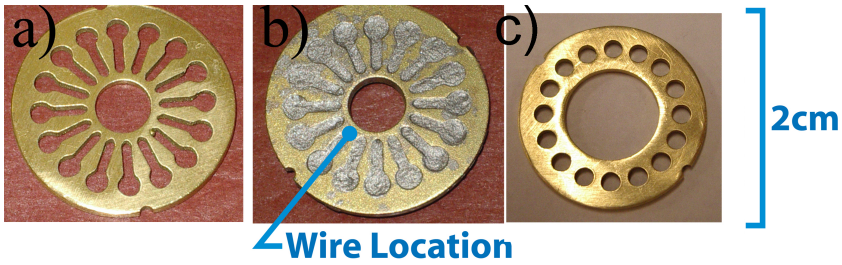

Figure 5.3: Brass "lollipop" electrode inserts. These inserts are replaced each shot to ensure consistency of conditions. a) Top view of brass cathode "lollipop" insert shown before soldering. The wires drop into the holes and are pulled in to the ends of the slots, resulting in an array diameter of 8mm. b) soldered electrode, and c) long pulse electrode. Note solder surface is roughly even with electrode surface.

All hardware was prepared the same way: the wires were strung through 1.5 mm thick brass anode and cathode inserts (Figure 5.3), and were pulled radially inward against the electrodes by hardware external to the anode-cathode gap. These inserts were replaced each shot to ensure consistency of results. Soldered array hardware was tinned prior to wire installation and ultrasonically cleaned to remove any flux residue. The wires were then strung in the array. Non-soldered arrays were mounted in the machine without any further modifications. Soldered array cathodes were heated on a hot-plate to approximately 5˚C above 180˚C, the melting point of the solder used. Temperature had to be carefully controlled, otherwise the flux baked-on and became difficult to remove. Flux usage was kept to a minimum. Many flux types were tested to find the one that performed the best, but was also easy to remove and left little residue. The best combination was found to be solid-core Pb60Sn40 solder dipped lightly in Kester "Tacky-Flux." More aggressive, acid-based fluxes and no-clean fluxes were found to etch the aluminum wire aggressively causing it to break. Therefore, we were limited to paste-type fluxes. Tinning of the

electrodes before stringing helped to minimize the amount of flux used, but a small amount of flux was still necessary to flow the solder and smooth the exposed solder surfaces. This solder/flux combination was applied to the holes or slots surrounding each wire. For positive polarity shots, the top electrode was soldered. The wires were pulled outward against this top electrode, and there were no holes to fill, so solder was applied as a drop around the wires. For the negative polarity shots, the bottom electrode was soldered. Enough solder was applied to completely fill the holes so that the solder on the bottom and top of the inserts was flush with the brass insert surfaces (Figure 5.3b).

The arrays were allowed to cool, and Miller-Stephenson Heavy Duty Flux Cleaner was sprayed on the soldered areas and the wires to remove the trace flux residue. The arrays were then loaded into the machine. The flux, flux cleaner and the heating process used on soldered arrays were tested on non-soldered arrays to ensure they caused no unintended effects.

It should be pointed out that solder did chemically bond to the brass electrodes, but not to the aluminum wires. However, instead of being almost completely surrounded by vacuum in which arcs and plasma can form, contact was improved because the wires below the top surface of the cathode insert were surrounded by a solid, conductive medium.

5.3 Modifying polarity of a wire array z-pinch: bolt-on convolute

Most Marx-driven pulsed power machines charge and connect the capacitors such that, upon firing, the Marx output is negative with respect to ground (described in section 2.1). Using standard notation, current flows from ground,

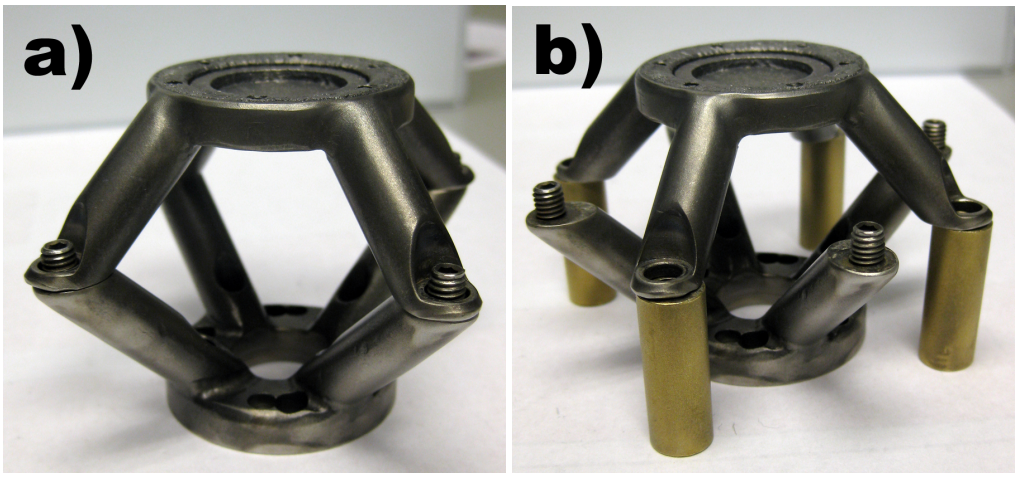

Figure 5.4: COBRA bolt-on convolute in (a) negative polarity and (b) positive polarity..

through the current return posts, through the array, then ultimately back through the switching network to the capacitors. The electric fields established during this process point from the current return posts to the load, and the array is therefore at negative polarity with respect to ground. Without the ability to discharge the Marx positive, the only other way to establish a positive polarity at the load is to re-route the current such that it flows first through the array, then through the return posts and back to the Marxes. Therefore, the inductive voltage drop across the load establishes electric field lines that point from the load to the current return posts. This is accomplished on COBRA using a two-piece bolt-on convolute (Figure 5.4), the top part of which can be rotated and connected differently to accomplish this current re-routing (Figure 5.5).

There were two main difficulties in designing and constructing the convolute: considerations of inductance and electron-emission/current loss. First, the convolute could not add too much inductance. Inductance will limit the current that can reach the load, and a too-high inductance puts greater stresses on the machine upstream of the load in the form of reflected voltages. Second, the in-

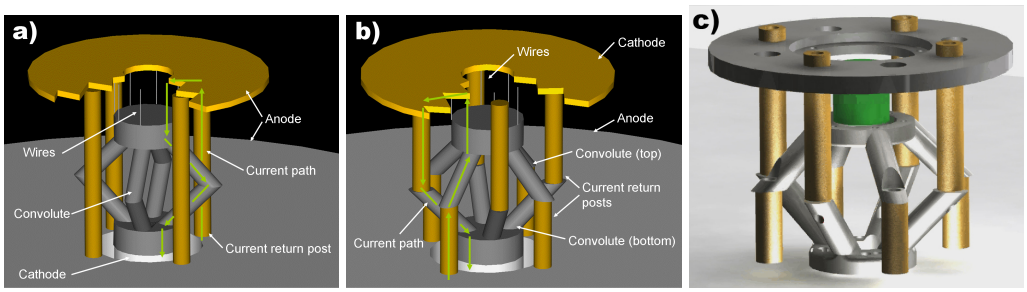

Figure 5.5: Convolute establishing (a) negative polarity, (b) positive polarity. (c) CAD rendering of the convolute in positive polarity showing current return posts.

ductance in the negative and positive polarity configurations had to be nearly identical, otherwise the negative and positive polarity conditions would not be side-by-side comparisons. The inductance of the convolute was experimentally determined to be ~12 ±1 nH in both polarities, low enough to have minimal effects on the load. Therefore, the rigid-mount inductance downstream of our voltage monitor, not including the array, is ~21.5 nH (9.5 nH for the vacuum feed and 12 nH for the convolute). Figure 5.6, which shows a comparison of four shots with and four shots without the convolute, indicates that the inductance added by the convolute does not significantly affect the current reaching the load.

Another problem with the convolute design was that we had to mitigate and carefully monitor any magnetic-field nulls, as well as high-voltage, small separation gaps, to ensure minimal electron loss. Any polarity-reversal situation necessarily produces magnetic-field nulls between the crossing current paths. The magnetic null in the COBRA convolute occurs in positive polarity on the z-axis of the convolute between the negative polarity, bottom piece, and the positive polarity, top piece (a simplified model is developed below). Field nulls can be a problem on pulsed power machines, where breakdown and electron loss is

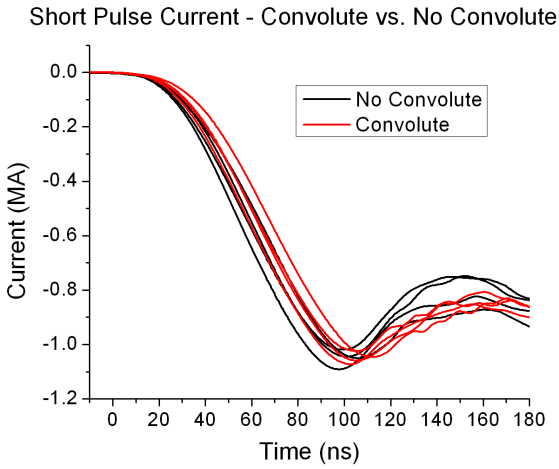

Figure 5.6: Four shot comparison of current with and without convolute. Differences between convolute and non-convolute shots are within typical experimental variations. All signals are shifted, so timing comparisons cannot be made from this plot.

often protected by utilizing magnetically insulation transmission lines (MITLs) [67, 68, 69]. A MITL, as applied to COBRA, consists of a cylindrical conductor with a current flowing along it, and a tangential magnetic field which restricts the radial flow of emitted electrons so that they cannot fully escape from the conductor. If the electric field on the surface of the conductor is high enough, electrons will explosively emit from the surface, and can cause significant current loss. However, in a MITL, a magnetic field (often self-generated) with a large enough component oriented tangentially to the cross section of the conductor, will create a JxB force-induced cyclotron motion with a radius smaller than the gap between the conductors such that the electrons will strike and return to the emitting conductor during their rotation instead of escaping completely. In effect, this creates a sheath of electron-flow around the conductor. MITLs are critical to pulsed power machines the size of COBRA because significant current would otherwise be lost before reaching the load. A magnetic field null around a conductor dependent upon magnetic insulation represents

a high-loss path for electrons. Therefore, the magnetic field nulls in the vicinity of the convolute had to be carefully monitored to ensure that too much current was not being lost before reaching the load.

5.3.1 Field nulls on the COBRA convolute

A simplified visualization of the magnetic field null in the COBRA convolute can be developed by assuming the eight legs of the convolute are infinitely small line-conductors each carrying the same current (Figure 5.7). Four of the line-conductors carry current in one direction, while the other set of four carry the current in the opposite direction, and they are connected at one end with a finite-inductance load. Each set of four conductors lies on the same diameter, and the diameters for the two sets are different but coaxial. Any pair of two, diametrically opposed conductors carrying the same amplitude current in the same direction will cancel each other's magnetic fields at a point equidistant between them, which we will call the null axis. Any number of these conductor pairs can be combined, and, as the diameters on which they are placed are co-axial, a magnetic null will remain on that axis. Therefore, both sets of four conductors will have a magnetic field null at their axes, and when combined, there will be zero contribution from each set of conductors to the magnetic field at the central axis.

On COBRA with the convolute installed but without any polarity reversal this magnetic field null was generally not a problem because the voltage across this null was only the inductive drop along the length of the line-conductors (the voltage drop from the 12 nH imposed by the convolute). However, if the legs were convolved and the polarity was reversed, the magnetic null existed between the inductive voltage drop across both the line-conductors and the

load, which was significantly higher. This presented a high-voltage electron loss path, and would have been evidenced by high-energy electrons, which were accelerated by the voltage along this null, striking the bottom surface of the top convolute piece and emitting high-energy x-rays.

Another high-risk area for electron loss and breakdown was in positive polarity between the four sets of two oppositely charged legs, which are ~2 cm apart with the full load voltage and approximately half the convolute voltage between them. However, the oppositely directed currents created magnetic fields that added constructively between the conductors. Therefore, this part of the geometry had high magnetic insulation, and inspection during experiments (detailed in the next section) showed no emission from this region, indicating proper magnetic-insulation.

5.3.2 Tests on current losses in the convolute

A set of tests were conducted on COBRA with the convolute installed in both negative and positive polarity, and with long and short pulses, to determine current loss (Figure 5.8). These tests used the following diagnostics:

- Current monitors before and at the load, measuring any differential between the main current feed and the current reaching the load. The current before the load was measured with the main COBRA Rogowski coil, and the current at the load was measured with a calibrated $\dot{B}$ probe.
- PCDs aimed at likely current loss paths, and filtered to look at higher-energy electrons (the x-ray energy emitted as electrons strike the surface opposite the emitting conductor are on the order of the voltage across the gap, which is greater than >100 keV).

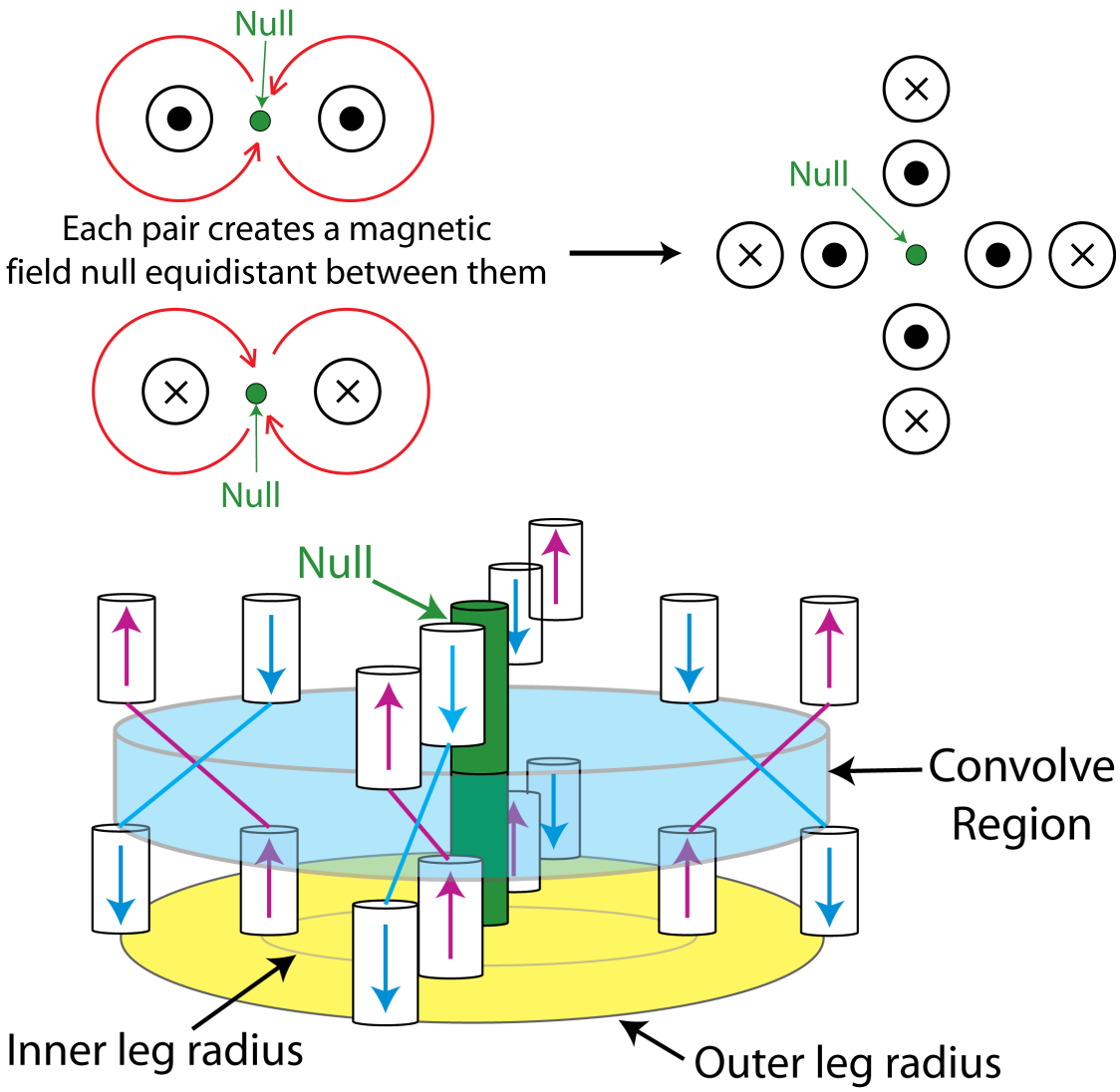

Figure 5.7: Simplified visualization of the magnetic field nulls on the COBRA convolute. (top) 2D, view down axis of conductors, shows magnetic field null formed on line between the two conductors equidistant between them. Combining four pairs of two conductors still produces a null on the axis. (bottom) A 3D illustration of the null in the convolute, assuming no contribution from the legs in the convolve region.

- Time-integrated open-pinhole cameras aimed at the convolute, observing different energies.
- The unfiltered bolometer aimed at the convolute.

In positive polarity, the $\dot{B}$ probes showed some current loss at the time of peak voltage (when di/dt is at a maximum), but it was limited to ~20 kA. The PCDs showed hard x-ray emission coincident with the current loss, most likely in the form of accelerated electrons escaping through the nulls. However, the bolometer did not detect any emitted energy at this point, so the amount of energy emitted from these electrons was probably below the threshold for the bolometer to detect. The open pinhole cameras showed some emission, but no very bright spots (Figure 5.8). The emission seen by the open pinholes was also from very soft x-rays, which are common late-time artifacts of pulsed power feeds, and the time-integrated limitation of the pinhole cameras did not allow us to time-resolve this emission.

The negative polarity configuration showed no current loss with the current monitors, and no x-ray emission with the PCDs and bolometer. The open pinhole cameras again showed some emission, but the emission was again from softer x-rays and was assumed to be late-time.

Taken together, these data indicate that minimal current was lost in positive polarity, and there was no detectable current loss in negative polarity. Therefore, any current losses were below normal experimental variation in current profiles, and we determined that the convolute behaved properly with respect to delivering current to the load.

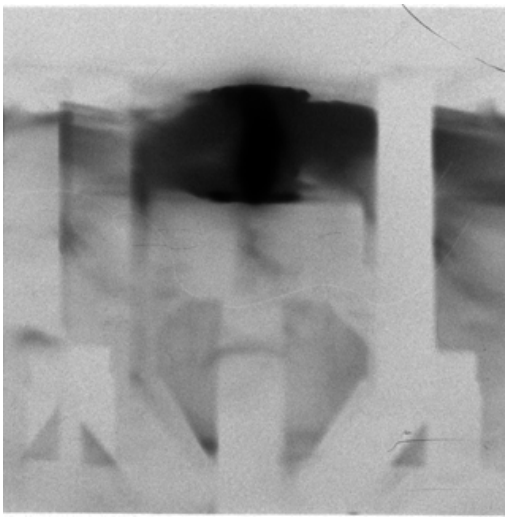

Figure 5.8: Side-on open pinhole negative-image of convolute in positive polarity. The dark spot of emission is from the pinch, and the shadow (in white) of the convolute and current return posts can be seen. The x-rays from the region of the convolute are diffuse and of a low emission level and energy.

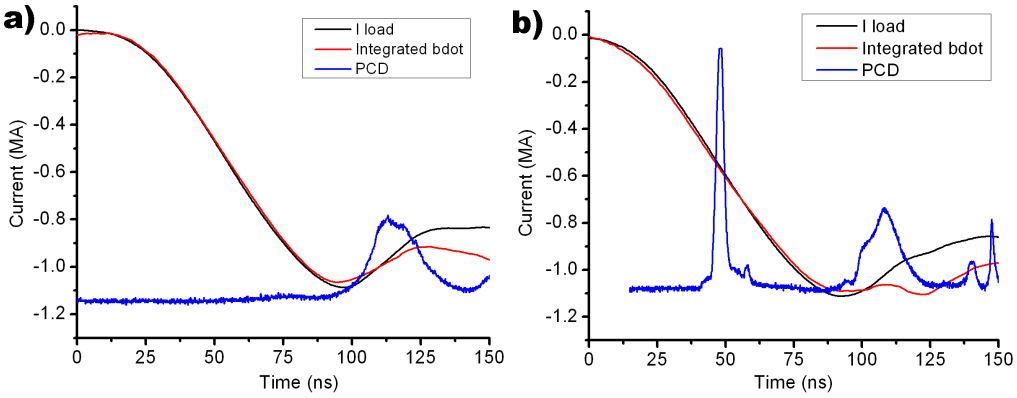

Figure 5.9: Convolute test data, showing (a) negative polarity and (b) positive polarity. The positive polarity shot shows x-ray emission on the PCD signal (2 μm Mylar filtered) at voltage peak (di/dt peak, ~50 ns). However, the $\dot{B}$ measuring current at the load shows very little current lost, as indicated by a slight inflection of its current signal.

5.4 Choosing an array with which to conduct the experiments

All the arrays consisted of 16, 12.5 μm φ aluminum wires, 20 mm long, with four return current posts at 35 mm. The arrays for the short pulses were on an 8 mm diameter. The long pulse arrays were on a 16 mm diameter. The array diameter was varied to match the load to the current drive so that the peak x-ray output occurred at peak current. The choice to change array diameter as opposed to wire diameter was based upon considerations of field emission, which is speculated to have strong effects on the voltage collapse [25, 29, 30]. A simple model, described below, was developed that predicted the electric field at the surface of the wires for different wire and array diameters. This model was used to determine that we should change the wire diameter to match the array to the driver. This choice was made because changing the diameters of the wires from 12.5 to 17 μm, while keeping the array diameters constant, would have drastically changed the field enhancement at the surface of the wires. Changing the array diameter from 8 mm to 16 mm while keeping the wire diameter constant had a small effect of the field enhancement and field emission at the surface of the wires.

The effects on electric field of changing the wire diameter vs. the wire radius can be estimated with a simple model. This involves modeling the wire-return post situation with a simple 2-D electric dipole, where one infinitely long line-charge is at the center of the wire and the other infinitely long line-charge is at the center of a return current post. For simplicity, we assume that the wire and return post are on the same radial spoke of the coaxial geometry. This is not completely accurate for every wire in the array, but can give us an approximation of the ratios of the fields for the different cases. The electric field magnitude at any point on the line between the two conductors can be calculated as:

$$E = \frac{\lambda}{2\pi\varepsilon_0}\left(\frac{d-2r}{dr-r^2}\right)$$

The charge separation, d, is a measure of the array diameter, and is simply the distance from the center of the wire to the center of the return current post (the diameter of which we assume to be infinitely small, an assumption that has a negligible effect on the electric field condition at the wire). This charge separation is different for the two array diameters we used (31 mm and 27 mm for the big and small diameter arrays, respectively). The distance at which we are calculating the field, r, is a measure of the wire radius (~6 μm for the wires used in the experiments, and 8.5 μm for the wires to be used if the array diameter were held constant).

When looking close to the charge that represents a wire (r << d), the results of this model are highly dependent upon r (the wire diameter), and changes in d (array radius) from 31 mm to 27 mm have a negligible effect. Therefore, changes in the diameter of the wire are much more important to the magnitude of the electric field than changes in the array diameter. Table 5.1 summarizes the (dimensionless) results for the ((d-dr)/(dr-r^2)) term, showing little variation when changing the return current radius, but a large difference in the field when changing the wire diameter. This implies that field emission, which is related to electric field amplitude, and in the regimes with which we are dealing, is much more sensitive to wire diameter than the array radius.

We did consider that other parameters important to array dynamics changed with the array radius, namely the interwire gap [70, 45]. However, it was impossible to use identical loads, so compromises had to be made, and our primary concern was keeping field emission as constant as possible.

Table 5.1: Dimensionless results for the electric field at two radii (wire radius) of an infinite 2-D dipole with two different value for the charge separation (return current distance). Note that there is little difference when changing the return current radius (charge separation), but changing the wire radius has a large impact on the electric field.

Electric field (dimensionless)

		Return current radius	
		d=31 mm	d=27 mm
Wire Radius	r=6 μm	169.4593	169.4545
	r=8.5 μm	119.0154	119.0106

5.5 Obtaining statistical significance - five shots per case

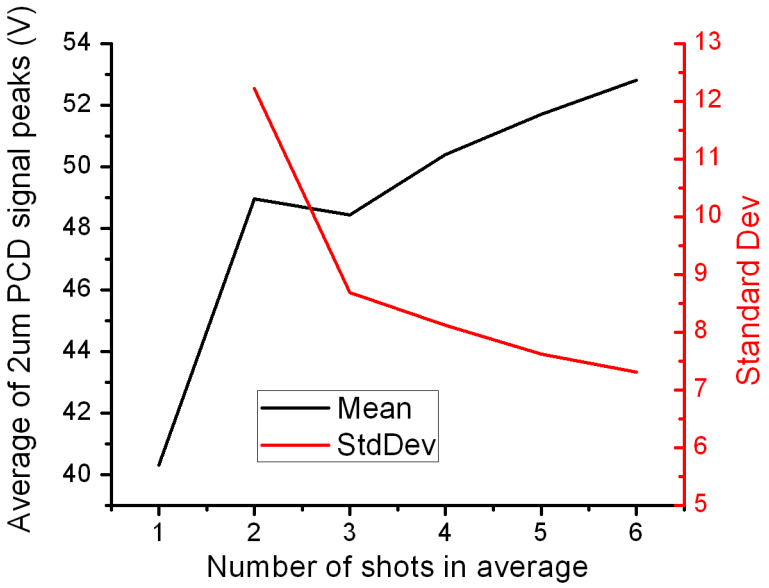

Figure 5.10: Statistical analysis of number of shots The mean and standard deviation both begin to plateau around five shots, and any statistical gains by increasing the number of shots beyond five were considered marginal when compared to the time investment required.

For the experiments presented here, a minimum of five shots were conducted for each case: soldered/non-soldered, short pulse and soldered/non-soldered, long pulse, and each in positive and negative polarity. Five shots was chosen because tests showed that the average for the x-ray peak powers became relatively constant after five shots (Figure 5.10). While improved statistical significance would be realized by increasing the number of shots substantially, obtaining the necessary data would have increased the time required by too much. This is because each successful set of five shots often required from six-eight shots to complete due to undesirable current pulses and diagnostic failures, and this would be multiplied by the number of cases. Therefore, we settled on five shots as a number with enough statistical significance, but did not require an inordinate amount of invested time to obtain.

CHAPTER 6

RESULTS FROM THE CONTACT AND CURRENT RISETIME DATASET

These data are from a series of shots investigating the effects of contact and risetime on wire array z-pinches (polarity was not included) [66]. The contacts were modified by soldering the wires to the electrodes and the current was varied by utilizing different COBRA current pulses, as described in sections 5.1 and 5.2. The numbers of shots conducted in each of the four cases are listed in Table 6.1.

6.1 Results of soldered vs. non-soldered - short pulse

Experiments conducted with the COBRA short pulses were used to carefully examine the four phases of wire array z-pinch dynamics: initiation (resistive voltage phase), ablation, implosion and stagnation. Soldered and non-soldered array results were compared in each phase. The initiation phase, as observed by the voltage monitor, showed no significant differences between soldered and non-soldered array conditions (Figure 6.1a).

As shown in these figures, all resistive voltage signals started at the same time with respect to the current onset, had the same rate-of-rise of the voltage, and reached the same peak voltage before breakdown. This is consistent with

Table 6.1: Number of shots conducted for each case of the contact and risetime dataset

Number of shots for each case		
	Short pulse	Long pulse
Non-solder	7	5
Solder	6	5

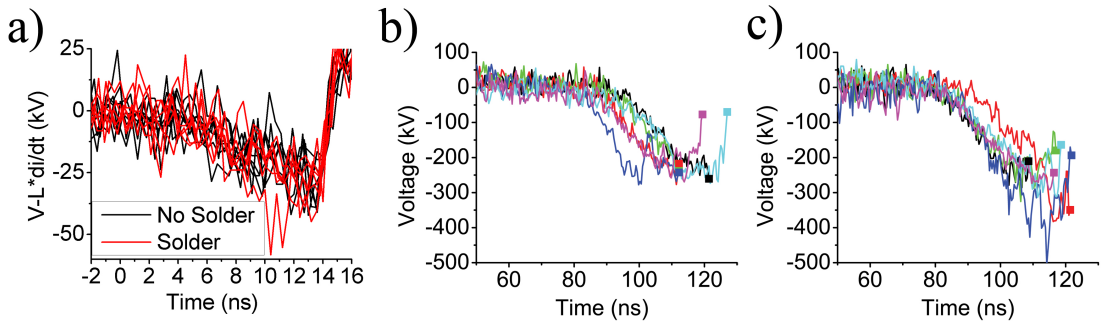

Figure 6.1: Short pulse voltage traces. a) Non-soldered (7 shots) and soldered resistive voltage (6 shots) b) Non-soldered dL/dt voltage c) Soldered dL/dt voltage. Resistive voltages are no different between soldered and non-soldered arrays, but soldered arrays reached a higher average magnitude dL/dt voltage at peak x-ray output, represented by the squares on each trace. This resulted in a smaller current radius achieved.

the single wire experiments which showed no differences in the resistive voltage between soldered and non-soldered wires in negative polarity.

The laser shadowgraphs showed negligible differences between soldered and non-soldered images taken soon after the initiation phase. The improved uniformity of expansion near the electrodes in the single wire experiments demonstrated in the laser shadowgraphs in Reference [25] was observed 300 ns after voltage collapse when the single wires were being driven by 1-5 kA. This wire condition did not exist in the COBRA experiments because of the large di/dt in its power pulse. In the COBRA experiments, 300 ns after voltage collapse, ablation, implosion, and stagnation had already occurred. Near voltage collapse both the single wire experiments and the COBRA experiments were in agreement in that the laser shadowgraphs showed essentially no wire expansion.

In addition, the COBRA laser shadowgraphs showed negligible differences during the subsequent ablation, implosion and stagnation phases. The general

structure and timing of ablation streams and the fundamental wavelength of axial modulation in the images were all determined to be the essentially same for soldered and non-soldered arrays. This was confirmed by the 4-frame self-emission XUV camera.

However, there were observed differences in the voltage monitor and PCD signals for soldered and non-soldered arrays driven by the short current pulses. Under the assumptions described previously, the voltage monitor signals were analyzed to give the current radius as a function of time during the implosion phase (Figures. 6.1b, 6.1c). The dots on these graphs indicate the time of peak x-ray emission as observed on the PCDs. The times and minimum current radii reached at peak x-ray output were tabulated and averaged. Soldered array shots were found to reach a mean current radius of 0.71 mm at x-ray peak. Non-soldered array shots were found to reach a mean current radius of 1.03 mm at x-ray peak. Therefore, after unfolding the dL/dt signal, the soldered array shots reached a smaller current radius on average at peak dL/dt. However, this did not translate to improved x-ray production as the x-ray yields were essentially the same for soldered and non-soldered array conditions.

The PCD data of x-ray output for the short pulse shots showed little difference between soldered and non-soldered arrays (Figures. 6.2a, 6.2b). Signal onsets, rise-times, peak power outputs and total yields were all similar. One anomalous signal occurred with a non-soldered array, resulting in 50% lower x-ray output. This could have been due to especially poor contacts.

The bolometer data showed nearly identical total energies emitted for both soldered and non-soldered array conditions (Figure 6.2c). Even though the soldered arrays appeared to implode to a smaller radius, the x-ray yield was essentially the same as for the non-soldered arrays.

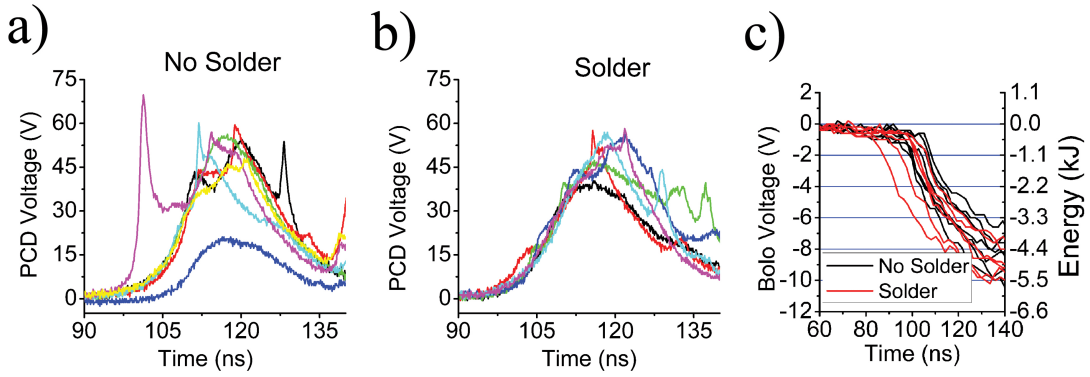

Figure 6.2: PCD with 2 μm Mylar filter for a) non-soldered and b) soldered arrays, and c) bolometer data for short pulse shots. No significant differences were seen between soldered and non-soldered with short pulses

6.2 Results of soldered vs. non-soldered - long pulse

One of the questions posed for this set of experiments was, can the performance of a cheaper, long pulse machine be improved by improving the wire-electrode contacts? Therefore, we conducted long pulse experiments that we could directly compare to the previously described short pulse experiments. Five shots each were conducted with long pulses for both soldered and non-soldered arrays. The arrays were constructed using 16, 12.5 µm φ aluminum wires on a 16 mm diameter. In contrast to short pulse experiments, the long pulse results showed marked differences between soldered and non-soldered arrays.

During the initiation phase, the long pulse results were essentially the same as the short pulse results: no significant differences were observed with soldered vs. non-soldered arrays as indicated by the resistive voltage pulse (Figure 6.3). This is not surprising since, as mentioned, the short and long current pulses are initially identical with the same di/dt per wire of 175 A/ns at voltage collapse.

With long current pulses, differences in the implosion dynamics of soldered

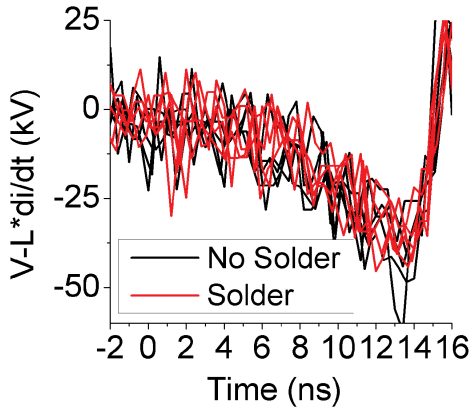

Figure 6.3: Initiation phases for long pulse shots showed no difference between non-soldered and soldered array resistive voltages, and were nearly identical to short pulse initiation phases.

and non-soldered arrays began to appear during the ablation and implosion phases. The XUV images with soldered vs. non-soldered wires demonstrated an enhanced "Christmas Tree" effect as shown in Figure 6.4. This effect had two distinct features that occurred near the cathode: an early pinch or implosion, and axial flow toward the anode. While the images in Figure 6.4 for the non-soldered case were taken later in time than the soldered array images, the soldered array frame at 176 ns clearly shows the effect while the non-soldered array frame at 196 ns shows almost none. We define the time of pinch of these early cathode implosions as the time associated with the first frame of the 4-frame XUV images during which we see a tightly defined column at the cathode with pinch instabilities beginning to form. Previous experiments on MAGPIE at Imperial College have shown fast rising x-ray pulses correlated with the "Christmas Tree" effect [62]. On COBRA we observed no x-ray emission coincident with these early pinches. However, in all but one shot we observed one or more short, fast rising x-ray pulses superimposed on the main x-ray pulse 15-20 ns after the early cathode pinch.

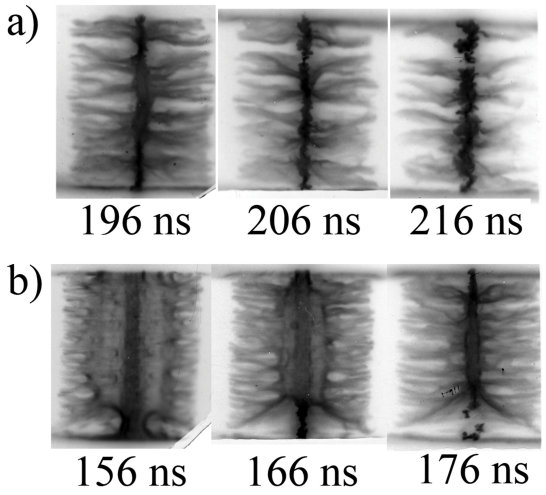

Figure 6.4: Long pulse XUV 4-Frame images show soldered arrays had enhanced "Christmas Tree" effect originating at the cathode a) non-soldered b) soldered.

The x-ray output generated at the end of the implosion phase and during stagnation was different for soldered and non-soldered arrays in these long pulse experiments. This is in contrast to the short pulse results where soldering had almost no effect. PCD signals with a 12 μm Beryllium filter are shown in Figure 6.5. The graph shows all soldered and non-soldered shots with t=0 at peak x-ray generation. Soldered arrays gave higher and more consistent peak powers and total yields. One non-soldered array produced x-rays comparable to the best soldered arrays, but this may have been the result of non-reproducibly good contacts between the wires and the electrodes.

Another difference between the soldered and non-soldered array long pulse x-ray signals is shown in Figure 6.6. Plotted here is dL/dt vs. time as interpreted from the voltage monitor signal by the method previously described. The general shape is a curve that steadily increases in magnitude, reaches a peak dL/dt, then decreases in magnitude. The dots placed on these traces indicate the time of peak x-ray generation for that shot. Using the model developed in section

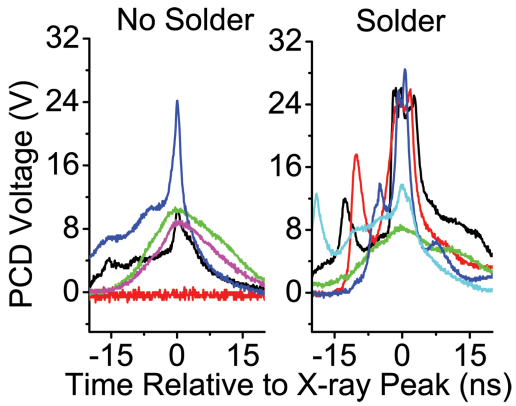

Figure 6.5: 12 μm Beryllium PCD signals for long pulse shots. When compared to non-soldered shots, soldered shots had consistently higher x-ray yields.

3.2.2, the current and voltage monitor signals can be unfolded to give the radius of the cylindrical shell of imploding current. The soldered array shots produced peak x-rays at the same time as peak implosion velocity (Figure 6.6b), but the non-soldered array shots produced peak x-rays 10-15 ns after this peak implosion velocity (Figure 6.6a).

The integrals of dL/dt obtained up to peak implosion velocity for the soldered and non-soldered shots were averaged to obtain mean current radii for both conditions. Both soldered and non-soldered arrays reached approximately the same average current radius of 1.4 mm at peak implosion velocity. Average radii data are not available for later times because the assumption of a thin, imploding shell breaks down and the model is no longer valid. This delayed radiation may be associated with reduced x-ray output from the non-soldered arrays.

Unfiltered nickel bolometer data showed soldering arrays increased total energies output by an average of 69% (Figure 6.7). The total energies emitted by soldered arrays were also more consistent, while the non-soldered energies var-

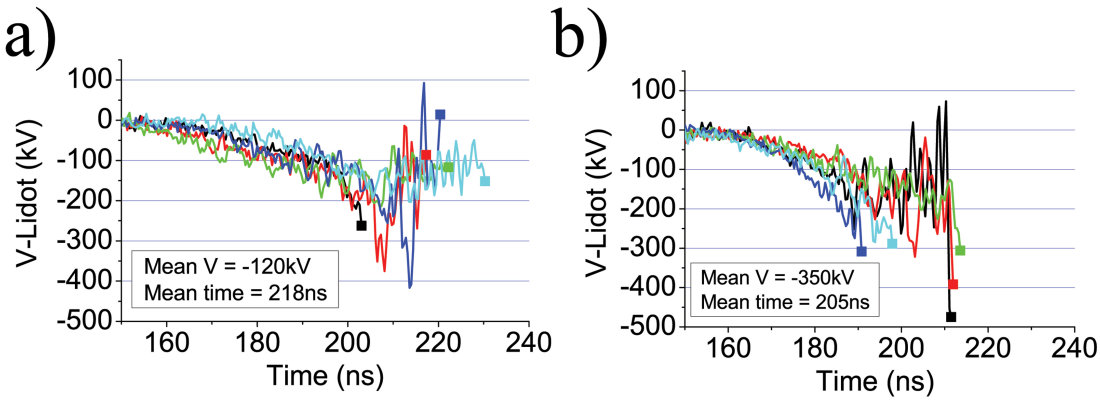

Figure 6.6: dL/dt voltages for a) non-soldered and b) soldered long pulse shots. Square dots represent time of peak x-ray production. Notice soldered shots reached minimum dL/dt voltage at time of peak x-ray production, whereas non-soldered shots produced x-rays 10-15 ns after minimum current radius.

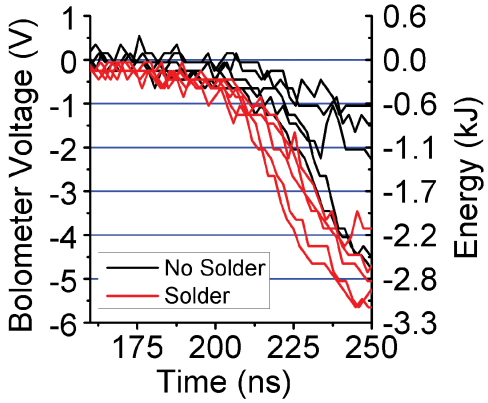

Figure 6.7: Bolometer data for long pulse shots. Soldered shots emitted, on average, 69% more total x-ray energy. Several non-soldered shots emitted comparable total x-ray energies but were less consistent.

ied by a factor of 4. This is consistent with the idea that wires in non-soldered arrays occasionally made good wire-electrode contact, but soldering gave more consistent and reproducible results.

6.3 Discussion and summary of contact/risetime dataset

Previous work has looked at the effects of di/dt [31] and wire electrode contacts [43] on the operation of cylindrical wire array z-pinches. The importance of the early time initiation phase on the subsequent dynamics of the wire array pinch has been proposed [71]. Experiments at Cornell University and elsewhere, using single wires and low current pulses to simulate the initiation phase, have shown that modifying the electrode contacts, switching polarity, and the magnitude of di/dt can influence time of voltage collapse, peak voltage before voltage collapse, the energy deposited in the wires before the collapse, and the rate of expansion near the soldered electrode [25].

The wire array z-pinch experiments reported in this paper have investigated the effects of soldered vs. non-soldered wire-electrode contacts with short (100 ns) vs. long (200 ns) negative polarity current pulses produced by the COBRA generator. Because COBRA is essentially a voltage source for early times, the short and long pulses drove the initiation phase with the same di/dt per wire, 175 A/ns. Only after approximately 35 ns did the short and long COBRA current pulses begin to exhibit significantly different current rise-rates.

6.3.1 Short pulse results

The COBRA short pulse results, even after the initiation phase, showed little difference between soldered and non-soldered arrays. The laser shadowgraphic and 4-frame images showed no observable differences between soldered and non-soldered arrays through the ablation, implosion and stagnation phases of the pinch. Figures 6.1b and 6.1c imply that with soldered arrays the current reached a smaller radius upon implosion. However, the PCD and bolometer

signals in Figures. 6.2a, 6.2b, and 6.2c show that the soldered and non-soldered arrays produced almost identical x-ray yields.

Experiments conducted on the 100 ns Z Machine in negative polarity by Sanford et al. [43] showed a factor of 1.6 increase in radiated power by improving wire-electrode contacts at the cathode. At first glance, the previously described experiments on Sandia's Z-Machine and those using short, 100 ns current pulses on COBRA appear to be in contradiction. There was a marked increase in the x-ray yield with improved contacts on Z but essentially none with improved contacts on COBRA. The individual wires in both of these experiments, during the main power pulses, were driven by very similar currents in both pulse shape and magnitude. However, there was a 100 ns prepulse on Z while COBRA had essentially none. During this prepulse the di/dt per wire on Z was approximately 30-40 A/ns while the di/dt per wire on COBRA quickly rose to 175 A/ns in approximately 13 ns. These early time differences in the pulse shapes on the two machines may be responsible for the increased x-ray peak power and total yield due to improved contacts that were seen on Z but not on COBRA.

6.3.2 Long pulse results

The main differences in the COBRA-driven wire array z-pinches between soldered and non-soldered arrays occurred with long pulses. During the initiation phases, there were no observed differences in the energy deposited between soldered and non-soldered arrays. However, differences later in time were demonstrated by the bolometer signals that responded to total time integrated radiated energies, the PCD x-ray detector signals that gave time dependent radiated energies above ~1 keV, the XUV 4-frame images, and the inductive voltage mon-

itor. The soldered arrays driven with long pulses generated peak x-ray power at maximum dL/dt. The non-soldered shots generated peak x-ray power 10-15 ns after peak dL/dt. The soldered shots emitted, on average, 69% more total radiated energy than the non-soldered shots, and with more consistency. The soldered shots also showed an enhanced "Christmas Tree" effect near the cathode with an early pinch and flow towards the anode.

Thus, the COBRA long pulse results show that soldering improved both x-ray power and total yield, despite no improvement in total energy deposited in the wires during the initiation phase. The first effects of improved contacts were observed in the ablation and implosion phases with the appearance of the "Christmas Tree" effect. This is the first clear evidence that improved contacts can affect the ablation and implosion without a significant difference in energy deposited during initiation. However, single wire experiments did show faster wire expansion near the soldered contacts. It is unknown whether this effect was present in the COBRA experiments and, if present, whether it influenced the occurrence of the "Christmas Tree" effect and the improved x-ray output with soldered contacts.

As mentioned earlier, one of the questions set forth for this work was, can the variable risetime feature of COBRA be used to determine if less expensive, long pulse machines can give comparable x-ray yields to those generated by the more expensive short pulse machines? To this end the long pulse vs. short pulse and soldered vs. non-soldered results are compared in Table 6.2. Shown in this table are the average total energies radiated as observed by the bolometer and a percentage figure of merit with the short pulse results taken as the 100% objective. As can be seen from this dataset, soldering the contacts with long current pulses significantly improved the peak radiated power and total yield

Table 6.2: Average voltage change and total energy emitted by x-ray pulse for contact and risetime dataset

Mean voltage change and total energy emitted by x-ray pulse

Shot series	ΔVoltage [V]	Energy [kJ]	% of short pulse
Long pulse, non-soldered	2.9	1.60	37%
Long pulse, soldered	4.9	2.70	62%
Short pulse, all	7.9	4.35	100%

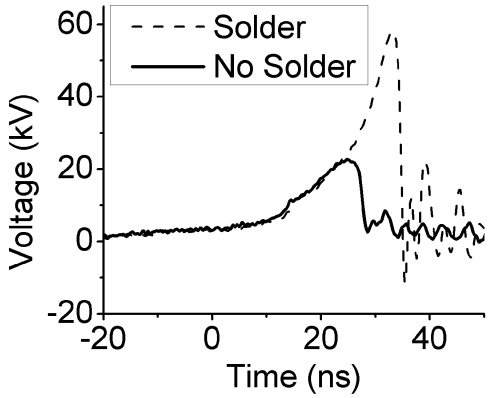

Figure 6.8: Breakdown voltage of positive polarity single wires. Operating in positive polarity dramatically increased resistive heating of wire and therefore energy deposition. Chapter 7 will focus on the impact this effect has on wire array z-pinch implosion.

as compared to the non-soldered results, but only resulted in about 62% of the total yield produced by short current pulses.

All the work in this dataset was performed on COBRA in negative polarity. The previously mentioned low current single wire experiments that were performed to simulate the initiation phase were done in both positive and negative polarity. A positive polarity single wire result is shown in Figure 6.8. It can be seen that in positive polarity with soldered contacts the voltage collapse was delayed and the peak voltage reached before collapse was significantly increased

resulting in increased energy deposited in the wire cores. This has motivated a series of experiments on COBRA using a reversible convolute in the load region to allow positive and negative operation of the array. Soldered and non-soldered arrays were operated in both negative and positive polarity with both short and long pulses.

CHAPTER 7

RESULTS FROM THE POLARITY, CONTACT AND CURRENT RISETIME DATASET

The data presented in this section are from experiments motivated by single wire results, and the contact and risetime dataset presented in the previous section. These experiments examined the effects of polarity, contact and current risetime on wire array z-pinches. Load polarity with respect to ground was varied between positive and negative. Contacts were varied by applying solder or leaving them unsoldered. Current risetime was modified by varying the di/dt supplied by COBRA, leading to two different length current pulses. These methods are all described in chapter 5. A parametric sweep was conducted across the three variables, resulting in eight different cases.

The number of shots conducted in each of the eight cases is shown in Table 7.1. The actual shot numbers used, separated by case, are shown in Table 7.2.

7.1 Effects on the initiation stage

If one wire of a wire array z-pinch did in fact behave like the single wire experiments on LCP3, then we would have expected:

Table 7.1: Shots conducted for each case of the polarity, contact, and risetime dataset

Number of shots for each case				
	Short pulse		Long pulse	
	Positive	Negative	Positive	Negative
Non-solder	5	5	5	7
Solder	5	5	5	5

Table 7.2: COBRA shot numbers used in each set. * indicates PCD signals clipped.

Short Pulse				Long Pulse			
Positive		Negative		Positive		Negative	
Press	Solder	Press	Solder	Press	Solder	Press	Solder
1364	1369	1373	1382	1389	1395	1404	1409
1365	1370	1377	1383	1390	1398	1405*	1410
1366	1371	1379	1384	1392	1400	1406	1411
1367	1372	1380	1385	1393	1402	1407*	1412
1368	1374	1381	1386	1394	1403	1408	1413
						1414	
						1415	

- Operating in positive polarity to increase energy deposited before voltage collapse when compared to negative polarity.
- Soldering the wires to the electrodes to increase the energy deposited before voltage collapse only in positive polarity.

Note that the effect of di/dt on initiation was not considered, as the COBRA long and short current pulses do not have different di/dt's during initiation. Therefore, di/dt was only considered a variable for times after 35 ns, or during the ablation and later phases. However, despite the similar current pulses, the short and long pulse data cannot be combined due to the different arrays used. Therefore, they are treated as separate cases and no comparisons are made between the two.

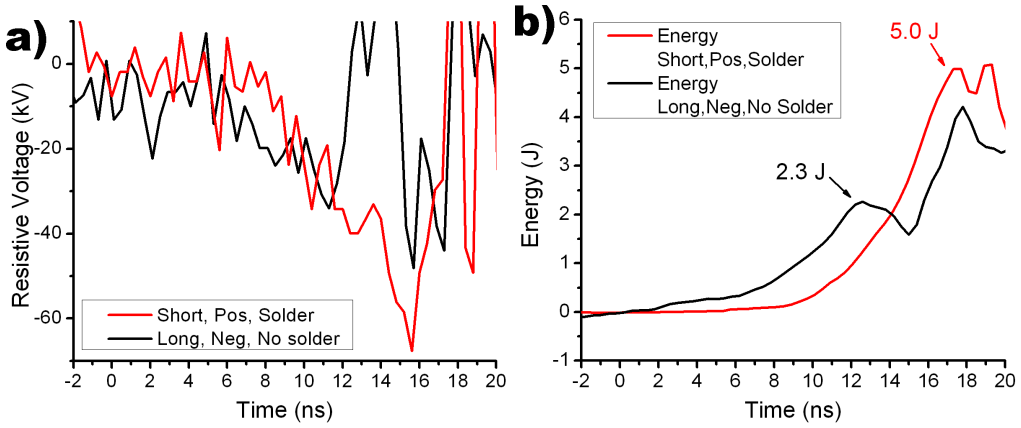

Figure 7.1: Improvement in (a) resistive voltage and (b) energy deposited shown by operating in positive polarity. Note that both polarity pulses are negative here (despite positive polarity at the load) because the voltage monitor reads the voltage drop at the same location in the vacuum feed for both positive and negative polarity, and therefore the polarity of the signal it detects does not change. These are not entirely representative traces, as one of the better positive cases was chosen. For numerical comparisons, please refer to Table 7.4.

We found that both of these expected, low current, single-wire effects were present in wire arrays. Figure 7.2 shows the average deposited energies for all eight cases. All positive shots are in red, negative in black. Solid squares represent soldered shots, hollow squares represent non-soldered shots. Similar to the single wire experiments, operating in positive polarity increased the energy deposited for all cases. Again, similar to the single wire experiments, soldering the wires to the electrodes consistently increased energy deposited only in positive polarity. Two shots are shown in Figure 7.1 as examples of resistive voltage and deposited energy traces.

The percent differences, separated into improvements from positive polarity and improvements from soldered contacts, are summarized in Tables 7.4 and 7.3. Averaging the results, positive polarity had a net impact of improving energy deposited by 25%. Soldering positive polarity arrays improved energy

Table 7.3: Improvement in the energy deposited during initiation from operating in positive polarity (vs. negative) for each case of the polarity, contact and risetime dataset.

Improvement from positive polarity			
		Current risetime	
		Short	Long
Contact	Soldered	26%	34%
	Non-soldered	19%	21%

Table 7.4: Improvement in the energy deposited during initiation from soldering the wire-electrode contacts (vs. non-soldered) for each case of the polarity, contact and risetime dataset.

Improvement from soldering			
		Current risetime	
		Short	Long
Polarity	Positive	22%	14%
	Negative	15%	-3% (decreased)

deposited by 16%, on average.

Numerical comparisons between single wires and wire arrays were not valid because the di/dt's involved were radically different. The highest di/dt seen on LCP3 was 60 A/ns, whereas voltage breakdown occurred on COBRA at around 175 A/ns.

Energy deposited can be compared to the amount of energy required to convert the wires from a solid to liquid or vaporized state, as described in section 3.2.1. The energy required to melt the wires is composed of the energy

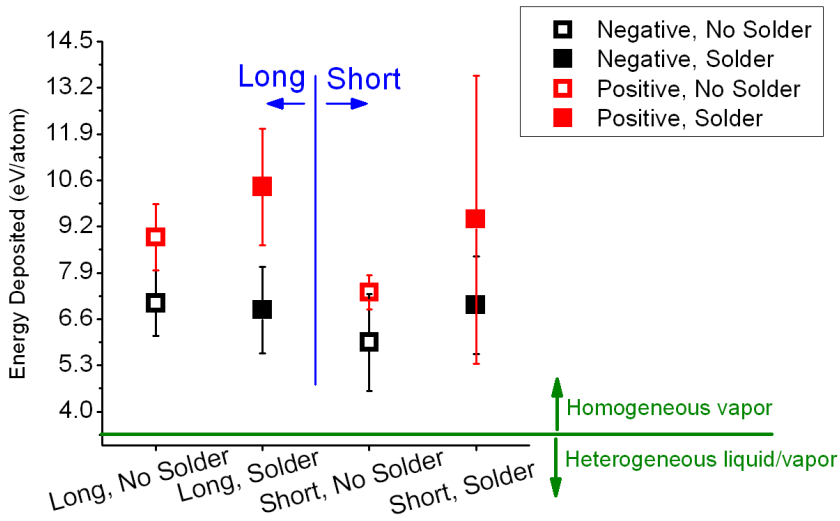

Figure 7.2: Averages of energy deposited for all eight cases. Operating in positive polarity increased the energy deposited in all cases. Soldering also improved the energy deposited in positive polarity in all cases. Soldering had mixed a mixed effect on negative polarity, increasing energy deposited in one case, decreasing it in the other. All deposited energies were above the energy required to completely vaporize the aluminum wires.

required to raise the temperature of the wires from room temperature to the melting point, and the latent heat of fusion of the amount of mass in the array. The energy require to vaporize the wires is composed of the energy to heat the wires from the melting point to the vaporization point, and then the latent heat of vaporization of the amount of mass in the array. These values for our arrays are listed in Table 7.5.

Comparing the energy required to melt/vaporize the array and our results for energy deposited, we observe that we have deposited enough energy to completely vaporize the array. The amount of energy we have deposited per atom is on the order of the amount of energy necessary to ionize the first electron of that atom. Therefore, we are beyond the regime of homogeneous liquid wire cores suspected to be desirable for initiation [30]. Despite this undesirable char-

Table 7.5: Thermodynamical properties of state changes of aluminum arrays used in these experiments.

Thermodynamical property of aluminum/array	Value	Unit
Conversion factor Joules/array to eV/atom	2.6376	N/A
Energy to transition from room temp to melted	0.2711	eV/atom
Energy to transition from room temp to vaporized	3.4402	eV/atom
First ionization potential for aluminum	5.986	eV/atom
First ionization potential for aluminum	5.986	eV/atom

acteristic, we do not have present capabilities to decrease the amount of energy deposited in the array during initiation. However, the theory of homogeneous liquid wires was derived from light emission from single wire experiments and ablation theory - there were limited data on the relationships between initiation conditions and actual x-ray emission. Therefore, we examined a different regime than what the theory predicts to be optimal, but can still study the effects of absolute energy deposited into the wires during initiation.

7.2 Effects on later stages

The two main foci of these experiments were to study the effects of polarity, contact and risetime on the initiation stage, and the subsequent effects on x-ray generation. We also examined the effects of initiation and deposited energy on the later stages, and tied these results in with present literature.

The ablation phase is speculated to depend greatly upon the initial conditions created during the initiation phase. Fast risetime machines, 100 - 200 ns, have the desired ablation rates when the wires are in a homogeneous liquid state after initiation. The experiments presented here all surpassed the hot, liq-

uid wire state, and ablation was started with fully vaporized wire cores.

We relied upon the self-emission XUV 4-frame camera, laser backlighter and current radius derived from the voltage and current monitors to diagnose the ablation phase. Figure 7.3 shows sample 4-frame camera data. In analyzing the 4-frame camera images, we compared structure and timing of general advancement of pinch dynamics, axial symmetry, sizes of streamers, and diameters of pinch columns. Several observations from the 4-frame camera data:

- In long pulse, the "Christmas tree" effect was observed more frequently with soldered shots. This was independent of polarity.
- In long pulse, the two non-soldered shots with "Christmas tree" activity also had the highest x-ray output for all negative polarity shots. These data, and the data from the contact/risetime dataset (where the "Christmas tree" effect was more prominent in shots with higher x-ray output), imply that there is a positive correlation between the appearance of the "Christmas tree" effect and high x-ray output.
- In short pulse, the pinch column in positive polarity shots was observed to be smaller in diameter. This indicates a smaller current radius, hotter pinch. This is consistent with the current radii data presented later.
- The "Christmas tree" effect is not present in the smaller diameter arrays used in the short pulse shots.

Sample optical streak images are shown in Figures. 7.4 and 7.5. One can observe from the radial streak of the long pulse (Figure 7.4, top) the signs of a non-uniform implosion front. This is typical of these aluminum arrays, and the late-time implosion trajectories can cause late-time spikes on the PCD traces, as shown later. Emission can also be seen ~50 ns before the first inward-streaming

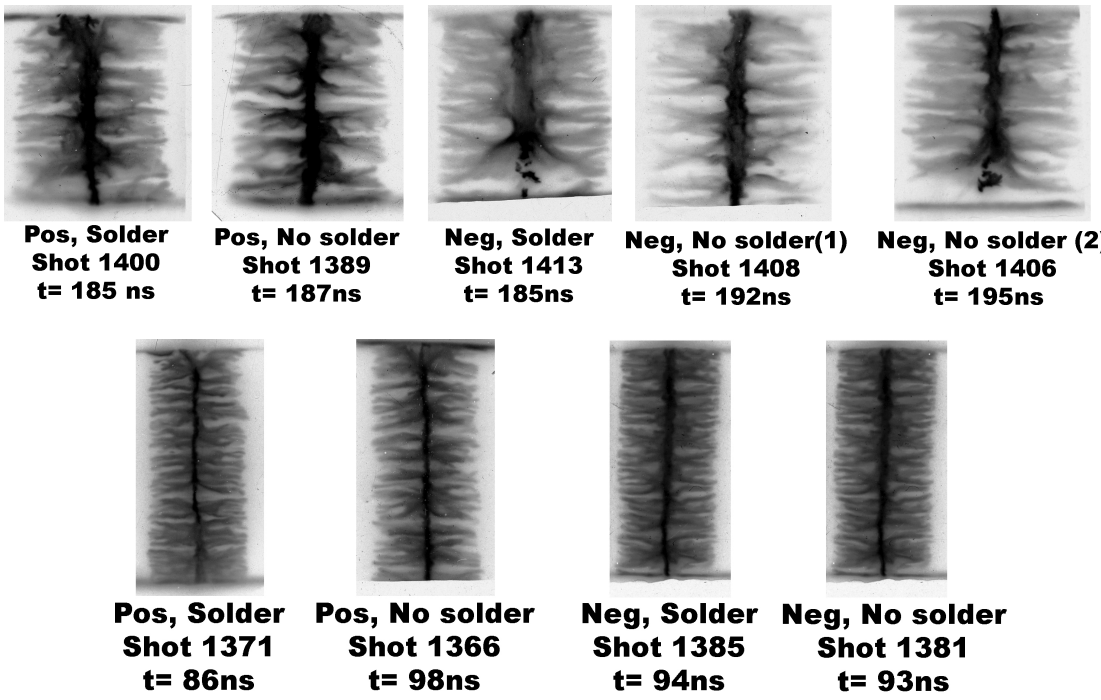

Figure 7.3: 4-frame self-emission XUV images. Representative images from each of the cases in (top) long pulse and (bottom) short pulse. Two shots from the long pulse, negative, no solder case are shown as representation of the inconsistent appearance of the "Christmas tree" effect (early cathode implosion and pinch).

wire (~75 ns before the fiducial). This is also typical of these aluminum arrays, and the time and intensity of this emission, presumed to be from the on-axis precursor, did not vary between cases. The precursor was also seen on laser shadowgraphs, starting at around the same time. The emission from this precursor, however, did not appear on the PCD signals, as shown later.

The non-uniform implosion front is also seen in the axial streak (Figure 7.4, bottom) as bubbles that move past the axial viewing-port at different times. These bubbles impacted the central column at different times, expanding the x-ray emission from the pinch and producing several bursts, instead of a unified, main pinch.

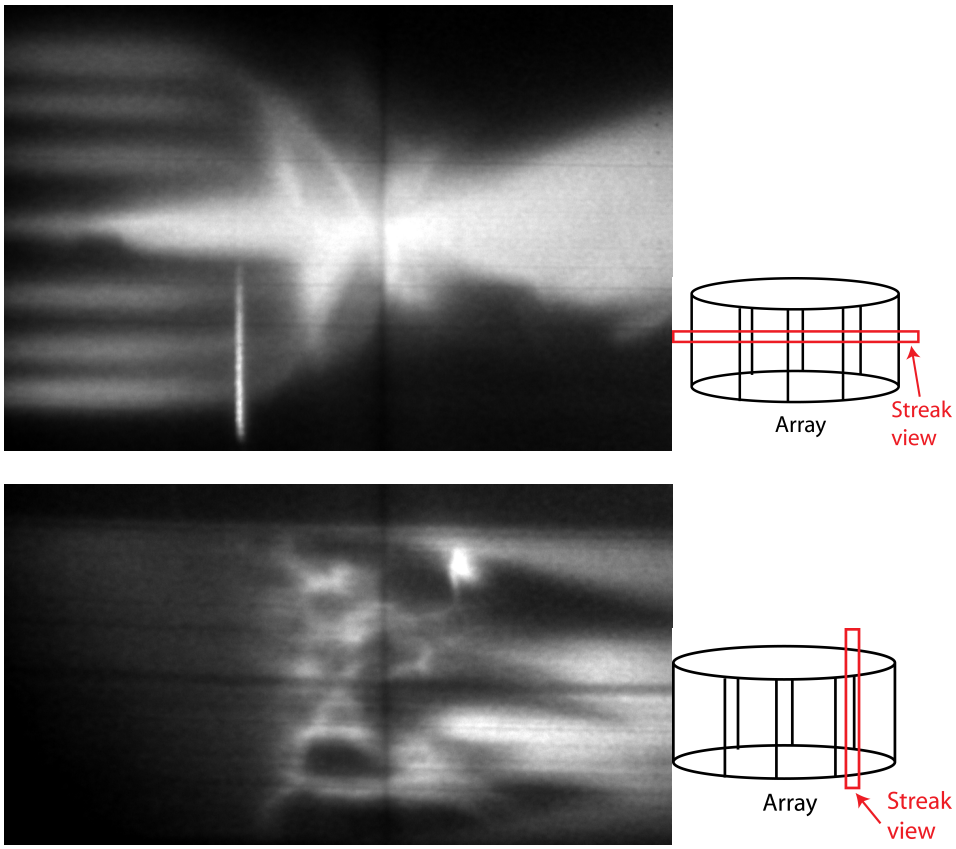

Figure 7.4: Representative optical streak from long pulse, negative, soldered: shot 1410. (top) radial streak and (bottom) axial streak were both collected on the same camera. The horizontal axis on both of these plots represents 200 ns, increasing from left to right. The fiducial (bright vertical line, ~2 ns in length) is at 150 ns into the current pulse.

The short pulse streak shows a lot of background emission (Figure 7.5). This is also typical of the short pulse, smaller arrays.

Other than the general features noted above, the optical streak images showed no consistent differences between any of the eight cases.

Average current radii were unfolded from the current and voltage measurements, as described in section 3.2.2. This analysis was only done for the short pulse shots because the repeatable PCD peaks and voltage monitor measurements allowed accurate determination of implosion milestones (beginning and

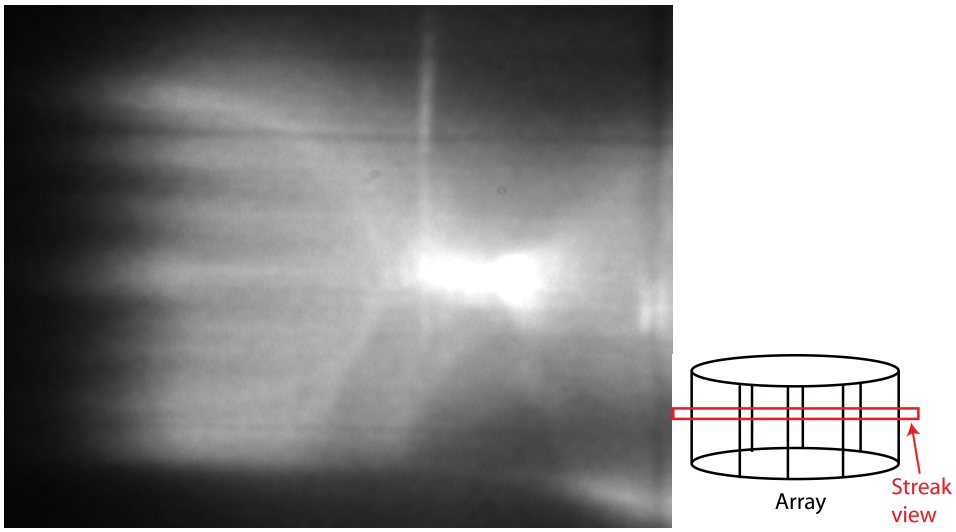

Figure 7.5: Representative optical streak from short pulse, positive, soldered: shot 1370. Only the radial streak is shown, and the horizontal axis represents 100 ns, increasing from left to right. The fiducial (bright vertical line, ~2 ns in length) is at 95 ns into the current pulse.

end of emission, etc.). We had little confidence in the long pulse current radii due to the ambiguities of which times should be selected as minimum current radii, and voltage monitor irregularities contributed to several minimums that were most likely artifacts of late-time breakdowns on the physical monitor. The summary of the short pulse current radii is shown in Figure 7.6. The comparison of short pulse positive vs. negative is also shown in Figure 7.6. Clearly, non-soldered positive shots performed the best with regards to minimum current radius, reaching ~1.1 mm. The negative, soldered shots reached the largest minimum radius, 2.0 mm. Positive soldered and negative soldered performed similarly, with 1.4 and 1.3 mm current radius reached, respectively.

Comparing all positive to all negative shots, however, shows that positive reached 1.2 mm vs 1.7 mm averaged minimum current radius. This represents a ~30% smaller radius. These data are consistent with the 4-frame XUV data

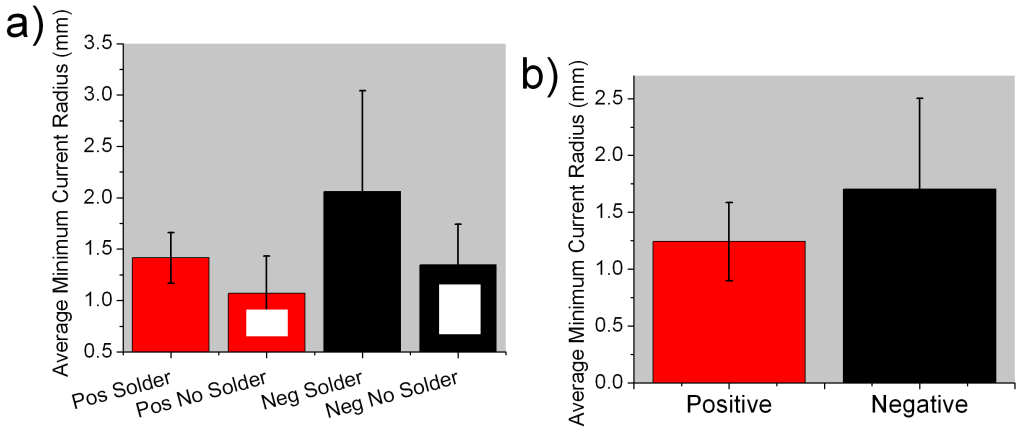

Figure 7.6: Averaged minimum current radii for short pulse shots from the polarity, contact and current risetime dataset for (a) all four cases and (b) separated into positive and negative polarity.

presented earlier, which showed a smaller main pinch column in positive polarity.

PCD data were compiled and analyzed for all eight cases. Up to four PCDs observed the pinch for every shot. The standard set of 2 μm and 6 μm Mylar and 25 μm Beryllium were used. An additional PCD with 6 μm of Mylar observed the pinch through a collimating tube. We used this collimated PCD because we were concerned that emission from the convolute would confound the pinch radiation data. During post-processing, however, we determined that the collimated data were typically not substantially different from the non-collimated data (probably because there was little emission from the convolute during the pinch). For the analysis below, however, we will present only data from this 6 μm filtered, collimated PCD. This is because it is possible that some shots had emission from the convolute during the time of the pinch, and we wanted to eliminate the possibility of analysis errors due to potential convolute emission.

Before we delve into the analysis, it is worthwhile to visit Figure 7.7, which is a comparison of two representative PCD signals from a short and long pulse.

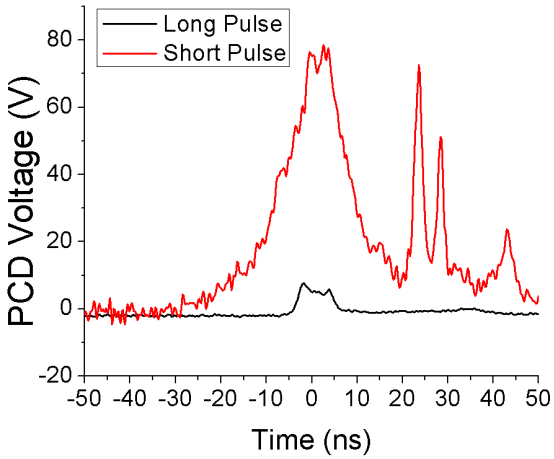

Figure 7.7: Representative long vs. short pulse PCD signals showing order of magnitude improvement to peak power in with short pulses.

It is immediately visible from this plot that we observed substantial differences in both peak power and total yield between short and long pulses. This is a consistent effect; Figure 7.7 shows only two representative cases. Average long pulse peak powers were an order of magnitude below average short pulse peak powers. The x-ray pulse shapes in long pulse were also very broad, highly inconsistent, and rarely formed peaks with a measurable risetime. Due to these differences, we focused on short pulse PCD signals, and ultimately determined that the main conclusion to draw from the long pulse PCD signals was the poor performance of these long pulse arrays relative to short pulse arrays.

Overlaid 6 μm, collimated PCD data from all shots are shown in Figure 7.8 separated by case. These signals have been shifted in time to align the first peaks.

Comparisons of the peak powers of all eight cases, from the 6 μm collimated PCD, are shown in Figure 7.9. The average, total PCD yields are shown, for short pulse only, in Figure 7.10. The long pulse yields were not calculated due to difficulties in determining and repeatable choice of start and finish of the PCD

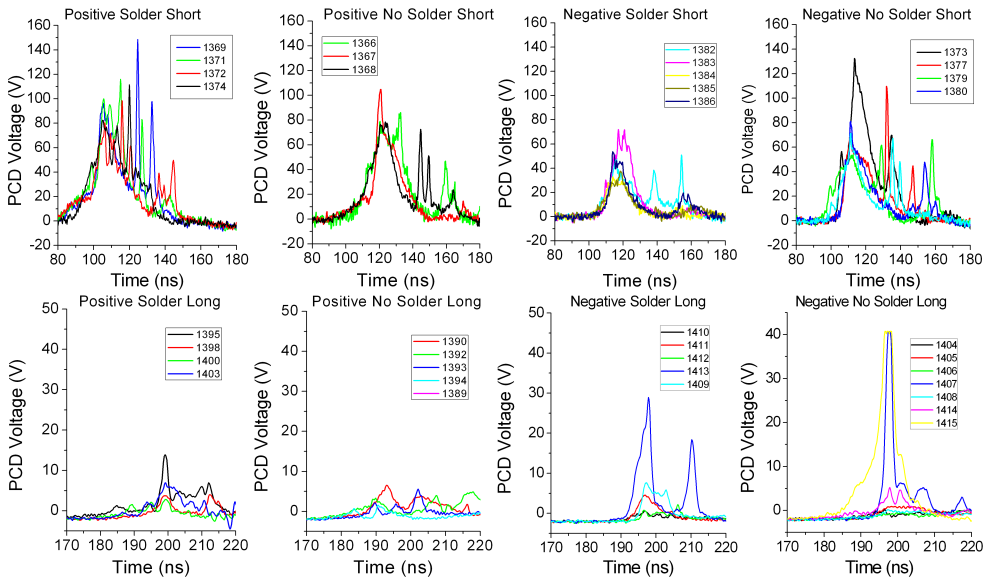

Figure 7.8: All 6 μm Mylar, collimated PCD data separated by case for the polarity, contact and risetime dataset. The signals have all been shifted to align the first peak, so relative timing is irrelevant.

pulses. This led to a lack of confidence in the results.

We also averaged and compared the peak powers and yields of the negative vs. positive shots. These data are shown in Figure 7.11. One can observe that operating in positive polarity with short pulses increased peak power by 20% and total yields by 50% over negative polarity.

Comparing the PCD and current radii data, one can see a positive correlation. Operating in positive polarity shows an increase of 20% in peak x-ray power and a 30% decrease in minimum current radius achieved. These data are summarized in Table 7.6.

Bolometer data were obtained and compared for all shots. The 6 μm Mylar, collimated PCD signal was used to determine the length of time for which the array was radiating, and the energy absorbed by the bolometer was determined by these time constraints. The beginning of rise of this PCD signal was used as the beginning of bolometer energy absorption. The end of radiation was

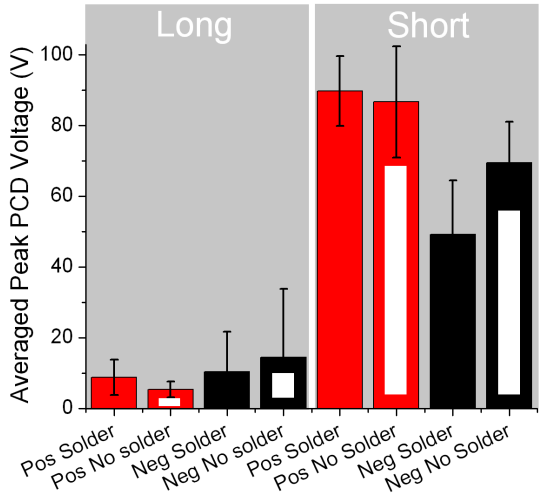

Figure 7.9: All eight cases of 6 μm Mylar filtered, collimated PCD: comparison of averaged peak powers.

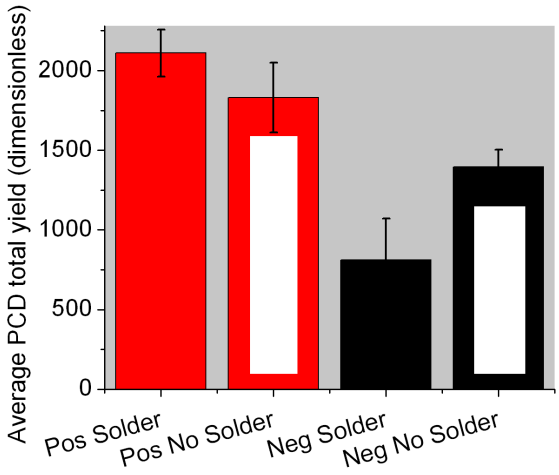

Figure 7.10: All four cases of short pulse only, 6 μm Mylar filtered, collimated PCD: comparison of averaged total yield. Total yield for long pulse is not shown because difficulties in determining a start and finish of the x-ray pulses led to lack of confidence in the analyzed results.

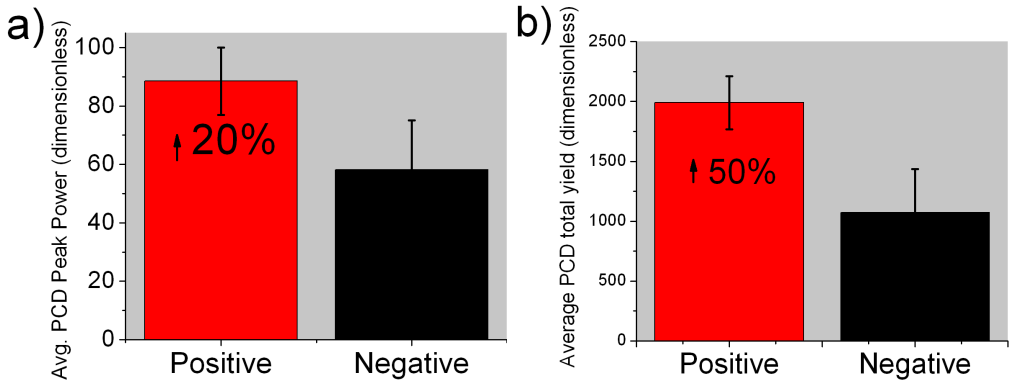

Figure 7.11: Averaged PCD (a) peak power and (b) total yield for positive vs. negative, short pulse only.

Table 7.6: Comparison of improvements in averaged minimum current radii and PCD data from operating in positive polarity, short pulse only.

Improvement by operating in positive polarity		
PCD peak power	PCD total yield	Minimum current radius
20%	50%	30%

more difficult to determine as there was rarely a defined point at which the PCD signal returned to zero. However, after comparing bolometer data for several shots taking different times as the end of emission, we determined that the introduced user error due to time selection was <~5%. Therefore, no complicated scheme was developed to determine the end of emission, and the end points were selected by eye.

The averaged bolometer data are shown in Figure 7.12. Comparing the bolometer data to the above PCD data, there are clearly differences when comparing the data. Whereas the PCDs showed an increase of 20% in peak power and 50% in total yield by operating in positive polarity vs. negative polarity,

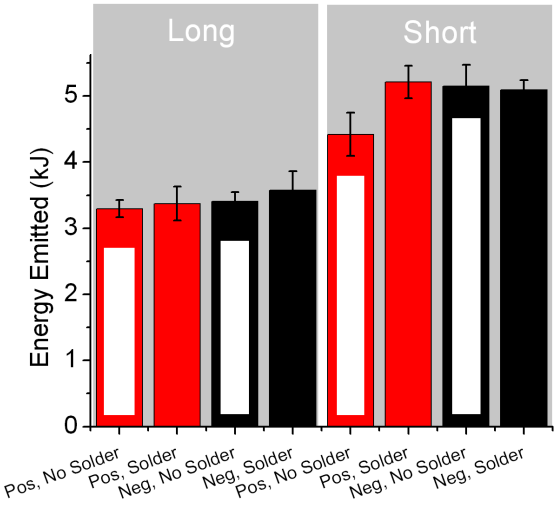

Figure 7.12: Averaged bolometer data, separated into eight cases from polarity, contact and risetime dataset.

the bolometer showed none. The factor of ten improvement in radiation observed by the PCDs in short vs. long pulse is reduced to a factor of two. We attribute this to the bolometer's sensitivity to UV and soft x-rays (10 eV-1 keV) and the proportional dominance of the aluminum array emission in this frequency range. We believe that this low-energy emission raised the baseline on the bolometer readings and drowned out any high-energy (>1 keV) differences. Since we are not particularly interested in UV emission, we have determined that the PCDs are more useful for forming comparisons, with regards to x-ray sourcing, between the eight cases. The bolometer data are useful, however, for reinforcing our conclusion that, with the arrays used and convolute installed, COBRA short pulses operate better with respect to x-ray emission than their long pulse counterparts (the specific percentage improvement of which is dependent upon the diagnostic results, PCD or bolometer, one puts their faith in).

7.3 Discussion and summary of polarity, contact and risetime dataset

7.3.1 Initiation and the correlation between deposited energy and x-ray power

As explained in detail in section 1.3.1.1, it is speculated in current literature that the amount of energy deposited during initiation must be within a certain range to have desirable pinch dynamics. This preferred state is an axially homogeneous, fully melted liquid. This generates the proper ablation rates, as described in section 1.3.1. We compared energy deposited during the initiation phase with x-ray yield and peak power as determined from the 6 μm Mylar filtered, collimated PCD. The short pulse results are shown in Figure 7.13 (we did not include long pulse results because of the undesirable x-ray pulses and general poor performance). We have also included plots breaking the peak power and total yield data down into the four cases in short pulse in Figure 7.14. If there were a relationship between deposited energy and x-ray yield, we would have seen a correlation on these plots. Our data, however, show no such correlation. The red line is not part of the source data nor is it a fit; it is a hand-drawn representation of the expected positive correlation inferred from literature.

It is worth noting, however, that we have not ruled out the possibility of the existence of a positive correlation for several reasons:

Firstly, it is possible that we were not operating in the deposited energy ranges inside which this positive correlation is theorized to exist (liquid core temperatures of ~0.1-3.5 eV/atom).

Secondly, if we re-examine the data and color the shots according to the four

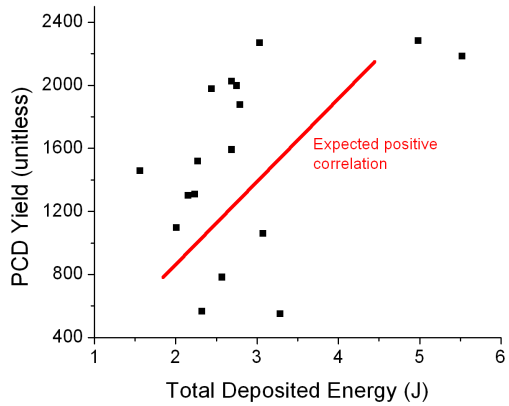

Figure 7.13: Deposited energy and PCD yield showed no correlation. The red line is not part of, nor a fit from the data, and is merely a representation of an expected positive correlation

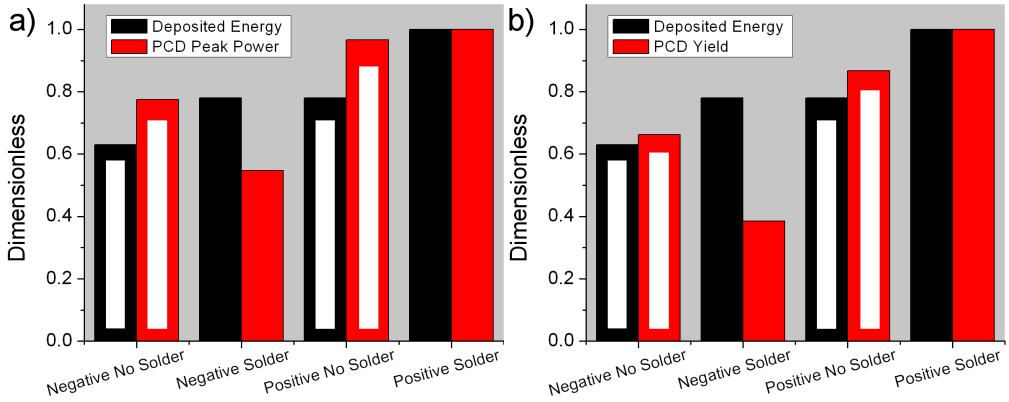

Figure 7.14: (a) Averaged deposited energy and (b) PCD peak power and yield separated into the four contact/polarity cases for short pulse only.

contact/polarity cases studied in short pulse, some interesting trends emerge (Figure 7.15). We see that the lowest PCD yield shots are all the same case - negative, soldered. We are unable to determine a reason for this decrease in PCD yield (we suspect the flux may have contaminated the results, but cannot determine this from the data). If we re-plot the data, considering as outliers these negative, soldered shots, as well as the two green points at the high end of the deposited energy axis, a positive correlation emerges. Again, the non-

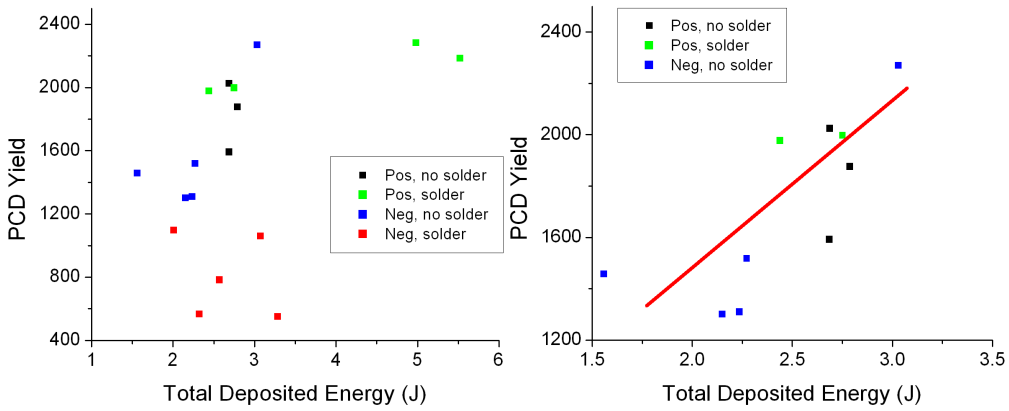

Figure 7.15: Deposited energy and PCD peak power and yield with (a) all data from the polarity, contact and risetime dataset included and the four cases colored separately, and (b) potential outliers removed. A positive correlation appears to arise when outliers are removed.

statistical techniques used to generate this plot did not warrant data fitting, so this is not a linear fit but is again hand-drawn. Future work will focus on this potential correlation, and hope to elucidate the reasons for decreased PCD yield with the negative, soldered case.

7.3.2 Improvements from positive polarity

Arrays operated in positive polarity were found to increase deposited energy during initiation on average by 25% over negative polarity. Positive polarity arrays with short pulses were also found to reach a 30% smaller current radius, which was visibly verified by a skinnier pinch column in the 4-frame XUV images. Positive polarity arrays with short pulses were found to improve average peak power radiated by 20% and to increase average total yield by 50%. It is also clear from the PCD signals that there were more late time x-ray bursts with positive polarity, which we suspect to be responsible for the disparity between the yield and power increases. It was visible from the streak camera images that

there were late-time wire trajectories, and these x-ray bursts may have been correlated with this wire material coming in after the first pinch. We suggest that, on a machine where the wire trajectories are more azimuthally correlated, these late-time bursts may be utilized to produce even greater peak powers. Therefore, on a machine with greater azimuthal correlation, we suspect the peak power increase of positive over negative arrays would be even greater than 20%. This warrants further research, and suggests that polarity experiments should be conducted on higher-current machines.

The origins of these power and yield increases, however, are unknown. Part of the scope of these experiments was to examine the effects of initiation and energy deposited on x-ray yield. While positive polarity did increase both the energy deposited during initiation and the x-ray output, including the negative polarity shots destroyed this positive correlation between energy deposited and x-ray output. Therefore, it is not clear from these data whether the increase in x-ray output was caused by positive polarity operation during the initiation (reduced explosive electron emission, greater hold-off of current-shunting plasma, etc.), or whether the effects occurred in later stages (improvement in ablation, implosion and stagnation). Separating these effects can be difficult, as we had limited diagnostics during these times, and often two shots had remarkably different x-ray pulse shapes but very similar shadowgraph or self-emission images. It is possible, however, that operating in positive polarity has improved the energy deposited during initiation and this subsequently improved the x-ray yield, and the lack of correlation in negative polarity was due to altogether different effects (e.g. the methods involved in soldering negative polarity arrays had confounding effects on the pinch). Unfortunately, these details were difficult to determine from this dataset, and warrant further research.

7.3.3 The effects of contact

We determined that arrays on COBRA do behave similarly to single wires on LCP3 with regards to contact. Negative polarity arrays showed no improvement, or even a reduction (but still within each other's error bars) in deposited energy when soldered. Energy deposited during initiation of positive polarity arrays, on the other hand, showed an improvement of 16% by soldering the wires to the contacts (recall that we are not comparing the two different di/dt cases to each other, for the reasons mentioned earlier). We do not have enough statistically significant data from the previous single wire experiments to make a direct comparison, but Duselis et al. [25] showed several hundred percent improvement in deposited energy by soldering a positive polarity wire to the electrode over a negative, non-soldered wire. We were significantly below this level of improvement, but differences were not surprising given the vastly different experimental configurations.

We did observe a correlation between contact and the appearance of the Christmas Tree effect in long pulses. This effect was not completely absent from non-soldered shots, but it was observed much more frequently on soldered shots. In short pulse mode, however, the Christmas tree is never observed, presumably due to the smaller array radius.

While there were improvements seen in energy deposited by soldering arrays in positive polarity to the electrodes, soldering did not result in improved peak powers in short pulse over non-soldered arrays. There was a slight improvement in yield, approximately 10%, again from what we believe to be late time wire implosion trajectories. While improving energy deposited is novel, it is not important if it does not subsequently increase x-ray peak power or total yield. In fact, the x-ray output of negative polarity shots was actually sig-

nificantly harmed. Additionally, the time and effort required to solder each individual array was enormous, and much development was spent on obtaining specific procedures for these specific arrays on COBRA. Due to the lack of substantial results, inevitable experimental variation in some of the soldering procedures, effort required for completion of each array, and greater chance of array breakage due to the wires being fixed, we do not recommend at this time that research into soldering as a means of modifying contact be continued. Other techniques to modify contact, including using a soft, malleable metal gasket at the electrode [72], have shown promise in single wire experiments. While we have seen little beneficial effect by improving wire-electrode contact substantially, we do not rule out the possibility that further experiments will diagnose different issues or outcomes. We also suggest that, if anode-cathode gap vacuum-induced motion can be circumvented, experiments be conducted with both ends soldered. It is also possible that different di/dt regimes during initiation will yield different results with regards to wire-electrode contact.

7.3.4 The effects of current risetime

PCD data on short pulse shots showed an order of magnitude improvement over long pulse shots in peak power and total yield for x-rays >1 keV. Bolometer data showed a smaller improvement, ~40%. We again attribute this difference between PCDs and the bolometer to the dominance of the emission spectrum by the relatively unimportant UV and sub-1 keV frequencies.

Modifying contact and polarity did nothing to substantially affect the difference between short and long pulse x-ray output. Additionally, the x-ray pulse shapes of arrays operated in long pulses were also very poor, with huge variation within a single case, and often did not have a single distinguished peak nor

could we determine a risetime to peak.

This poor performance could have been due to differences in the arrays we chose. As noted in the literature, spacing amongst the wires in an array, called the interwire gap, is very important to pinch dynamics [70, 73, 44, 8]. However, in order to keep electron emission as constant as possible, we chose to vary the array diameter, and therefore the interwire gap, instead of wire diameter. There was no way to use identical arrays for long and short shots as they would not be properly matched, and therefore not a fair comparison. However, it is recommended that further research be conducted into risetime holding different array variables constant. We also suggest re-examining the experiments on COBRA when the monotonic current pulse is fully developed.

The results of this dataset, however, are clear: our arrays operated with the double-humped long pulse performed significantly worse than with the short pulse. Therefore, in future examinations of polarity on COBRA, we do not recommend performing the experiments in both long and short pulse mode, unless other, significant evidence comes to light that suggests otherwise.

7.3.5 Disagreements between the two datasets

We do not currently understand why there are some substantial differences between the two datasets. The main difference is that the soldered, long pulse from the non-convolute dataset (therefore negative polarity) showed an improvement over the soldered case, but no improvement was seen in the convolute dataset. We are currently exploring this difference further, but have several suspicions about the reasons. Our main concern is that the inclusion of the convolute introduced a substantial difference between the two datasets. Therefore, it may not be accurate to make an A/B comparison between the non-convolute

negative polarity and convolute negative polarity cases.

We are also concerned with the impacts of the soldering process. It introduced inevitable experimental variation (amount of solder, amount of flux, etc.), and therefore we suspect the single-variable experimental control was lost, having unknown effects on dynamics of the pinch. The soldered, negative polarity, short pulse case showed a substantial decrease in x-rays, for which we can see no reason. We are suspicious that trace flux-residue remained, or some other variable which soldering introduced, and the quality of the pinch was impacted. In general, the variable nature of soldering the wire arrays is in question, and this is one of the reasons we are recommending abandoning experiments involving soldering wire arrays.

Also, despite the constant attention to controlling variables, the amount of time (~1 year) between the datasets may have introduced changes to COBRA that were not evident on the diagnostics available. For this reason, it is recommended that experiments so reliant upon statistical results be conducted in quick succession.

CHAPTER 8

CONCLUSIONS AND RECOMMENDATIONS

The following is a review of the questions posed for these experiments:

1. What are the effects of polarity, wire-electrode contact and current risetime on the initiation phase of wire array z-pinches?
2. What are the effects of polarity, wire-electrode contact and current risetime on the later phases of wire array z-pinches?
3. What are the impacts of initiation on later phases of wire array z-pinches?
4. Of what importance to wire array z-pinches are low current, single wire experiments?

A summary of the findings is as follows:

1. Current-routing polarity reversal has been successfully demonstrated with a reversible, bolt-on convolute on the COBRA pulsed power generator.
2. Operating wire array z-pinches in positive polarity showed a substantial increase in deposited energy (25%), x-ray peak power (20%), and total energy yield (50%), and a smaller average current radius (30%), with short pulses.
3. Soldering the wires to the electrodes showed improvements in deposited energy in positive polarity with short pulses. In this respect, the wire array z-pinches behaved similarly to low current, single wire experiments.
4. Arrays operated with lower di/dt, longer current risetimes universally showed significantly lower x-ray peak powers and total energies.

5. The impact of initiation on later stages appears very complex, but certain analyses suggest that a positive correlation may be present between increased energy deposition during initiation and increased x-ray output. Further investigation is recommended.

6. The utility of low-current, single wire experiments as they relate to wire array z-pinch experiments is still under question, and is dependent upon the findings of further investigations into the correlation between deposited energy during initiation and x-ray output. We do suspect, however, that deleterious effects on the pinch from soldering processes harmed the dataset. Eliminating data points (outliers) from these shots shows the expected positive correlation. We hope to confirm this with future experiments.

We recommend that future research be focused on the differences between positive and negative polarity, and that soldering, and its associated complications, be eliminated. Double-humped long pulse experiments did not achieve the same x-ray yield as short pulse shots, and as such should not be pursued in the interest of maximizing x-ray output in future experiments. However, there are certainly other useful experiments that can be conducted with long pulses. Also, it is possible that, once the monotonic long pulse becomes reproducible on COBRA, the current risetime variable of this research can be analyzed again to eliminate the possibility of spurious effects due to the region of positive di/dt on the double-humped long pulse.

Eliminating soldering and long pulses will allow more shots to be conducted for a given unit of time (soldering was very time-intensive), and the total dataset to be substantially smaller. Therefore, more shots can be conducted for the relevant cases, and statistical significance can be improved.

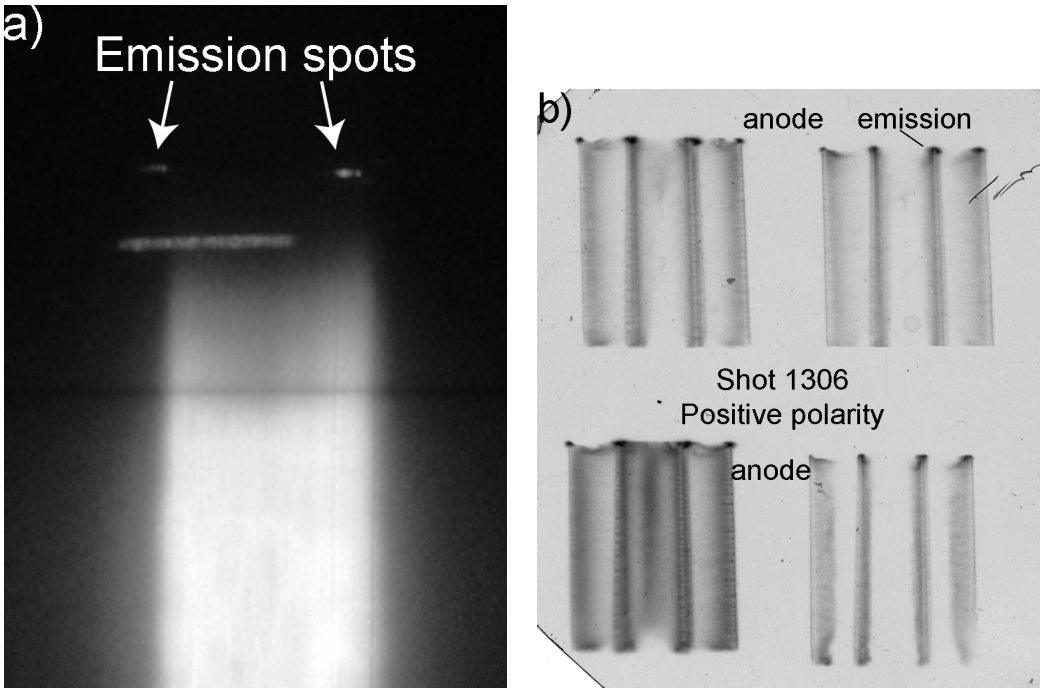

Figure 8.1: (a) Axial optical streak and (b) 4-frame self-emission XUV images show potential sources of emission at wire-electrode interface. The optical streak is shown courtesy of P. Knapp and S. Pikuz. The 4-frame image was taken from shot 1306, which was not included in any of the research here, but was a positive polarity convolute test shot.

Several other diagnostics and techniques should be employed for future experiments. Visual streak and 4-frame data have both shown potential emission spots at the wire-electrode interface, as shown in Figure 8.1. We recommend that these diagnostics be used to examine the potential mitigation of electron emission and arcing at the high-voltage electrode by operating in positive polarity.

It is also recommended that decreasing di/dt during the initiation phase be considered. The literature suggests that the wires should be in a homogeneous liquid state after initiation, but we surpassed this state and arrived in the vaporized state. It is unknown what effects this had on the later stages of the pinch.

Developing techniques to reduce COBRA early-time di/dt may allow initiation di/dt, and therefore energy deposited, to be low enough to leave the arrays in a homogeneous liquid state.

APPENDIX A

COBRA LASER WORK AND MAINTENANCE

A.1 Trigger laser

The laser used for output switch triggering is an EKSPLA NL303 Nd:YAG (Neodymium-doped Yttrium aluminum garnet) laser. The fundamental wavelength is 1,064 nm (infrared), but it is frequency doubled to 532 nm (green), and further quadrupled to 266 nm, the UV frequency desired for SF_6 spark gap triggering [50, 49, 48, 74]. The laser produces a 4 ns wide pulse, with ~800 mJ in fundamental and ~80 mJ in UV. The energy required to reliably trigger a spark gap switch is highly dependent upon geometry and setup, but we estimate that up to 20 mJ per switch is required for our specific setup[75, 76]. Given that we must split the 80 mJ beam into 3 equal parts (3 of the switches must be triggered, while the fourth self-breaks), the laser must be properly tuned to meet this requirement.

The laser is composed of a master oscillator (MO), frequency generating crystals, and frequency splitting crystals. I will describe the process used to rebuild this laser from a its components in the following sections. While this process may never again be required for this laser, it will be a good guide for understanding the methods of adjusting each component individually.

While such heavy maintenance may never be necessary, the laser will often slowly lose power. This is typical of a flashlamp powered laser, as the electrodes on the flashlamps age, slowly visibly blackening at the electrodes. The EKSPLA lasers have a provision for this in the form of a simple flashlamp voltage adjustment. The flashlamp voltage can periodically be increased to maintain adequate output energy. However, after several years or several million pulses, the flash-

lamps are beyond the point where a voltage adjustment can compensate, and they must be completely replaced. Note: flashlamps should always be replaced in pairs.

A.1.1 Basic ideas about master oscillator

The master oscillator is where the laser pulse is generated. The EKSPLA lasers currently used in the laboratory all have similar master oscillator designs. the master oscillators for the NL303 and SL312 are composed of several components that work in conjunction to provide a Q-switched pulse 4 ns wide. A Q-switched laser operates by creating flashlamp-pumped electron inversions in the Nd:YAG rod over a long time-scale (~200 μs in our case) but withholding lasing until peak inversion. The polarizer and Pockels Cell, which are in the cavity, in line with the rod and between the mirrors, work in conjunction to block lasing during this period. The polarizer reflects all light of one linear polarization, while transmitting light of the perpendicular polarization. Before Q-switching is desired and while the rod is being pumped by the flashlamps, light transmitted through the Pockels Cell gets rotated 45 degrees. The beam is then reflected off the back mirror, and a second pass through the Pockels Cell rotates the beam another 45 degrees for a total of 90 rotation. The beam, which was originally aligned with the polarizer's preferred linear polarization, is now perpendicular to this polarization and gets completely reflected. Therefore, the light cannot return to the rod and initiate lasing. Note: depending upon PC design, the actual rotations may be different, but they all operate in the same way: rotating the beam using input voltages while working in tandem with a polarizer to selectively dump the beam.

When Q-switching is desired, the bias across the Pockels Cell is inverted

(and is often of a different amplitude, but this is all internally controlled in the lasers and is not within the scope of this document). The Pockels Cell now no longer rotates the polarization as is passes through (or rotates it 90 degrees each pass, acting as a quarter-wave plate, depending on PC design). Therefore, on the second pass, the beam is of the correct linear polarization for the polarizer and is fully transmitted. This light is now allowed to interact with the rod and initiate lasing. The rod inversions are very rapidly swept up by the light transmitting through the cavity, and the result is a short, high-power pulse.

The efficiencies of the Pockels Cell and polarizer are highly tied to incident angle. If they are misaligned, incorrectly polarized light will leak through one or both of them and can create free-running. Free-running depletes some of the inversions in the rod, and reduces the energy delivered in the main pulse.

A.1.2 To build laser from components:

1. Remove polarizer and Pockels cell
2. Turn simmer on, use diffuse backlight at output end of laser to align rod ends and front mirror Gaussian
3. Use CW HeNe laser to further align front and back mirror. Only adjust back mirror.
4. Establish free-running and tune back mirror for best beam shape. One may have to turn up flashlamp voltage a bit to get adequate pumping.
5. Install polarizer. Adjust polarizer for maximum free running. Check beam shape to make sure it is still fairly circular
6. Install Pockels cell. Use coarse adjustment (rotation) to eliminate free-running. Check beam shape to make sure still circular (only hesitantly

touch mirrors at this point – the beam shape should be stable by this point). Use fine adjustment (allen wrench) when one cannot adjust rotation accurately enough.

7. Fine tune polarizer to get proper pulse width (4-5ns)
8. Turn up flashlamp voltage to ~10% above operating voltage and ensure free-running is not present.
9. Turn flashlamp voltage to operating voltage that corresponds to proper output energy (750-800 mJ in the fundamental). The master oscillator is now aligned and should not be touched further.
10. Ensure that beam travels through all downstream optics on-center and parallel to baseplate (harmonics and splitter crystals). If this is not the case, the beam must be steered (do not touch master oscillator! Only steer with external steering mirrors).
11. Remove fourth harmonic crystal and measure energy in green beam. Tune harmonics crystal first then quarter-wave plate to get to max green energy.
12. Install fourth harmonic crystal. Tune crystal for max UV energy.
13. Do not touch frequency splitters! Unless otherwise directed, assume one will be able to establish original beam path with steering mirror. Attempt this first before attempting the difficult job of adjusting splitting crystals.

Note: Since this document has been prepared, the steering mirror between the master oscillator and harmonics units has been removed to make alignment simpler. This steering mirror may be replaced if the operator is comfortable enough with laser maintenance.

A.1.3 Detailed description of laser master oscillator rebuild

To complete this operation, the laser must be easily accessible from all sides, so it should be removed from Faraday box and placed on external breadboard. Remove harmonics units and remove two bolts holding back plate on master oscillator so that the back mirror can be accessed.

Before removing polarizer and Pockels cell, make marks on the mounts (with a pen) so that they can be relocated when reinstalled. Remove the polarizer and pockels cell and place in lint-free tissue in a safe place.

The following part is difficult and can be time-consuming. Several different lights (flashlights, fiber optic lights, etc.) and tissue paper are required. Hold the tissue in front of the laser output and backlight it with the light. View from the back mirror and sight along the rod. Have somebody help by moving the light and changing light sources and paper thicknesses so that the Gaussian spot is visible on the front mirror (the dielectric coating on the rod ends is Gaussian shaped, and is used to obtain required beam profile). It will show up as a dark spot. Move your eye until both the rod ends are concentric, and adjust the front mirror so that the reflection of the Gaussian spot is also concentric with them. The front mirror will now be a fixed component, and one will align everything else to it.

To setup the rear mirror, align a HeNe laser so it points in to the cavity from the output end of the laser. It will be easiest if the HeNe can be translated as well as tilted so that one can accurately point it down the cavity. The laser should come out of the center of the front and rear mirrors. Use tissue paper to confirm this, and go back and forth between the mirrors and HeNe laser angle adjustments to make sure this is the case.

With the laser beam traveling down the center of the cavity, if the rear mirror

is aligned, any reflections from the front and rear mirrors should be collinear. Use tissue paper to find the reflection spot from the rear mirror by blocking the rear mirror reflection and seeing which of the spots disappears. This spot should be collinear with the input HeNe beam, so adjust the rear mirror to move the spot onto the HeNe output (all light traveling into the cavity will now travel back the same path it traveled in on).

At this point, the mirrors should be closely enough aligned that the cavity will free-run. Turn flashlamp voltage way down (~60% - all flashlamp voltages are given assuming flashlamps were replaced right before alignment was started), turn Electrooptics off, and use an Infrared (IR) detector to look for free running in "OF" mode. Adjust rear mirror to get a round beam shape. The profile will not be exactly Gaussian because it is designed to have a slight null in the center of the beam. Use the rear mirror to move this null to the center.

If one did not see free-running at 60% voltage, slowly turn flashlamp voltage up to perhaps 70%. It is possible that the rear mirror is not close enough from the HeNe alignment step to establish free-running. If the laser now free-runs, adjust the rear mirror to get a circular beam shape then turn voltage back down to 60% to eliminate the possibility of damaging any components – the rear mirror should be closer to properly adjusted and cavity should now free-run. Continue adjusting rear mirror at this lower voltage to get a good beam shape.

Once one has a circular beam profile with free-running, reinstall polarizer, and use alignment marks one made previously to get it close to where it used to be. With the polarizer installed but no pockels cell, there will be no rotation of the polarization, so the polarizer should dump very little of the beam. This means that the laser should be adjusted for maximum free-running, which means that the polarizer is letting as much light through as possible. To ac-

complish this, set-up a fast (sub-nanosecond) photodiode looking at the diffuse reflection from the beam. If the end is not terminated in 50 Ω (e.g. terminated in MΩ), the decay time should be long enough that the flashlamp pulse will be observable on the oscilloscope. It should be approximately 300 μs long, and be several hundred mV in amplitude. Free-running will show up as a sharp spike in the flashlamp pulse near the peak (after 200 μs or so). Rotate the polarizer so that this free-running pulse is maximized. The polarizer is very sensitive, so be aware. Do not do a final tightening of the bolts because fine-tuning the of the polarizer will be required later.

Now reinstall the Pockels Cell. Turn Electrooptics back on. With the polarizer and Pockels Cell installed and energized, one should be able to adjust Pockels Cell to remove free-running.

To accomplish this, pulse laser in "OFF" mode and look at the photodiode signal. Use an allen wrench to rotate pockels cell and eliminate free-running. Once one has gotten this adjustment as close as possible, use smaller allen wrench in small hole in pockels cell mount to fine-tune. Turn flashlamp voltage up incrementally and keep adjusting pockels cell to eliminate any free-running. If flashlamps were replaced, they should be adjusted to approximately 75% when done, so increase voltage to ~ 85% and make sure there is still no free-running, then turn the voltage back down to 60% or so. The pockels cell should now be aligned properly. Tighten the bolts securely, and ensure that the free-running does not return.

At this point, one should be able to Q-switch the laser. To keep components safe, always operate at a low power while adjusting. To accomplish this, change "AD" timing on keypad to approximately "3000."

Look at the Q-switched pulse on the photodiode. The polarizer has a big

impact on pulse width, so adjust the polarizer to get a 4-5ns pulse. There will be several small peaks superimposed on the main peak – these are the various longitudinal modes and are normal. With the correct peak chosen, tighten down the polarizer bolts, watching to make sure the pulse width does not increase when doing this. Re-check beam shape.

Turn the flashlamp voltage back up to 85% or so and ensure there is still no free-running in "OF" mode (adjustment of the polarizer may have affected this, although it is unlikely if the laser output is a 4-5ns pulse), then turn flashlamp voltage back down to 60%. Now use energy meter and turn flashlamp voltage up to get specified output energy.

The beam should now be a circular, 4-5ns wide pulse at the proper energy. Ensure that all these conditions are met.

A.2 Diagnostic Laser

The laser used for imaging, called the diagnostic laser, is an EKSPLA SL312. It is a Nd:YAG laser, with a 150 ps pulsewidth. At full power, the laser produces 250 mJ in the fundamental (1064 nm) and 120 mJ in green (532 nm). The master oscillator is very similar in physical layout to the NL303, but the outputs have some fundamentally different characteristics. After the master oscillator, the SL312 pulse is shortened in time by the Stimulated Brillouin Scattering (SBS) cell, described later, after which it is amplified to the output energy.

A.2.1 Quick checks of function of SL312

There are several quick checks to determine if the laser is operating correctly:

- When the SL312 is operating normally, the beam profile will be double

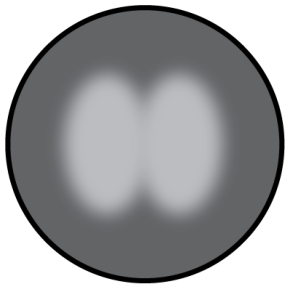

Figure A.1: Double-lobed profile of diagnostic laser.

lobed (not Gaussian, as seen in Figure A.1).

- The master oscillator Photodiode (PD) (read off the remote control in regime 1, 9) should be reading in the range of 3.45 – 3.65 μJ (independent of amplification – in fact amplification should be 01). This value will sometimes increase after 5-10 minutes of lasing.
- The Amplifier photodiode (regime 0, 2, 8) should read ~60 at 99 amplification.
- There should not be any harsh snapping coming from inside the chamber at 99 amplification.
- With harmonics unit removed, the fundamental output energy should be 250 mJ in the second harmonic at full power. Do not be afraid to remove the harmonics unit (although do not disconnect the heater connection). It must be removed to accurately determine the output energy, and will reinstall with only very minor readjustment necessary.

If the previous conditions are not met, it is likely that the laser will have to be tuned. Otherwise, the laser is likely running near-optimum.

A.2.2 Basic operation of the SL312

This is a slightly different cavity than most Nd:YAG Q-switched lasers, including the NL303 described earlier. There is an intentional low level of free-running before the Q-switch occurs, which is not typical. This free-running, coupled with the Fabry-Perot etalon (a form of frequency bandpass filter) and Nd:YAG adsorbing crystal, sets up the single longitudinal mode. This selection process creates a "survival of the fittest" of the free-running pulses, and is essentially a method to produce self-seeding. The single longitudinal mode means that only one longitudinal packet of lasing exists - all the wavefronts line up. If there are multiple packets of aligned wavefronts, the efficiency of the SBS cell would be affected, and the desired output will not be achieved.

This laser also has a unique feedback control mechanism which allows the master oscillator cavity to be slightly misaligned and still operate properly. The feedback operates in the following fashion:

- Flashlamps fire
- Once peak inversion nears (~200 μs), the voltage across the Pockels Cell increases. The Pockels Cell is designed with a variable control of the voltage across it, controlling the amount of transmission of the polarized light that will escape through the polarizer and create free running. This allows a degree of control of free-running, which is desirable to setup the pre-lasing necessary for the single longitudinal mode.
- The feedback mechanism then uses the master oscillator photodiode signal to maintain the desired amount of pre-lasing by controlling the voltage on the second section of the Pockels Cell. The amount of time for which this occurs is indicated (and can be controlled) on the remote pad under

"Feedback time menu," shown with a Δ (adjustment of this will be covered later).

- Once the desired pre-lasing time is achieved, the full voltage is placed across the Pockels Cell, switching it completely, and Q-switched lasing occurs.

After exiting the master oscillator, the 0.8 mm diameter pulse gets focused into the Stimulated Brillouin Scattering (SBS) cell. Stimulated Brillouin Scattering is the process by which density variations in a medium can change the frequency or path of light traveling through it. The situation in which we are interested involves a propagating beam of light being reflected back in the direction from which it came, and with the same phase variation. This specific effect, which utilizes SBS, is called optical phase conjugation. The plane at which the optical phase conjugation occurs is called a phase conjugate mirror.

The SL312 uses the the incoming laser beam itself to create a phase conjugate mirror. This mirror is established within the cell at a certain threshold of deposited energy, which comes from energy deposited from the laser beam as it travels through the medium. The laser light is focused into the cell, which has the effect of depositing an increasing amount of energy per unit volume the further it travels into the cell (energy deposited increases as the beam cross section decreases). Therefore, as the amount of energy per unit volume deposited increases, the plane of the OPC mirror moves closer to the incoming pulse. The plane of the mirror moving rapidly towards the incoming light, reflecting the light as it moves towards it, which has the effect of compressing the pulse in time. The 3 ns wide pulse is reflected as a 150 ps pulse, and travels back out the cell and continues on to the amplifier circuit.

After leaving the SBS cell, the beam is passed through the amplifier rod three

times, which is a pumped Nd:YAG rod as well. The first pass is unexpanded and at a slight angle. The beam then gets expanded to ~4mm, and passes through the amplifier rod twice more.

The final output of the amplifier stage has two lobes of intensity, and is therefore non-Gaussian. This is done to eliminate hotspots and therefore damage to any internal optical components.

The beam then goes through the harmonic crystal, where the 532nm frequency is generated. Finally, these two beams are separated and output different apertures.

A.2.3 Maintenance on the SL312

Note: Always place burn paper in a plastic bag to prevent debris from getting on optics

Master Oscillator Adjustment

If the master oscillator is the suspected source of the problem, there are three simple things to check. If these three conditions are satisfied, then there is no reason to suspect the master oscillator, and one should move on to aligning the amplifier or harmonic crystal.

- Electrooptical signal (with feedback off) should have the general shape of the left plot on page 8-4 of the user manual. The plot shown peaks negatively at ~150mV. Anywhere between 150mV and 400mV is acceptable.
- The photodiode energy (read off the control panel in regime 9) should read ~3.45-3.65 (which is the energy in μJ from the cavity photodiode).
- The beam should be roughly Gaussian and circular (use burn-paper before the polarizer). The beam is quite small at this point, so the easiest way to determine if it is circular is to look for flares or diffraction rings at the edge.

The most common evidence of master oscillator problems is a rapid fluctuation in output intensity. This is from the SBS cell, which requires specific output conditions from the master oscillator. If these conditions are not met, the output of the SBS cell is chaotic.

This problem can often arise from dust on the master oscillator rod. Cleaning the rod should be the first step, and will often solve this problem. If the problem persists, adjustment of the master oscillator is necessary.

To adjust master oscillator, turn off feedback control, and turn thumbscrews (both vertical and horizontal) on back mirror of master oscillator to obtain maximum photodiode energy while still having the desired oscilloscope trace. Maximum photodiode energy does not necessarily have the desired pulse shape (there might be no pre-lasing), so take care to find compromise between both pulse shape and maximum energy.

It is unlikely that the pre-lasing time will have to be changed, located in the "Feedback time menu," because proper alignment of the master oscillator should require the same pre-lasing time as from the factory. However, if the Q-switching does not happen at the end of the pre-lasing signal valley, try changing the right value on the screen so that the laser tries to match it, thereby changing where the Q-switching occurs. This will have a slight effect on output energy, so again try to maintain maximum output energy.

If this adjustment does not provide suitable energy, consider turning up the flashlamp voltage (the lamps will wear out over time – 2000 hours of operation or 6-10 million pulses is a typical lifetime. This can be checked on the back of the power supply cabinet). However, this is a last resort as it will prematurely age flashlamps if done too soon.

Note: If feedback is left on, then the laser will try to compensate for bad

alignment with the feedback, and therefore the cavity will not necessarily be optimized upon adjustment.

The master oscillator controls are all coupled complexly, and changing one often affects the others. Therefore, it is usual to have to adjust the back mirror, flashlamp voltage, pre-lasing time and Q-switch voltage iteratively to obtain the optimum pulse.

Amplifier Adjustment

The beam passes through the amplifier rod three times. The first time is unexpanded, the it gets expanded and makes two more passes. The first pass is at an angle through the rod, when the beam is much smaller than the rod and therefore rarely goes so much out of alignment that it's hitting the edge of the rod. If the master oscillator is properly aligned and no other mirrors have moved, this pass should never need adjustment.

The next thing to check is if the beam is going through the aperture A2 properly. Use burn paper on either side of the aperture to see if the shape changes from hitting one of the sides. The beam is still quite small, but it is possible to determine irregularities in the profile. Again, if the master oscillator is properly aligned, the beam should easily pass through the aperture.

For the second pass, use burn paper in front of mirror M10. The amplifier should be set to about 65 on the remote to obtain the proper intensity. This is a dangerous amplification to work at because back reflections may cause permanent damage at this level. Therefore, always work with the laser in single shot mode ("Pk" menu), and always block mirror M10 with the burn paper so the beam cannot propagate any further. A nearly symmetric profile is desired, but it should not be perfectly Gaussian. If the beam is Gaussian, adjust mirror M8 slightly so that the beam is no longer Gaussian (this laser must be intentionally

misaligned to prevent hotspots in the Nd:YAG rod). The shape should look like it is starting to get the double-lobed profile that is desirable after the third pass (Figure A.1). There should also be no diffraction lines around the outside of the beam, as this indicates that the beam is hitting an edge somewhere. Again, adjust mirror M8 to prevent this.

To align the third pass, hold burn paper in front of the harmonic crystal, and look for the characteristic double lobed pattern. Use mirror M10 to optimize this profile. Mirror M10 is the least sensitive to adjustment of the mirrors. Again, diffraction rings should be completely eliminated.

Harmonic Crystal

The harmonic crystal is extremely sensitive to adjustment around the vertical axis (twist), but not sensitive to adjustment about the horizontal axis (tilt). Therefore, to eliminate back-reflections into the laser optics, the vertical alignment is purposefully not normal to the incident beam. **Do not adjust the tilt of the mirror.** It was aligned with a square so that it is several degrees off vertical.

If tilt was accidentally adjusted, use a square against the mounting bracket, and intentionally tilt the mirror several degrees (3-4 turns of the thumbscrew off of vertical) so that the back-reflection is directed towards the floorplate of the laser.

When adjusting the twist, note that there is more than one peak to the transmission curve. Typically, there are three peaks, and the middle one is the most desirable (and also the most intense by far - 5-10x higher). If only a slight adjustment is necessary, and one can assume that the laser is still on the same peak (it will take at least ¼ turn to go from one peak to the next), do not try to find any other peak. However, if the laser maintenance is starting from scratch, or is staring from scratch or an adjustment upstream has been made (master oscilla-

tor or amplifier), then it is a good idea to turn the thumbscrew to either side to make sure adjustment is in the middle peak.

The quarter-wave plate must also be rotated (very slightly – 1/32 increments - as it is extremely sensitive) to optimize output energy.

Eliminating Back-Reflections

There are two main sources of back-reflections that can be dangerous.

- Harmonic crystal back-reflections
- Depolarized light backscatter

If the harmonic crystal was properly aligned according to the above method, then there should be no back-reflections from it.

The depolarized light comes from thermal effects in the Nd:YAG rod, which depolarizes some of the incident light. Therefore, it will not pass through the polarizer on the third pass, and will be reflected back towards the master oscillator. To protect the Pockels Cell (the most likely component to get damaged by back-reflections), EKSPLA has intentionally made the incident and reflected beams on M10 slightly off coaxial. This ensures that the depolarized backscattered light will not trace the beam all the way back to the master oscillator, and will get blocked by the aperture. Make sure that this is happening by looking for the beam hitting the back of the aperture. If properly aligned, the backscattered beam will hit the aperture at about 11 O'clock. The back-reflected beam is usually an annulus about 1 cm in diameter, sometimes resembling a crescent moon.

NOTE: when checking for reflections, keep the laser at a maximum of 25 amplification, as this will probably not have enough energy to harm anything. Once the amplifier is set to 40-50, the backreflections will have enough energy to do damage. Sometimes it is necessary to bring the amplification up to 40-45

to see the depolarized backscatter, but be very careful when doing this. Listen very carefully for the onset of snapping within the laser.

This laser is designed so that the beam center is always 50 mm off of the ground plate. One can use a machined plate with a hole at 50mm to inspect for back-reflections (allow the beam to pass through it and look for reflections on the back side - much like the aperture).

APPENDIX B

GLORY CIRCUIT WALKTHROUGH

The internal operation of the Glory Circuit is explained below. Please refer to Figures B.2 for a complete schematic of the Glory Circuit.

The three separate stages of the circuit are shown in greater detail in Figures. B.2, B.3 and B.4.

The output of NOR gate U7 is referred to as "RESET." The output of U8 is referred to as "SET." The output of U9 is referred to as "SEQUENCE." These names correspond to the names on the LEDs on the front panel of the Glory Box. the LEDs on the front will indicate when a state is logically high by lighting up.

The outputs are collectively referred to as "FIRE."

B.1 Glory Box Input Stage - TRIG-in and CLOCK-in

The Glory Box is designed to operate with a 0-10 Hz +5 V clock signal and a user-operated trigger input, which must be a positive, rising pulse greater than 5 V. These signals are connected to the CLOCK-in and TRIG-in, respectively, and are initially handled in the input stage.

The input stage, shown in Figure B.2, converts this 0-10 Hz clock signal to a ~500 μs wide pulse at the original clock frequency. The main device that accomplishes this is U6, a 555 timer. The R-C time (established by R5 and C7) is configured such that, when triggered, it outputs a 500 μs pulse. This stage also maintains the TRIG-in signal between 0 and +5 V via the clamping diodes at the TRIG-in input.

Assuming a constantly running clock input pulse, U4 is waiting for CLOCK-in and the output of U3 to be coincidentally high so it can pass on. Before receiving a trigger, the output of U22 remains at a steady-state high value. When

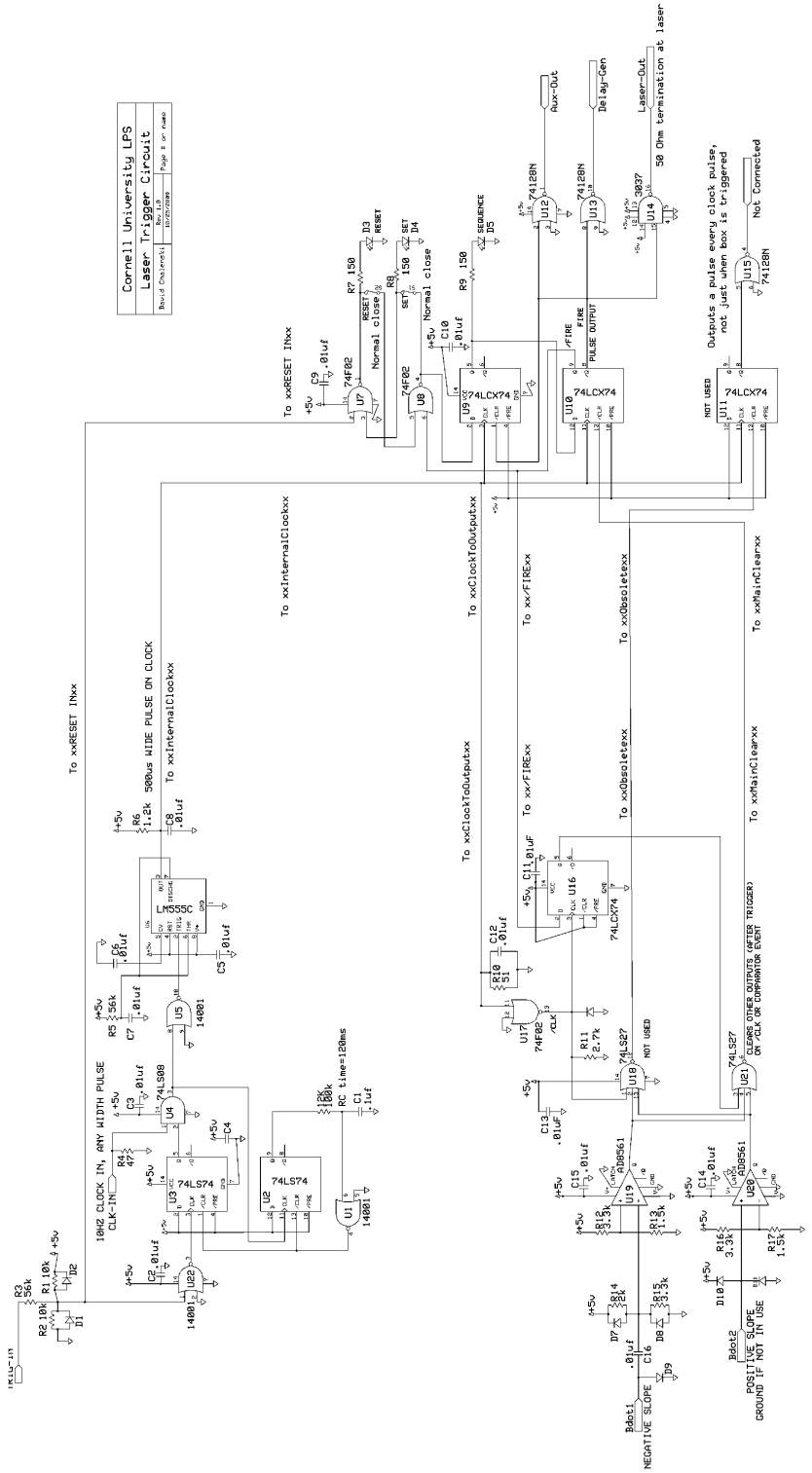

Figure B.1: Glory Circuit Schematic - Complete

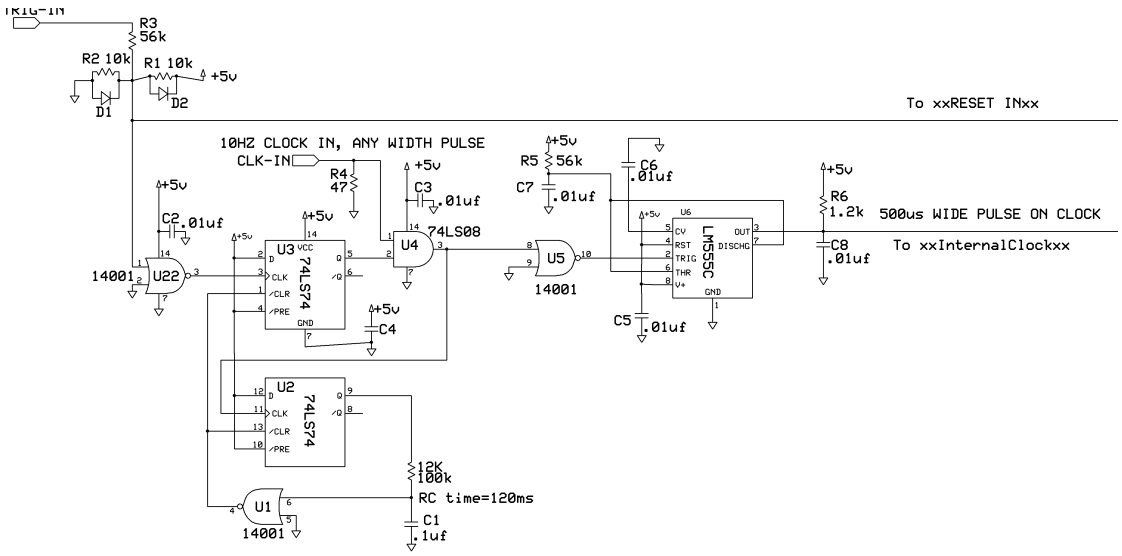

Figure B.2: Glory Circuit Schematic - Clock and Trigger Inputs

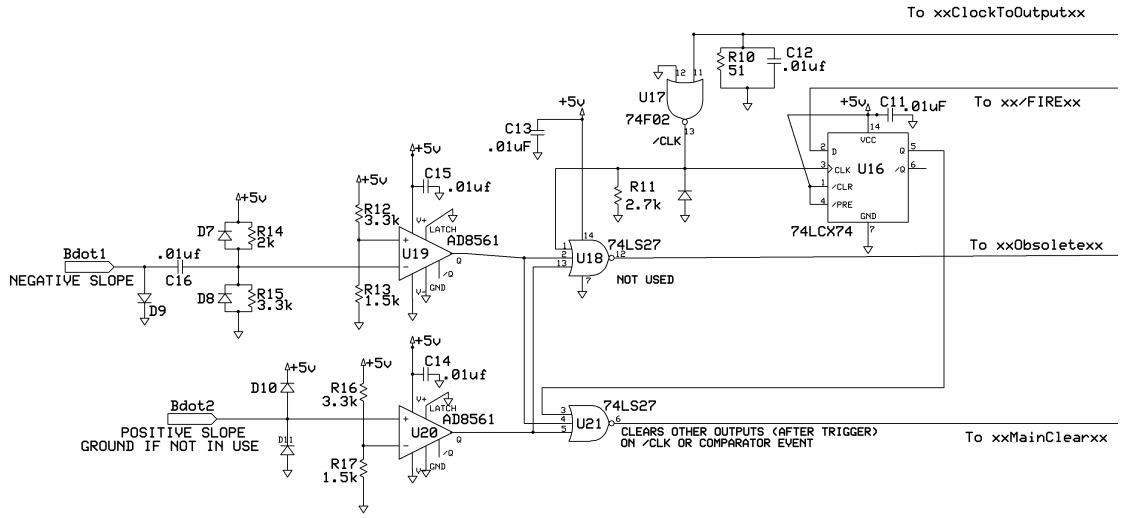

Figure B.3: Glory Circuit Schematic - $\dot{B}$ Inputs and Comparators

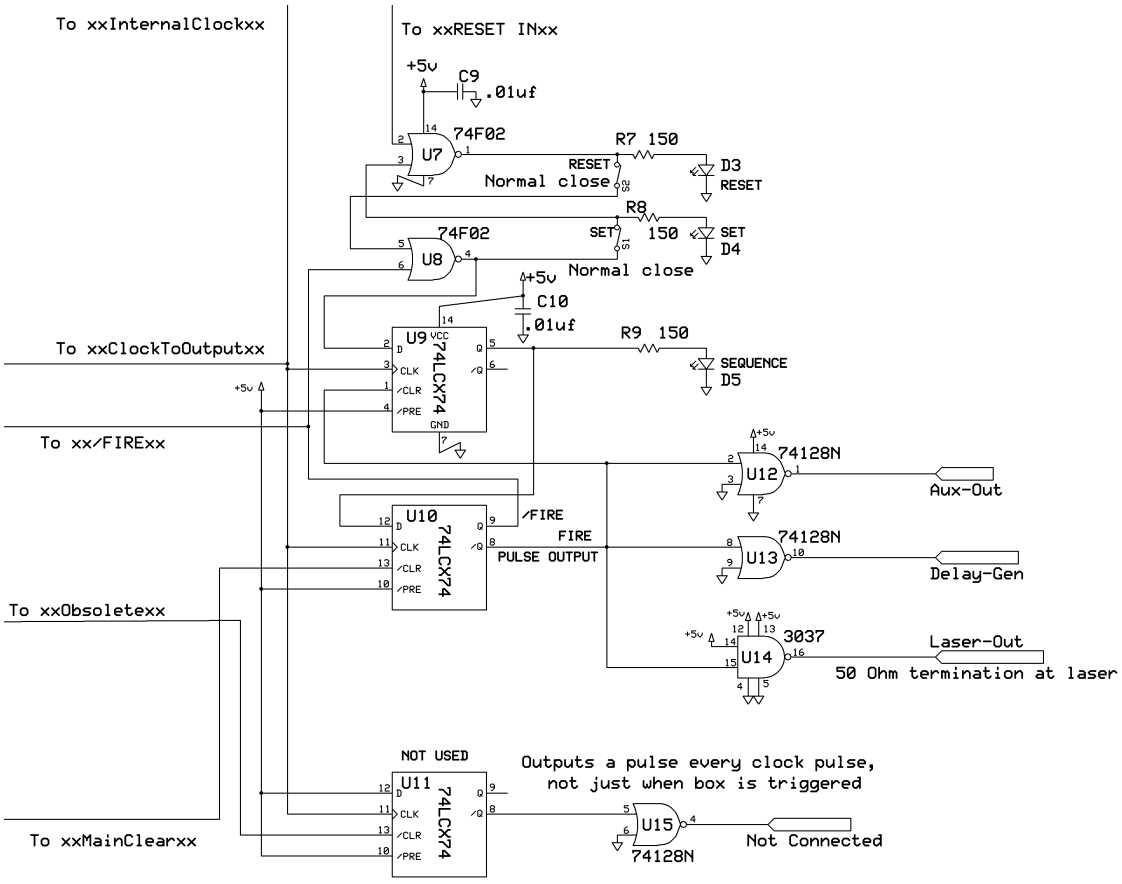

Figure B.4: Glory Circuit Schematic - Output Stages

TRIG-in goes high, U22 sends a falling edge to U3, which does not read this because it is the falling edge. This delay is built in so that other elements of the circuit, namely the reset-set-sequence-fire loop, will establish the correct levels. However, once the input trigger to the Glory Box goes low again, U22 passes a rising-edge signal to U3, the output of which will remain high until it is reset. When the output of U3 and CLOCK-in are both high, U5 passes this high signal to U6, which now independently sends out the appropriate 500 μs pulse. This pulse is read downstream as the clock input to the various flip-flops.

The resetting of the input stage is accomplished via U2, which passes a high signal upon the previously explained instance of U4 going high. The R-C circuit

on the output of U2 is set to ~120 ms, and doesn't pass this high signal to U1 until this time has elapsed. This ensures that the output of U3 is high long enough to catch only one clock signal, which occur every 100 ms. Once 120 ms has elapsed, U3 is cleared, and the output of U4 will remain low until another TRIG-in event.

B.2 Glory Box Steady State - No Input on TRIG-in, CLOCK-in Irrelevant

Assuming no set state anywhere, no TRIG-in event, and clock signal on CLOCK-in, the circuit can be reset and placed in a steady-state by pushing the RESET button. This is accomplished by a a feedback loop that guarantees that FIRE goes low within one clock cycle after RESET is depressed. If the reset button is pressed, RESET will float, and output of U8 will go low (this is due to the TTL nature of the specific NOR gate used, whereby a floating input is equivalent to high). This low gets passed through U9 at next clock rising edge to SEQUENCE. This in turn gets passed through U11 at next clock rising edge, and FIRE goes low, maintaining SET at low via U8. The output of U8 will now force RESET high from U7. The inputs and outputs to U8 are now stabilized, and the circuit will remain at steady state assuming no further inputs.

Note: diodes indicating READY (corresponding to RESET) and SET will not light up immediately when either button is pressed, only when released, because they are on the side of the switches with the inputs to gates, not the outputs which have gone high.

Circuit is now stable and ready to accept input. Current state: RESET: high, SET: low, SEQUENCE: low, FIRE: low

B.3 Glory Box With Operation of COBRA (user inputs signal on TRIG-in)

Assume circuit in stable reset mode with the following conditions: RESET: high, SET: low, SEQUENCE: low, FIRE: low.

Pushing the trigger button at the control panel sends a positive pulse to the input of U7. This forces the output (RESET) to low. This in turn causes the output of U8 (SET) to go high. This will be passed through U9 to SEQUENCE at the next rising edge of the output of the 555-timer (labeled "xxInternalClockxx"). SEQUENCE will be passed through U11 to FIRE and /FIRE after the 555 timer outputs a rising edge. /FIRE in the high state previously inhibited output from U12, U13 and U14, but /FIRE going low is now passed through to the output, which remains high as long as /FIRE is low (until U10 is reset).

The conditions of FIRE high and /FIRE low clear SET through U8 and SEQUENCE through U9.

The time when U10 is reset determines the length of the pulse. U10 is reset when the output of U21, a three-input NOR gate, is low. Of the three inputs to U21, two are from comparators connected to the $\dot{B}$ inputs. The other input remains low until a falling edge of the 500 μs clock pulse (via U1 and U18).

The comparator circuits are shown in figure B.3. The 8561 Comparators take two inputs, V+ and V-, and compare them with the output dependent upon the relative values. These inputs are not logic inputs, and therefore are voltages between 0 and +5 V. If V+ is higher than V-, the output is 5 V (high). If V- is greater than V+, the output is 0 V (low).

BDOT1 is DC-blocked from the input of U19, which is clamped at ~3 V by the D7/D8 diode/resistor network. V+ of U19 is clamped by a resistor network

to 1.5 V. Therefore, with no $\dot{B}$ input, V- > V+ and the output is low. If a $\dot{B}$ event occurs (characterized by a negative spike across the Bdot1 input), the is capacitively coupled to V-, dropping it momentarily, meeting the condition of V+ > V-, and the output briefly goes high. This event alone will drop the output of U18, resetting the main Glory Box outputs coincidentally with a $\dot{B}$ event.

The BDOT2 section works in a similar fashion to BDOT1, but is designed such that BDOT2 first goes positive. Therefore, V+ is usually less than V- unless a $\dot{B}$ event occurs, during which V+ briefly goes above V-, and the output of U20 goes high. Note: this difference in input polarities may be changed in future generations of the Glory Circuit.

B.4 Notes on Speed of Glory Circuit

The Glory Circuit is a very fast circuit, with throughput times of approximately 20-30 ns. This is accomplished through several techniques, the most important of which is component selection. LCX and LS series components were selected for their high-speed operation. The Vcc inputs of most gates are also designed with 0.01 μF capacitors between +5 V and ground. These capacitors provide a low-inductance supply of current for fast switching of the gates. The circuit is also mounted on a board with a ground plane on one side, which minimizes inductance of the leads.

BIBLIOGRAPHY

[1] D.H. McDaniel, M.G. Mazarakis, D.E. Bliss, J.M. Elizondo, H.C. Harjes, H.C. Ives, D.L. Kitterman, J.E. Maenchen, T.D. Pointon, S.E. Rosenthal, D.L. Smith, K.W. Struve, W.A. Stygar, E.A. Weinbrecht, D.L. Johnson, and J.P. Corley. The ZR refurbishment project. In *Power Modulator Symposium, 2002 and 2002 High-Voltage Workshop. Conference Record of the Twenty-Fifth International*, pages 252–256, 2002.

[2] R.B. Spielman and J.S. De Groot. Z pinches-A historical view. *Laser and Particle Beams*, 19(04):509–525, 2001.

[3] J.C. Martin. Nanosecond pulse techniques. *Proceedings of the IEEE*, 80(6):934–945, 1992.

[4] T. H. Martin. Design and performance of the sandia laboratories hermes II flash X-Ray generator. *Nuclear Science, IEEE Transactions on*, 16(3):59–63, 1969.

[5] J.C. Martin, T.H. Martin, A.H. Guenther, and M. Kristiansen. *JC Martin on pulsed power*. Plenum Publishing Corporation, 1996.

[6] R.B. Spielman, F. Long, T.H. Martin, J.W. Poukey, D.B. Seidel, W. Shoup, W.A. Stygar, D.H. McDaniel, M.A. Mostrom, K.W. Struve, P. Corcoran, I. Smith, and P. Spence. PBFA II-Z: a 20-MA driver for z-pinch experiments. In *Pulsed Power Conference, 1995. Digest of Technical Papers., Tenth IEEE International*, volume 1, pages 396–404 vol.1, 1995.

[7] R. B Spielman, S. F Breeze, and C. [and others Deeney. *PBFA Z: A 20-MA z-pinch driver for plasma radiation sources*. 1996.

[8] T. W. L. Sanford, G. O. Allshouse, B. M. Marder, T. J. Nash, R. C. Mock, R. B. Spielman, J. F. Seamen, J. S. McGurn, D. Jobe, T. L. Gilliland, M. Vargas, K. W. Struve, W. A. Stygar, M. R. Douglas, M. K. Matzen, J. H. Hammer, J. S. De Groot, J. L. Eddleman, D. L. Peterson, D. Mosher, K. G. Whitney, J. W. Thornhill, P. E. Pulsifer, J. P. Apruzese, and Y. Maron. Improved symmetry greatly increases X-Ray power from Wire-Array Z-Pinches. *Physical Review Letters*, 77(25):5063, December 1996.

[9] C. Deeney, T. J. Nash, R. B. Spielman, J. F. Seaman, G. C. Chandler, K. W. Struve, J. L. Porter, W. A. Stygar, J. S. McGurn, D. O. Jobe, T. L. Gilliland, J. A. Torres, M. F. Vargas, L. E. Ruggles, S. Breeze, R. C. Mock, M. R. Douglas, D. L. Fehl, D. H. McDaniel, M. K. Matzen, D. L. Peterson, W. Matuska,

N. F. Roderick, and J. J. MacFarlane. Power enhancement by increasing the initial array radius and wire number of tungsten z pinches. *Physical Review E*, 56(5):5945, November 1997.

[10] G. R. Bennett, I. C. Smith, J. E. Shores, D. B. Sinars, G. Robertson, B. W. Atherton, M. C. Jones, and J. L. Porter. 2–20 ns interframe time 2-frame 6.151 keV x-ray imaging on the recently upgraded z accelerator: A progress report. In *Proceedings of the 17th Topical Conference on High-Temperature Plasma Diagnostics*, volume 79, pages 10E914–3, Albuquerque, New Mexico (USA), October 2008. AIP.

[11] E.A. Weinbrecht, D.H. McDaniel, and D.D. Bloomquist. The z refurbishment project (ZR) at sandia national laboratories. In *Pulsed Power Conference, 2003. Digest of Technical Papers. PPC-2003. 14th IEEE International*, volume 1, pages 157–162 Vol.1, 2003.

[12] M. G. Haines, S. V. Lebedev, J. P. Chittenden, F. N. Beg, S. N. Bland, and A. E. Dangor. The past, present, and future of z pinches. In *Phys. Plasmas*, volume 7, pages 1672–1680. AIP, 2000.

[13] J. B. Greenly, J. D. Douglas, D. A. Hammer, B. R. Kusse, S. C. Glidden, and H. D. Sanders. A 1 MA, variable risetime pulse generator for high energy density plasma research. *Review of Scientific Instruments*, 79(7):073501–5, July 2008.

[14] J. D. Douglass, S. A. Pikuz, T. A. Shelkovenko, D. A. Hammer, S. N. Bland, S. C. Bott, and R. D. McBride. Structure of the dense cores and ablation plasmas in the initiation phase of tungsten wire-array z pinches. *Physics of Plasmas*, 14(1):012704–9, 2007.

[15] R. D. McBride, T. A. Shelkovenko, S. A. Pikuz, D. A. Hammer, J. B. Greenly, B. R. Kusse, J. D. Douglass, P. F. Knapp, K. S. Bell, I. C. Blesener, and D. A. Chalenski. Implosion dynamics and radiation characteristics of wire-array z pinches on the cornell beam research accelerator. *Physics of Plasmas*, 16(1):012706–15, 2009.

[16] T. A. Shelkovenko, D. A. Chalenski, K. M. Chandler, J. D. Douglass, J. B. Greenly, D. A. Hammer, B. R. Kusse, R. D. McBride, and S. A. Pikuz. Diagnostics on the COBRA pulsed power generator. In *Rev. Sci. Instrum.*, volume 77, pages 10F521–5. AIP, October 2006.

[17] C. Deeney, M. R. Douglas, R. B. Spielman, T. J. Nash, D. L. Peterson, P. L'Eplattenier, G. A. Chandler, J. F. Seamen, and K. W. Struve. Enhance-

ment of X-Ray power from a z pinch using Nested-Wire arrays. *Physical Review Letters*, 81(22):4883, November 1998.

[18] R. B. Spielman, C. Deeney, G. A. Chandler, M. R. Douglas, D. L. Fehl, M. K. Matzen, D. H. McDaniel, T. J. Nash, J. L. Porter, T. W. L. Sanford, J. F. Seamen, W. A. Stygar, K. W. Struve, S. P. Breeze, J. S. McGurn, J. A. Torres, D. M. Zagar, T. L. Gilliland, D. O. Jobe, J. L. McKenney, R. C. Mock, M. Vargas, T. Wagoner, and D. L. Peterson. Tungsten wire-array z-pinch experiments at 200 TW and 2 MJ. *Physics of Plasmas*, 5(5):2105–2111, May 1998.

[19] M. E. Cuneo, E. M. Waisman, S. V. Lebedev, J. P. Chittenden, W. A. Stygar, G. A. Chandler, R. A. Vesey, E. P. Yu, T. J. Nash, D. E. Bliss, G. S. Sarkisov, T. C. Wagoner, G. R. Bennett, D. B. Sinars, J. L. Porter, W. W. Simpson, L. E. Ruggles, D. F. Wenger, C. J. Garasi, B. V. Oliver, R A. Aragon, W. E. Fowler, M. C. Hettrick, G. C. Idzorek, D. Johnson, K. Keller, and S. E. Lazier. Characteristics and scaling of tungsten-wire-array z -pinch implosion dynamics at 20 MA. *Physical Review E*, 71(4):046406, 2005.

[20] C Olsen, G Rochau, and S Slutz. Development path for Z-Pinch IFE. *Fusion Science and Technology*, 47(3), 2005.

[21] Michael G. Mazarakis, Michael E. Cuneo, William A. Stygar, Henry C. Harjes, Daniel B. Sinars, Brent M. Jones, Christopher Deeney, Eduardo M. Waisman, Thomas J. Nash, Kenneth W. Struve, and Dillon H. McDaniel. X-ray emission current scaling experiments for compact single-tungsten-wire arrays at 80-nanosecond implosion times. *Physical Review E (Statistical, Nonlinear, and Soft Matter Physics)*, 79(1):016412–15, 2009.

[22] R. W. Lemke, D. B. Sinars, E. M. Waisman, M. E. Cuneo, E. P. Yu, T. A. Haill, H. L. Hanshaw, T. A. Brunner, C. A. Jennings, W. A. Stygar, M. P. Desjarlais, T. A. Mehlhorn, and J. L. Porter. Effects of mass ablation on the scaling of X-Ray power with current in Wire-Array z pinches. *Physical Review Letters*, 102(2):025005–4, 2009.

[23] R.J. Leeper, T.E. Alberts, J.R. Asay, P.M. Baca, K.L. Baker, S.P. Breeze, G.A. Chandler, D.L. Cook, G.W. Cooper, C. Deeney, M.S. Derzon, M.R. Douglas, D.L. Fehl, T. Gilliland, D.E. Hebron, M.J. Hurst, D.O. Jobe, J.W. Kellogg, J.S. Lash, S.E. Lazier, M.K. Matzen, D.H. McDaniel, J.S. McGurn, T.A. Mehlhorn, A.R. Moats, R.C. Mock, D.J. Muron, T.J. Nash, R.E. Olson, J.L. Porter, J.P. Quintenz, P.V. Reyes, L.E. Ruggles, C.L. Ruiz, T.W.L. Sanford, F.A. Schmidlapp, J.F. Seamen, R.B. Spielman, M.A. Stark, K.W. Struve, W.A. Stygar, D.R. Tibbetts-Russell, J.A. Torres, M. Vargas, T.C. Wagoner,

C. Wakefield, J.H. Hammer, D.D. Ryutov, M. Tabak, S.C. Wilks, R.L. Bowers, K.D. McLenithan, and D.L. Peterson. Z pinch driven inertial confinement fusion target physics research at sandia national laboratories. *Nuclear Fusion*, 39(9Y):1283–1294, 1999.

[24] M.G. Haines. A heuristic model of the wire array z-pinch. *Plasma Science, IEEE Transactions on*, 26(4):1275–1281, 1998.

[25] Peter U. Duselis, Jeffrey A. Vaughan, and Bruce R. Kusse. Factors affecting energy deposition and expansion in single wire low current experiments. *Physics of Plasmas*, 11(8):4025–4031, 2004.

[26] G. S. Sarkisov, K. W. Struve, and D. H. McDaniel. Effect of current rate on energy deposition into exploding metal wires in vacuum. *Physics of Plasmas*, 11(10):4573–4581, October 2004.

[27] S. C. Bott, D. M. Haas, Y. Eshaq, U. Ueda, F. N. Beg, D. A. Hammer, B. Kusse, J. Greenly, T. A. Shelkovenko, S. A. Pikuz, I. C. Blesener, R. D. McBride, J. D. Douglass, K. Bell, P. Knapp, J. P. Chittenden, S. V. Lebedev, S. N. Bland, G. N. Hall, F. A. Suzuki Vidal, A. Marocchino, A. Harvey-Thomson, M. G. Haines, J. B. A. Palmer, A. Esaulov, and D. J. Ampleford. Study of the effect of current rise time on the formation of the precursor column in cylindrical wire array z pinches at 1 MA. *Physics of Plasmas*, 16(7):072701–14, July 2009.

[28] S. N. Bland, S. V. Lebedev, J. P. Chittenden, D. J. Ampleford, S. C. Bott, J. A. Gomez, M. G. Haines, G. N. Hall, D. A. Hammer, I. H. Mitchell, and J. B. A. Palmer. Effect of Radial-Electric-Field polarity on Wire-Array Z-Pinch dynamics. *Physical Review Letters*, 95(13):135001, 2005.

[29] S. Rosenthal, P. Sasorov, G. Sarkisov, and T. Sanford. New paradigm : controlling initiation phase is necessary for optimization of wire-array z-pinch performance. Technical report, August 2008.

[30] G. S. Sarkisov, K. W. Struve, and D. H. McDaniel. Effect of deposited energy on the structure of an exploding tungsten wire core in a vacuum. *Physics of Plasmas*, 12(5):052702–9, May 2005.

[31] G. S. Sarkisov, S. E. Rosenthal, K. W. Struve, V. V. Ivanov, T. E. Cowan, A. Astanovitskiy, and A. Haboub. Effect of current prepulse on wire array initiation on the 1-MA ZEBRA accelerator. *Physics of Plasmas*, 14(5):052704–4, May 2007.

[32] F. N. Beg, A. E. Dangor, P. Lee, M. Tatarakis, S. L. Niffikeer, and M. G. Haines. Optical and x-ray observations of carbon and aluminium fibre z-pinch plasmas. *Plasma Physics and Controlled Fusion*, 39(1):1–25, 1997.

[33] S. C. Bott, S. V. Lebedev, D. J. Ampleford, S. N. Bland, J. P. Chittenden, A. Ciardi, M. G. Haines, C. Jennings, M. Sherlock, G. Hall, J. Rapley, F. N. Beg, and J. Palmer. Dynamics of cylindrically converging precursor plasma flow in wire-array z-pinch experiments. *Physical Review E (Statistical, Nonlinear, and Soft Matter Physics)*, 74(4):046403–21, October 2006.

[34] G. N. Hall, J. P. Chittenden, S. N. Bland, S. V. Lebedev, S. C. Bott, C. Jennings, J. B. A. Palmer, and F. Suzuki-Vidal. Modifying Wire-Array Z-Pinch ablation structure using coiled arrays. *Physical Review Letters*, 100(6):065003–4, February 2008.

[35] D. B. Sinars, M. E. Cuneo, E. P. Yu, S. V. Lebedev, K. R. Cochrane, B. Jones, J. J. MacFarlane, T. A. Mehlhorn, J. L. Porter, and D. F. Wenger. Measurements and simulations of the ablation stage of wire arrays with different initial wire sizes. *Physics of Plasmas*, 13(4):042704–13, April 2006.

[36] S. V. Lebedev, D. J. Ampleford, S. N. Bland, S. C. Bott, J. P. Chittenden, J. Goyer, C. Jennings, M. G. Haines, G. N. Hall, D. A. Hammer, J. B. A. Palmer, S. A. Pikuz, T. A. Shelkovenko, and T. Christoudias. Physics of wire array z-pinch implosions: experiments at imperial college. *Plasma Physics and Controlled Fusion*, 47(5A):A91–A108, 2005.

[37] S. V. Lebedev, F. N. Beg, S. N. Bland, J. P. Chittenden, A. E. Dangor, and M. G. Haines. Snowplow-like behavior in the implosion phase of wire array z pinches. In *Review,Tutorial and Invited Papers from the 43rd Annual Meeting of the APS Division of Plasma Physics*, volume 9, pages 2293–2301, Long Beach, California (USA), May 2002. AIP.

[38] K. G. Whitney, J. W. Thornhill, J. P. Apruzese, J. Davis, C. Deeney, and C. A. Coverdale. Enhanced energy coupling and x-ray emission in z-pinch plasma implosions. *Physics of Plasmas*, 11(8):3700–3714, 2004.

[39] D. B. Sinars, R. W. Lemke, M. E. Cuneo, S. V. Lebedev, E. M. Waisman, W. A. Stygar, B. Jones, M. C. Jones, E. P. Yu, J. L. Porter, and D. F. Wenger. Radiation energetics of ICF-Relevant Wire-Array z pinches. *Physical Review Letters*, 100(14):145002–4, April 2008.

[40] C. Deeney, T. Nash, R. R. Prasad, L. Warren, K. G. Whitney, J. W. Thornhill, and M. C. Coulter. Role of the implosion kinetic energy in determining the

kilovolt x-ray emission from aluminum-wire-array implosions. *Physical Review A*, 44(10):6762, November 1991.

[41] A. G. Rousskikh, D Pil'tikhina, R. B. Baksht, I. I. Beilis, and S. A. Chaikovsky. Effect of electrode polarity on wire explosion in vacuum. *Journal of Applied Physics*, 104(1):013306–6, July 2008.

[42] A.G. Rousskikh, R.B. Baksht, S.A. Chaikovsky, A.V. Fedunin, K.V. Khishchenko, A.Yu. Labetsky, P.R. Levashov, A.V. Shishlov, and S.I. Tkachenko. The effects of preheating of a fine tungsten wire and the polarity of a High-Voltage electrode on the energy characteristics of an electrically exploded wire in vacuum. *Plasma Science, IEEE Transactions on*, 34(5):2232–2238, 2006.

[43] T. W. L. Sanford, R. C. Mock, J. F. Seamen, M. R. Lopez, R. G. Watt, G. C. Idzorek, and D. L. Peterson. Wire fixturing in high wire-number z pinches critical for high radiation power and reproducibility. *Physics of Plasmas*, 12(12):122701–8, December 2005.

[44] S. V. Lebedev, F. N. Beg, S. N. Bland, J. P. Chittenden, A. E. Dangor, M. G. Haines, K. H. Kwek, S. A. Pikuz, and T. A. Shelkovenko. Effect of discrete wires on the implosion dynamics of wire array z pinches. *Physics of Plasmas*, 8(8):3734–3747, 2001.

[45] S. V. Lebedev, F. N. Beg, S. N. Bland, J. P. Chittenden, A. E. Dangor, M. G. Haines, S. A. Pikuz, and T. A. Shelkovenko. Effect of Core-Corona plasma structure on seeding of instabilities in wire array z pinches. *Physical Review Letters*, 85(1):98, July 2000.

[46] G. S. Sarkisov, P. V. Sasorov, K. W. Struve, D. H. McDaniel, A. N. Gribov, and G. M. Oleinik. Polarity effect for exploding wires in a vacuum. *Physical Review E*, 66(4):046413, October 2002.

[47] Matthew R. Gomez, David M. French, Wilkin Tang, Peng Zhang, Y. Y. Lau, and R. M. Gilgenbach. Experimental validation of a higher dimensional theory of electrical contact resistance. *Applied Physics Letters*, 95(7):072103–3, 2009.

[48] A. H. Guenther and J. R. Bettis. The laser triggering of high-voltage switches. *Journal of Physics D-Applied Physics*, 11:1577–1613, 1978.

[49] J. R. Woodworth, C. A. Frost, and T. A. Green. uv laser triggering of high-voltage gas switches. *Journal of Applied Physics*, 53(7):4734–4739, July 1982.

[50] J. R. Woodworth, Jr. Hargis, L. C. Pitchford, and R. A. Hamil. Laser triggering of a 500-kV gas-filled switch: A parametric study. *Journal of Applied Physics*, 56(5):1382–1386, 1984.

[51] M.A. Kemp, R.D. Curry, J.M. Gahl, K.F. McDonald, and K.W. Struve. Modeling and analysis of the rimfire gas switch. *Plasma Science, IEEE Transactions on*, 33(4):1245–1251, 2005.

[52] E. Husain and R.S. Nema. Analysis of paschen curves for air, n2 and SF6 using the townsend breakdown equation. *Electrical Insulation, IEEE Transactions on*, EI-17(4):350–353, 1982.

[53] R.J. Adler. Pulse power formulary. North Star Research Corp. Albuquerque, NM, 1989.

[54] F.W. Peek. *Dielectric phenomena in high voltage engineering*. McGraw-Hill Book Company, inc., 1920.

[55] RV Latham. *High voltage vacuum insulation: basic concepts and technological practice*. Academic Pr, 1995.

[56] J. F. Kolb, R. P. Joshi, S. Xiao, and K. H. Schoenbach. Streamers in water and other dielectric liquids. *Journal of Physics D: Applied Physics*, 41(23):234007, 2008.

[57] E A Litvinov, G A Mesyats, and D I Proskurovskii. Field emission and explosive electron emission processes in vacuum discharges. *Soviet Physics Uspekhi*, 26(2):138–159, 1983.

[58] E.M. Waisman, M. E. Cuneo, W. A. Stygar, R. W. Lemke, K. W. Struve, and T. C. Wagoner. Wire array implosion characteristics from determination of load inductance on the z pulsed-power accelerator. *Physics of Plasmas*, 11(5):2009–2013, May 2004.

[59] R.C. Weast and Chemical Rubber Company. *CRC handbook of chemistry and physics*. CRC press Boca Raton, FL, 1988.

[60] Ian H. Hutchinson. *Principles of plasma diagnostics*. Cambridge University Press, 2002.

[61] S. N. Bland, D. J. Ampleford, S. C. Bott, S. V. Lebedev, J. B. A. Palmer, S. A. Pikuz, and T. A. Shelkovenko. Extreme ultraviolet imaging of wire array

z-pinch experiments. *Review of Scientific Instruments*, 75(10):3941–3943, October 2004.

[62] S. Bland. Personal communication. 2009.

[63] Rick B. Spielman, Lawrence E. Ruggles, Richard E. Pepping, Stephen P. Breeze, John S. McGurn, and Kenneth W. Struve. Fielding and calibration issues for diamond photoconducting detectors. In *Proceedings of the eleventh topical conference on high temperature plasma diagnostics*, volume 68, pages 782–785, Monterey, California (USA), 1997. AIP.

[64] R. B. Spielman, C. Deeney, D. L. Fehl, D. L. Hanson, N. R. Keltner, J. S. McGurn, and J. L. McKenney. Fast resistive bolometry. In *Proceedings of the 12th topical conference on high temperature plasma diagnostics*, volume 70, pages 651–655, Princeton, New Jersey (USA), 1999. AIP.

[65] Ryan McBride. *Implosion dynamics, radiation characteristics, and spectroscopic measurements of wire-array z-pinches on the Cornell Beam Research Accelerator (COBRA)*. PhD thesis, Cornell University, 2009.

[66] D. A. Chalenski, B. R. Kusse, and J. B. Greenly. Soldered contact and current risetime effects on negative polarity wire array z pinches. *Physics of Plasmas*, 16(8):082707–9, 2009.

[67] Raymond W. Lemke and M. Collins Clark. Theory and simulation of high-power microwave generation in a magnetically insulated transmission line oscillator. *Journal of Applied Physics*, 62(8):3436–3440, October 1987.

[68] Raymond W. Lemke. Linear stability of relativistic space-charge flow in a magnetically insulated transmission line oscillator. *Journal of Applied Physics*, 66(3):1089–1094, 1989.

[69] Robert I. Lawconnell and Jesse Neri. Theory of magnetically insulated electron flows in coaxial pulsed power transmission lines. *Physics of Fluids B: Plasma Physics*, 2(3):629–639, March 1990.

[70] C. A. Coverdale, C. Deeney, M. R. Douglas, J. P. Apruzese, K. G. Whitney, J. W. Thornhill, and J. Davis. Optimal Wire-Number range for high X-Ray power in Long-Implosion-Time aluminum z pinches. *Physical Review Letters*, 88(6):065001, 2002.

[71] T. W. L. Sanford, C. A. Jennings, G. A. Rochau, S. E. Rosenthal, G. S. Sark-

isov, P. V. Sasorov, W. A. Stygar, L. F. Bennett, D. E. Bliss, J. P. Chittenden, M. E. Cuneo, M. G. Haines, R. J. Leeper, R. C. Mock, T. J. Nash, and D. L. Peterson. Wire initiation critical for radiation symmetry in Z-Pinch–Driven dynamic hohlraums. *Physical Review Letters*, 98(6):065003–4, February 2007.

[72] M. R. Gomez, J. C. Zier, R. M. Gilgenbach, D. M. French, W. Tang, and Y. Y. Lau. Effect of soft metal gasket contacts on contact resistance, energy deposition, and plasma expansion profile in a wire array z pinch. *Review of Scientific Instruments*, 79(9):093512–5, 2008.

[73] S. V. Lebedev, R. Aliaga-Rossel, S. N. Bland, J. P. Chittenden, A. E. Dangor, M. G. Haines, and I. H. Mitchell. The dynamics of wire array z-pinch implosions. In *The 40th annual meeting of the division of plasma physics of the american physical society*, volume 6, pages 2016–2022, New Orleans, Louisiana (USA), May 1999. AIP.

[74] P. Rambo, J. Schwarz, and J. C Diels. High-voltage electrical discharges induced by an ultrashort-pulse UV laser system. *Journal of Optics A: Pure and Applied Optics*, 3(2):146–158, 2001.

[75] J.D. Sethian, M. Myers, I.D. Smith, V. Carboni, J. Kishi, D. Morton, J. Pearce, B. Bowen, L. Schlitt, O. Barr, and W. Webster. Pulsed power for a rep-rate, electron beam pumped KrF laser. *Plasma Science, IEEE Transactions on*, 28(5):1333–1337, 2000.

[76] W. R. Rapoport, J. Goldhar, and J. R. Murray. KrF laser-triggered SF6 spark gap for low jitter timing. *IEEE Transactions on Plasma Science*, 8:167–170, September 1980.